Development of Isotope Selective CT Imaging Based on Nuclear Resonance Fluorescence

A thesis for the degree of Ph.D.

by

Khaled Ali Mohammed Ali

Graduate School of Energy Science

Kyoto University, Japan

Kyoto, 2022

This work is a tribute to my supervisor, Ohgaki. The wonderful teacher who has taught me so much more than simple words could express. I will remember the impact you made on me for the rest of my life. I thank you for making me different.

Khaled Ali

CONTENTS

ABSTRACT

Nondestructive inspection (NDI) technology, which is used to identify particular isotopes in a substance, is important for nuclear waste management, nuclear safety, and nuclear material nonproliferation. Several research advocated using the nuclear resonance fluorescence (NRF) technique with gamma rays for the measurement of the isotopes of interest. One of the most remarkable features of computed tomography (CT) based on the NRF transmission method (NRF − CT) is the isotope selectivity capacity to differentiate an isotope of interest from other isotopes within the same volume. The technique can be used as an NDI for shielding isotope substances such as fissile material content in spent fuel. The NRF − CT imaging technique was demonstrated for the enriched lead isotope (^{208}Pb) distribution implanted in an aluminum cylinder together with a set of different materials including the enriched lead isotope (^{206}Pb) distribution, iron, aluminum, and a vacant area. The holder had a diameter of 25 mm and a height of 20 mm. The experiment was conducted at the beamline BL1U in the UVSOR − III synchrotron radiation facility at the Institute for Molecular Science, National Institutes of Natural Sciences, Japan. We were able to generate a laser Compton scattering (LCS) gamma-ray beam with a maximum energy of 5.54 MeV, intensity flux of 5.5 photons/s/eV, and beam diameter of 1 mm. The LCS gamma-ray beam was able to excite the $J^{\pi} = 1^{-}$ NRF level at 5.512 MeV in ^{208}Pb. Therefore, we were able to obtain an isotope-selective NRF − CT image in two *d*imensions (2D) for the ^{208}Pb distribution with a resolution of 2 mm/pixel within an acquisition time of 60 hours. Then, we upgraded the experimental conditions to define the LCS gamma-ray beam with a 2 mm beam size and an intensity flux of 10 photons/s/eV. Consequently, we obtained an isotope-selective NRF − CT image in three dimensions (3D) for the ^{208}Pb distribution with a resolution of 4 and 8 mm/pixel for the horizontal and vertical planes, respectively, within an

acquisition time of 48 hours. Increasing the resolution of the obtained images is critical for the NRF − CT imaging technique to be applicable in realistic applications. We proposed the numerical treatment of the fusion visualization (FV) method for improving the resolution of the obtained 3D NRF − CT image under the experimental conditions of the UVSOR − III facility. We implemented this treatment using a 3D gamma − CT image with a resolution of 1 mm/pixel measured at the same beamline using an LCS gamma-ray beam with an intensity flux of 0.7 photons/s/eV and a 1 mm beam size as an additional data source. We significantly improved the 3D NRF − CT image quality due to the employment of the FV technique with a specific method called the post-multiply FV (PMFV) method.

LIST OF TABLES

LIST OF FIGURES

LIST OF APPRVIATIONS

IAEA	International Atomic Energy Agency
HEU	Highly-Enriched Uranium
SNMs	Special Nuclear Materials
SSNMs	Strategic Special Nuclear Materials
LEU	Low-Enriched Uranium
LWR	Light Water Reactors
UF_6	Uranium Hexafluoride
MeV	Million electron volts
NDI	Nondestructive Inspection
IAT	Input Accountability Tank
MUF	Material Unaccounted
PWR	Pressurized Water Reactor
NRF	Nuclear Resonance Fluorescence
CT	Computed Tomography
LCS	Laser Compton Scattering
2D	Two Dimensions
3D	Three Dimensions
coh	Coherent
incoh	Incoherent
RTAB	Rayleigh Scattering Database
GDR	Giant-Dipole Resonance

HPGe	High Purity Germanium
FWHM	Full Width Half Maximum
ANDI	Active Non-Destructive Inspection
PNDI	Passive Non-Destructive Inspection
1D	One-Dimensional
AIST	National Institute of Advanced Industrial Science and Technology
HIγS	High-Intensity Gamma-Ray Source
ELI − NP	Extreme Light Infrastructure—Nuclear Physics
FEL	Free-Electron Lasers
CW	Continuous-Wave
RMS	Root Mean Square
FPD	Flat Panel Detector
ROI	Region of Interest
FV	Fusion Visualization
PMFV	Post-Multiply FV Method
T_r	Threshold Value
PSFV	Post-Sum FV Method

1 INTRODUCTION

1.1 Overview

The world's demand for nuclear materials is not solely focused on generating clean electricity; nuclear materials are also used in various critical applications. Some nuclear materials are used for military purposes, while others are used for civilian purposes as well. Medical isotope production, research and education [1], industrial radio sources [2], and a variety of other applications are among the civil applications. Keeping nuclear materials from spreading is a difficult endeavor. More than seventy-five years after the destructive power of nuclear explosives was first demonstrated, several international political and legal procedures are in place to help achieve nuclear non-proliferation goals. They include the countries' political obligations, multilateral treaties, and other legally enforceable agreements, including states' nonproliferation pledges, and, most importantly, international atomic energy agency (IAEA) safeguards. The IAEA plays a key role in independent verification, ensuring that nuclear material, infrastructure, and other safeguarded items are only used for peaceful purposes [3]. To tackle climate change, the world is working to transition away from fossil fuels. Therefore, several nations are exploring the use of nuclear power to boost reliable and clean energy production [4]. According to the official forecasts, nuclear power will continue to play a major role in low-carbon energy production during electricity generation, which is critical in the endeavor to attain net-zero emission [5]. According to the IAEA's forecast, global nuclear power generating capacity will reach 792 GW (net electricity) by 2050. To maintain its current proportion of the energy mix of electricity generation sources, nuclear power generation capacity would have to increase over the next three decades. As a result, nuclear power could supply around 12% of the world's electricity by 2050 [4].

1.2 Nuclear materials

Nuclear materials are one of the most important components of nuclear explosive devices [6, 7]. They include fissile, fissionable, and source materials [8]. Fissile materials are made up of atoms that may be split by neutrons in a self-sustaining chain reaction to release energy [9]. The most fissile materials used for non-peaceful purposes are highly-enriched uranium (HEU) (^{235}U isotope of uranium) and plutonium- 239 (^{239}Pu isotope of plutonium). Fissionable materials, such as deuterium-2 (^{2}H) and tritium-3 (^{3}H), are ones in which the atoms can fuse to release energy. The term "source materials" refers to materials that are used to augment nuclear threats by providing an extra supply of atomic particles for fission. ^{3}H, polonium-209 (^{209}Po), beryllium-4 (^{4}Be), lithium-6 (^{6}Li), and helium-3 (^{3}He) are among them [10]. Special nuclear materials (SNMs) are defined as ^{239}Pu, ^{233}U, or uranium enriched in the isotopes ^{235}U or uranium-238 (^{238}U), whether they are nuclear fuel or spent fuel forms, and need to be fully controlled, checked, and accounted for by the IAEA [11]. ^{233}U and ^{239}Pu do not exist naturally but are produced in nuclear reactors by irradiating source material or SNMs and may be chemically separated from old fuel or targets. Reprocessing is the process of extracting SNMs from spent fuel. Nuclear reactors that employ uranium as fuel or targets create ^{239}Pu. On the other hand, nuclear reactors that employ thorium as fuel or targets create ^{233}U. An enrichment facility produces uranium enriched in ^{235}U [9]. SNMs are only mildly radioactive, but they include fissile isotopes (^{233}U, ^{235}U, and ^{239}Pu) that might be utilized as the principal components of nuclear bombs if concentrated. Strategic special nuclear materials (SSNMs) are defined as these materials in quantities greater than formula quantities. The low-enriched uranium (LEU) concentration of ^{235}U may be enhanced to generate HEU, which is the key element in several nuclear explosive designs. Both ^{239}Pu and ^{235}U have been used in fission materials as nuclear explosives. These two components

accounted for nearly 90% of the work involved in developing the first nuclear explosives [12].

1.2.1 Plutonium

Plutonium, a manufactured element created in nuclear reactors, was used to create the world's first nuclear explosion [13]. ^{239}Pu is solid metal with a bright silvery color. It was originally formed at the beginning of the universe. However, having a half-life of only around 24,200 years naturally occurring traces of ^{239}Pu are hard to find. Trace quantities of this metal are still formed these days when terrestrial ^{238}U reacts with solar rays. However, this metal nowadays is mostly synthesized artificially. ^{239}Pu is produced from ^{238}U in nuclear power reactors. Firstly, as shown in equation (1.1), ^{238}U is struck with a high-energy neutron ($^{1}_{0}n$) and is converted into uranium-239 (^{239}U). ^{239}U is then, as shown in equation (1.2), changed into neptunium-239 (^{239}Np) by the emission of an electron and an anti-neutrino particle through beta (β^{-1}) decay. In the final stage, as shown in equation (1.3), ^{239}Np loses an electron and an anti-neutrino particle to form ^{239}Pu.

$$^{238}_{92}U + {}^{1}_{0}n \rightarrow {}^{239}_{92}U \qquad \text{Eq. (1.1)}$$

$$^{239}_{92}U \rightarrow {}^{239}_{93}Np + \beta^{-1} \qquad \text{Eq. (1.2)}$$

$$^{239}_{93}Np \rightarrow {}^{239}_{94}Pu + \beta^{-1} \qquad \text{Eq. (1.3)}$$

The neutrons are produced in a controlled chain reaction by the reactor. The speed of the neutrons must be slowed in order for them to be absorbed by the ^{238}U atoms. This is done by passing them through a material called a "moderator." In natural uranium reactors, graphite and heavy water (Deuterium oxide, $^{2}H_2O$, D_2O) [14] have been utilized as moderators [15]. Impurities in graphite will halt the chain reaction, so it must be extremely pure

to succeed as a moderator. Heavy water resembles conventional water in appearance and flavor, but it includes deuterium atoms rather than hydrogen. Heavy water must be clean in order to work as a moderator. It must be free of considerable contamination from ordinary water, with which it is frequently mixed in nature. Although the actual amount depends on the reactor type and operating conditions, nuclear reactors create around 300 gm of ^{239}Pu for every GW.d of produced electrical energy. As a result of nuclear power generation, approximately 6×10^5 kg of ^{239}Pu have been created globally since 1980 [16, 17].

1.2.2 Uranium

Uranium occurs naturally in underground deposits consisting of a mixture of 0.7% ^{235}U, which is easily fissionable, and about 99.3% ^{238}U, which does not contribute directly to the fission process (though it does so indirectly by the formation of fissile isotopes of ^{239}Pu) [18]. This isotope, like ^{239}Pu, is unstable and fissions when struck by a neutron. Fission, or the splitting of ^{235}U atoms in nuclear reactors, generates energy in the form of heat. Although ^{235}U and ^{238}U are chemically identical, their physical attributes, notably their mass, are not. ^{235}U has 92 protons and 143 neutrons in its nucleus, giving it an atomic mass of 235 units. On the other hand, the nucleus of ^{238}U holds 92 protons and 146 neutrons, three more than ^{235}U, giving it a mass of 238 units [19, 20]. Isotope separation, in general, is a physical process that concentrates ('enriches') one isotope compared to others [21]. Uranium enrichment is a process that increases the percentage of ^{235}U that undergoes thermal neutron fission in mined uranium, allowing it to be used as a nuclear fuel [22]. The enrichment of uranium to increase the proportion of ^{235}U to 90% or more is called HEU. HEU can be combined with ^{239}Pu to form the "pit", or it can be used alone for non-peaceful purposes. The bomb dropped on Hiroshima, Japan, used only HEU.

About $15-20$ kg of HEU is sufficient to make a bomb without ^{239}Pu. On the other hand, nuclear reactors require enrichment to about $3-5$ % of ^{235}U, which is called LEU. The mass difference between ^{238}U and ^{235}U allows the isotopes to be separated and the percentage of ^{235}U to be increased or enriched. This small mass difference is used in all present and historical enrichment processes, whether directly or indirectly. Uranium enrichment is necessary to manufacture fuel for light water reactors (LWR). Typical nuclear reactor fuel in presently enriched is natural composition (0.72% ^{235}U) to roughly (5% ^{235}U). The majority of the reactors are LWRs, which need uranium in their fuel to be enriched from 0.7% to $3-5$% ^{235}U. This is LEU in its natural state. Increased enrichment levels to roughly 7%, and as high as 20% for some special-purpose reactor fuels, are being considered. On the other hand, some reactors employ natural uranium as a fuel source. The prospect of civilian nuclear power infrastructure producing nuclear explosives drives nuclear material safeguarding measures. The security and accounting of enriched uranium and ^{239}Pu at declared civilian nuclear plants, as well as ensuring that clandestine nuclear material operations do not occur at undeclared locations, are among the essential safeguards.

1.3 Safeguarding enrichment facilities

Nuclear safeguards are a set of technical measures that the IAEA uses to independently verify a state's legal commitment not to divert nuclear facilities or material from peaceful nuclear activity to non-peaceful nuclear activities [3]. The ability to enrich uranium to dangerous levels is the key safeguard concern for an enrichment plant. On the other hand, the capacity to measure relative uranium isotope concentrations in materials at enrichment plants is crucial for safeguarding purposes. Uranium enrichment is currently measured using one of two methods; either gaseous samples such as uranium hexafluoride (UF_6)

are collected and studied using mass spectrometry, or passive counting of the 1.857 MeV gamma rays released during ^{235}U decay is conducted. Sampling is vehemently rejected by facility operators, who fear that it will introduce pollutants into delicate enrichment equipment. Therefore, since mass spectrometry is very costly, it is used infrequently [23, 24]. Calibrations are used in passive counting measurements to relate count rates to ^{235}U concentration and, consequently, enrichment. Because the calibration is sensitive to container thicknesses, which might change owing to erosion or deposition of solid UF_6 on the container surface, these measurements are prone to error. In principle, continuous measurement of fluorescent gamma rays on UF_6 at specific locations at an enrichment facility may be undertaken by nondestructive inspection (NDI) to monitor for relative concentrations of ^{235}U and ^{238}U. Enrichment measurements also give independent checks on the mass balance of uranium material entering, leaving, and presenting at the enrichment plant if the pressure and volume of the UF_6 are known. The nuclear materials safeguards require establishments authorized to hold SNMs to prove and maintain security systems that secure the material and prevent the loss or theft of SNMs in order to ensure public safety and national security [9]. According to the fissile material report [20], the global stockpile of HEU was over 1370 ± 125 tons at the end of 2014. While the global stockpile of the separated ^{239}Pu is 505 ± 10 tons. It is stated by the IAEA that the amount of mass in which the probability of producing a nuclear explosive is not excluded, is 25 kg for the HEU and 8 kg for the separated plutonium [25]. It means that the global amount of HEU and ^{239}Pu is sufficient to make approximately 1.2×10^4 nuclear explosives. In light of the above ability of the SNMs, the NDI techniques for screening SNMs have become a necessity for countering terrorism as well as supplying accountability tools to check these hazardous materials. Usage of nuclear power applications makes it imperative to take the

responsibility for supplying safety, regulatory, and security, and non-proliferation of nuclear materials. Many research groups have been working in the field of the NDI of the SNMs [26 – 29].

1.3.1 Facility security for spent fuel reprocessing

Measurement of fissile material composition in spent nuclear fuel is another example where it is important for safeguarding [3]. Chemical separation of actinides from fission products, as well as chemical separation of distinct constituent actinides from one another, is all part of reprocessing. Before reprocessing, the levels of ^{239}Pu and ^{235}U in spent fuel are not directly monitored. Surrogate signatures, such as the gamma rays released in the decay of Cesium-134 (^{134}Cs), Cesium-137 (^{137}Cs), and Europium-154 (^{154}Eu), can be detected as a burn-up indication and correlated to the ^{239}Pu and ^{235}U concentration using reactor model calculations. However, these measurements do not give independent information regarding fissile material content and are prone to systematic errors due to their reliance on reactor operating circumstances [30]. To avoid the disadvantages of indirect ^{239}Pu and ^{235}U measurements, these components are directly measured during the aqueous reprocessing process. Following fuel dissolving, the solution is transferred to an input accountability tank (IAT) with a defined volume, and a sample is taken for examination. Analytical radiochemistry methods are used to figure out the concentrations of ^{239}Pu and ^{235}U in the sample to a nominal 0.3 % uncertainty. Because the volume of IAT is known, saw concentrations in the sample can be linked to uranium and plutonium levels in the overall reprocessed assembly. However, because sampling takes place after dissolution, there is a chance that material will be diverted before reaching the IAT. In addition, for new fuel cycle systems, many non-aqueous reprocessing approaches are being considered. Some of these procedures do not include the

method of aqueous dissolution and sampling for determining fissile material content. The precision with which the fissile actinide concentration in spent fuel must be checked varies depending on the application. The IAEA's current objective is to have "no material unaccounted for" (MUF) [31]. The MUF is the difference between the amount of material entering a facility and the total amount of material exiting and present at the facility. In other words, there is a discrepancy between the real inventory and the nuclear material stock on the books. For example, if more ^{239}Pu entered a facility than was detected and then left, the MUF would be positive, indicating that there is material missing or unaccounted for. Because every measurement has a degree of uncertainty, MUF must have one as well. Improved safeguard technology aims to decrease MUF uncertainty to the lowest level achievable. Measurements of fissile material in spent fuel should, in principle, follow a Gaussian distribution whose width is specified by the measurement error's standard deviation in the absence of systematic uncertainty. Current spent fuel reprocessing systems process about three pressurized water reactors (PWR) assemblies per day, each holding about 3 kg of ^{239}Pu. If measurements of ^{239}Pu concentration were taken with 10% precision before the dissolution of each assembly, the system would produce approximately 2500 gm of ^{239}Pu MUF uncertainty per month due to statistical errors alone, ignoring any systematic errors. The mass uncertainty over a year would be around 8.7 kg. This means that continuous deviations of smaller amounts of ^{239}Pu could go undetected by materials accounting methods based on 10% measurements and that the amount of ^{239}Pu needed to make a nuclear explosive could be stolen over the course of one or two years while the facility complies with safeguards regulations. Reprocessing facilities currently measure fissile material with a nominal precision of 1% using destructive analysis of an aqueous sample collected from the IAT. This indicates that input ^{239}Pu uncertainties are one-tenth as large as those mentioned above, and that

continuous deviation would have to occur for a period of around 100 years (or at several reprocessing plants) to go unnoticed. However, if dissolved spent fuel is diverted around the ITA, the incidence of undetected ^{239}Pu diversion might skyrocket. This has sparked an interest in figuring out the content of intact spent fuel assemblies. Indirect measurements of ^{239}Pu concentration in used fuel assemblies can offer outstanding precision when compared to reactor models using well-known reactor conditions. However, without knowledge of reactor operating conditions such as power level fluctuations over time, these models have only $10-20\%$ accuracy. Because operators may provide erroneous information regarding a fuel's irradiation history on purpose or inadvertently, direct measurement of fissile material content would be the most trustworthy safeguard measurement. Therefore, we conclude that any technique that has the ability to measure ^{239}Pu or ^{235}U content in intact spent nuclear fuel with moderate precision and high accuracy would be technological advancement. Several methods for conducting such measurements are being researched [32]. From this standpoint, nuclear resonance fluorescence (NRF) is considered a considerable technology for assaying the isotopic composition of spent nuclear fuel. The research presented in this dissertation looks at the possibility of employing the NRF to conduct nuclear material investigations that might help prevent the spread of such materials.

1.4 Nuclear resonance fluorescence (NRF)

The purpose of nuclear or other radioactive material analysis is to figure out what the materials are, how they were manufactured, when and where they were made, and for what purposes they will be used [33]. Both radiometric and nonradiometric measuring techniques are included in the above definition of "analysis" [34 – 36]. The NRF technique is an effective method for studying nuclear physics as well as isotope imaging inside spent fuel canisters and

nuclear waste. F. R. Metzger [37] conducted the primary study that describes the physics and measuring procedures of that phenomenon. Physically, the NRF attenuation happens in the case of a sample targeted with a photon beam at a typical energy of 1.5 to 8 MeV during the investigation process. If the energy of an incident photon matches the excitation energy of a particular isotope, the isotope is excited because the nucleus of the isotope absorbs photons at specific energies, and then it decays to the ground state ($g.s.$) or to an excited state (E_f) by emitting a cascade of gamma-ray photons within a few picoseconds or less. Figure 1.1 illustrate the NRF process.

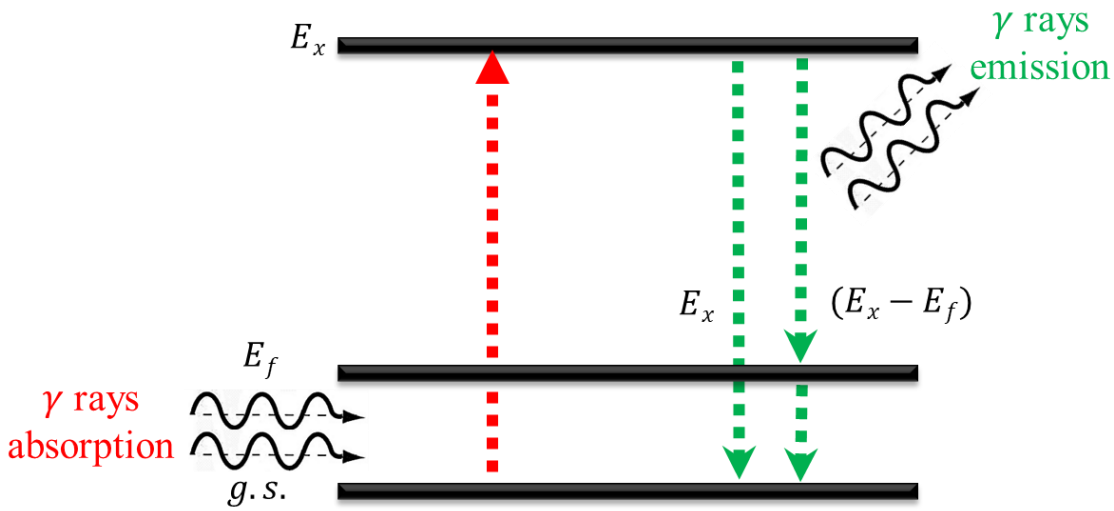

Figure 1. 1. The physics process of nuclear resonance fluorescence

The Breit–Winger resonance describes the energy dependence of the NRF cross-section [38, 39]. The relative simplicity of the interaction in the NRF process can produce some valuable spectroscopic information such as integrated NRF cross section (I_s), spin of the transition state (J), level excitation energy (E_i), transition width ratio $[(\Gamma_0^2)/\Gamma]$, state parity (π), and reduced excitation probabilities Γ_0. The NRF inspection can produce isotope-specific signatures for various materials, which can be used to assess materials' isotopic composition [40], due to the dependency of the excitation energies on the nuclear species. The power of the NRF technique can be demonstrated by a

comparison between attenuation path lengths for NRF gamma rays and those for x-ray photons and thermal neutrons utilized in other inspection techniques. Therefore, NRF provides a powerful probe for the NDI of SNMs even under severe shielding, which has a significant influence on homeland security technology [41 – 44]. NRF has a few key features that make it an extremely appealing active interrogation technique. The observed gamma rays are unique to certain isotopes. As mentioned, the NRF technique applies to a wide range of materials and compounds, not just SNMs. In contrast to many other activation analysis techniques, which might result in material activation or radiation damage, a gamma-ray excitation's low momentum transfer does not affect the sample being analyzed. The gamma-ray signatures have energy higher than 1 MeV, allowing considerable amounts of material to be penetrated. The NRF signatures for high atomic number (z) materials are near the atomic cross-section minima. The cross sections of NRFs are typically equal to, if not greater than, the atomic cross sections. The NRF cross sections are one to two orders of magnitude stronger than photofission cross sections at their strongest. The NRF resonances are quite narrow, approximately 1 electron volt (eV) wide after Doppler broadening. For more than five decades, researchers in nuclear physics have used NRF as a technique to study nuclear structures. The isotopic signature of the NRF at a MeV scale of energy permits the technique to work for a variety of applications, beyond the detection of SNMs, with reasonable sensitivity. Due to developments in accelerator technology, which allows for high-flux, high-duty-factor electron beams, and detector technology, which allows for high-resolution gamma-ray detection, this approach has been broadened to practical applications. O. Beck et al. [45] determined the carbon-13 (^{13}C) content in diamond non-destructively using the NRF technique. They proved that the NRF technique was able to detect the content of ^{13}C with a sensitivity that agreed well with Raman scattering. W. Bertozzi et al. [28] are

credited with being the first to propose the use of NRF as a method for detecting specific nuclear materials within cargo containers with bremsstrahlung gamma rays. T. Hayakawa et al. [41] measured the ratio of $^{12}C/^{14}N$ in the shielded melamine ($C_3H_6N_6$) by comparing the NRF spectra of carbon-12 (^{12}C) with that of nitrogen-14 (^{14}N). In addition, they clearly demonstrated the ability of NRF to identify chemical compounds. Another application of the NRF technique is the geo-sourcing of materials. It was found that there is a correlation between the ratio of lead isotopes or oxygen isotopes and their geo-location [46]. Accordingly, the NRF can provide a geo-location signature for many materials.

1.5 Research objectives

The isotope selectivity capability to distinguish an isotope of interest from others within the same volume is one of the most notable features of computed tomography (CT) based on the NRF transmission method ($NRF-CT$) for imaging techniques. This technique can be used as an NDI for shielding isotope substances such as fissile material content in spent fuel. The studies in this dissertation are targeted to demonstrate the isotope selectivity of the $NRF-CT$ imaging technique using the laser Compton scattering (LCS) gamma rays available at the beamline BL1U in the $UVSOR-III$ synchrotron radiation facility at the Institute for Molecular Science, National Institutes of Natural Sciences, Japan. The following is a list of the research objectives for this dissertation:

- The first objective is to utilize the LCS gamma rays to obtain an isotope-selective $NRF-CT$ image in two dimensions (2D) for the ^{208}Pb isotope distribution with a reasonable resolution.
- The second objective is to upgrade the experimental conditions of measurements to obtain an isotope-selective $NRF-CT$ image in three

dimensions (3D) for the ^{208}Pb isotope distribution within a considerable acquisition time.

- ❖ Since increasing the resolution of NRF − CT images is critical for realistic applications, the third objective of the current research is to propose a numerical treatment method for improving the original 3D NRF − CT image resolution under the current experimental conditions of the UVSOR − III facility.

1.6 The Outlines of the Dissertation

The current chapter provides an overview of the global need for nuclear materials as well as the domains in which they can be used for military and civilian purposes. Additionally, worldwide political and legal procedures can assist in nuclear non-proliferation. It also explains the IAEA's role in verification, which assures that nuclear material, infrastructure, and other safeguarded items are only used for peaceful purposes. This chapter includes the materials that can be used for non-peaceful purposes, as well as a brief discussion of SNMs. The theory of the NRF phenomenon is then discussed, as well as its merits as a tool for NDI isotope detection. Chapter 2 presents the photon interaction mechanisms that are relevant to the NRF interactions and their detection, as well as the photon transport computations, because these interactions and their effects on the target materials or detectors should be well known for better evaluation of the methods and interpretation of physical phenomena that may appear during the investigations reported in this dissertation. The processes are introduced with the corresponding cross-sections since detecting NRF gamma rays includes the scattering of non-resonant photons owing to elastic and inelastic interactions. The NRF interaction is also shown, along with its cross-section and angular distribution. Chapter 3 provides a brief description of the NDI methodologies for nuclear

materials. It also provides the concepts for potential applications of the NRF gathered from a wide variety of sources, in addition to a few of the most intriguing applications, with a mention of the challenges for the NRF to be commonly applied in each category. Chapter 4 discussed in depth the optimum components of the NRF technique for the NDI measurements, including the source of photons and the detection mechanism. This chapter also covers the generation of LCS gamma rays at the UVSOR − III facility, as well as the computations of their parameters. Furthermore, the sample's description has been utilized as a specimen target in recent studies also presented. In chapter 5, we detail the first experimental study of this dissertation and the upgrading in the source of photons to demonstrate the isotope-selective capability of CT imaging based on the NRF transmission method in 2D using quasi-monochromatic LCS gamma-ray beams in the MeV region for enriched lead isotopes (^{208}Pb and ^{206}Pb) implied within a cylinder aluminum holder of 20 mm and 25 mm in height and diameter, respectively. Chapter 6 shows the second experimental study of this dissertation and the upgrading of experimental conditions in the UVSOR − III facility to demonstrate isotope-selective 3D NRF − CT imaging using the LCS gamma rays in the MeV region for an enriched lead isotope (^{208}Pb) distribution hidden inside the same cylindrical holder with another enriched lead isotope (^{206}Pb), Fe, and Al rods, in addition to a vacant area. Chapter 7 emphasizes the limitations of the NRF − CT imaging technique for isotopes using the LCS gamma-ray beams to perform the imaging in 3D under the current experimental conditions of the UVSOR − III facility. It also includes a proposal for a study of an alternative approach that uses a numerical treatment to improve the quality of a 3D NRF − CT image. Since this numerical treatment relies on an additional source of information, this chapter describes the measurement of the 3D gamma − CT image for the same sample at the UVSOR − III facility under comparable experimental

conditions and with minor changes to the parameters of the LCS gamma rays. The procedures of the numerical treatment for merging the two CT image sources are also described. This chapter also includes an assessment of a few different numerical treatments and their impact on the image quality achieved. Chapter 8 presented the summary and conclusion of this work, as well as the future prospects for multiple isotope identification and quantification in the NRF − CT imaging approach employing LCS gamma-rays accessible at the UVSOR − III facility. Furthermore, the plan for the simulation work on NRF − CT imaging of SNMs mapping and characterization in nuclear waste and spent fuel under highly active circumstances may open up a practical use of the NRF − CT imaging technology in the future. The dissertation ends with a list of references, followed by a list of scientific journal publications, international conference proceedings, and presentations and posters from the different domestic conferences.

2 RADIATION-MATTER INTERACTION

2.1 Overview

Since our measurements are based on the NRF employing gamma rays, the present chapter discusses gamma rays and their numerous interactions with atoms and nuclei. Thorough knowledge of the mechanisms involved in the radiation-matter interaction is essential to properly understanding and developing NDI systems for nuclear materials. Radiation Physic is the conventional term for the branch of physics that examines how ionizing radiation interacts with matter and is particularly concerned with the outcomes of these interactions, notably the transfer of energy from radiation to the environment [47]. Radiation can be defined as the emission of energy in the form of subatomic particles or electromagnetic waves through a material medium or in a vacuum, which implies an interchange of energy and matter. Radiation is therefore considered energy in motion. The different types of radiation have vastly different interactions with matter [48]. Radiation, in general, can be classified into ionizing radiation and non-ionizing radiation based on its ability to ionize matter, or, more specifically, based on its ability to entirely detach one electron from the rest of the atom, and is commonly given in eV units. Ionizing radiation's fundamental characteristic is that it contains sufficient energy to ionize atoms. Once these are ionized, they can recombine or create new chemical compounds. This alteration may be permanent or long-lasting. Non-ionizing radiation, in contrast, lacks the energy to ionize or break atomic bonds. Therefore, the best it can do is produce collective motions of the material's electrons without causing any long-term alterations. This type of radiation includes microwave fields, electric infrared radiation, magnetostatic fields, and radio frequencies. It also includes visible light and ultraviolet radiation, while some of its effects can sometimes be comparable to those

produced by ionizing radiation [49, 50]. The following interactions may occur when radiation flows through matter:

- The interactions between radiation with an atom-sized wavelength (a few angstroms) and the atom itself. In most cases, the atomic electrons engage in the interaction, as in the photoelectric effect or the Compton Effect. Electromagnetic waves or electron beams can also be diffracted by a collection of atoms or crystals.
- Nuclear reactions are interactions with the atomic nucleus that produce radiation with a wavelength on the order of the nucleus' size.
- Particle bombardment in high-energy particle accelerators produces high-energy radiation through interactions with nucleons (neutrons and protons).

In a general way, each interaction has a certain probability of occurring based on the energy and nature of the radiation. Although there is no collision in the classical sense with an effective contact of the two particles, we usually use the words "shock" or "collision" instead of "interaction". This is the case, for example, of the interaction of an electromagnetic wave with an electron or the case of an alpha particle with an atomic nucleus, where effective contact is replaced by repulsion of the Coulomb force unless the alpha is very energetic and will overcome this force. As we mentioned, ionization is the process by which accelerated electrons get enough energy to escape from the parent atom. The intensity of ionization, also known as specific ionization, is defined as the number of ion pairs created per centimeter of transit through a material. The amount of ionization produced by a particle per unit length, which is a measure of its ionizing power, is proportional to the particle's mass and the square of its charge, according to the equation below:

$$I = \frac{m \times z^2}{E_{\text{kin}}} \qquad \text{Eq. (2.1)}$$

where I refer to the particle's ionizing power, m is its mass, z is the number of unit charges it carries, and E_{kin} is its kinetic energy. Because m for an alpha particle is about 7300 times greater than m for a beta particle, and z is twice as large, an alpha particle with the same energy would produce significantly more ionization per unit length. This phenomenon occurs because the larger alpha particle moves slower for a given energy and thus acts on a given electron for a longer time. Since the present dissertation's studies focus on the interaction of gamma-ray photons with matter, we will go over the major interactions of gamma rays with matter.

2.2 Electromagnetic radiation

Gamma rays are electromagnetic radiation that is similar to x-rays. The difference is that gamma rays come from an atom's nucleus, whereas x-rays come from circling electrons. An x-ray is created when orbiting electrons migrate to a lower energy orbit or when fast-moving electrons approaching an atom are deflected and decelerated when they react with the atom's electrical field. Nuclear processes and the disintegration of excited nuclei produce gamma rays. Due to their lack of mass and charge, gamma rays are challenging to block and have a remarkable ability to penetrate. Several feet of concrete or several meters of water will allow a small portion of the original gamma stream to pass through. Two physical mechanisms of photons' interactions with materials are absorption and scattering, owing to interactions with atomic electrons or nuclear material, respectively. The absorption process includes transmission as well since the transmitted intensity of a photon beam can be expressed as a complement to the absorbed intensity. The scattering process is the main process in the NRF for materials inspection due to its contribution to the background spectrum of the NRF and its significant effect on the signal-to-noise ratio. Scattering is divided into two categories: elastic scattering and

inelastic scattering. There are several interactions that can occur in each category, with different probabilities based on the energy of the electromagnetic wave and the material properties.

2.2.1 Photon linear attenuation coefficient

Gamma rays' attenuation or shielding is an essential part of radiation safety plans that attempt to decrease worker exposure to ionizing radiation [51]. The proportion of attenuated incoming photons in a monoenergetic beam per unit thickness of a material is described by the linear attenuation coefficient "μ". It includes all interactions including coherent scattering, Compton scattering, and the photoelectric effect. It is expressed numerically in units of cm^{-1} [52]. The equation for the fundamental law of attenuation for electromagnetic radiation in a matter is as follows [53]:

$$I = I_0 \, e^{-\mu_l \, L} \qquad \text{Eq. (2.2)}$$

where I_0 and I are the incident and transmitted photon intensities, respectively, μ_l is the linear attenuation coefficient, and L is the thickness of matter. The linear attenuation coefficient can be described as a function of photon energy (E) of the incident beam, the atomic number (z), and the density ρ. The mass attenuation coefficient was introduced to avoid the attenuation coefficient μ being dependent on the absorber density. The equation (2.2) may be stated using the mass attenuation coefficient, which is defined as the ratio of the linear attenuation coefficient μ_l to the absorber density ρ as follows [54]:

$$I = I_0 \, e^{-\mu \, \rho \, L} \qquad \text{Eq. (2.3)}$$

where the value ($\rho \, L$) refers to the areal density of matter. XCOM: Photon Cross Sections Database [55] supplies mass attenuation coefficients for each element and photon energies up to 100 GeV. Figure 2.1 shows the energy

dependence of mass attenuation coefficients for ^{238}U, emphasizing the relative importance of the four primary attenuation processes: photoelectric effect, pair production, Compton scattering, and elastic scattering [56]. The figure clearly shows the energy intervals to which the different components contribute significantly. Low-energy attenuation is dominated by the photoelectric effect. Compton scattering is primarily responsible for attenuation in the intermediate energy range, followed by pair production in the case of high-energy photons.

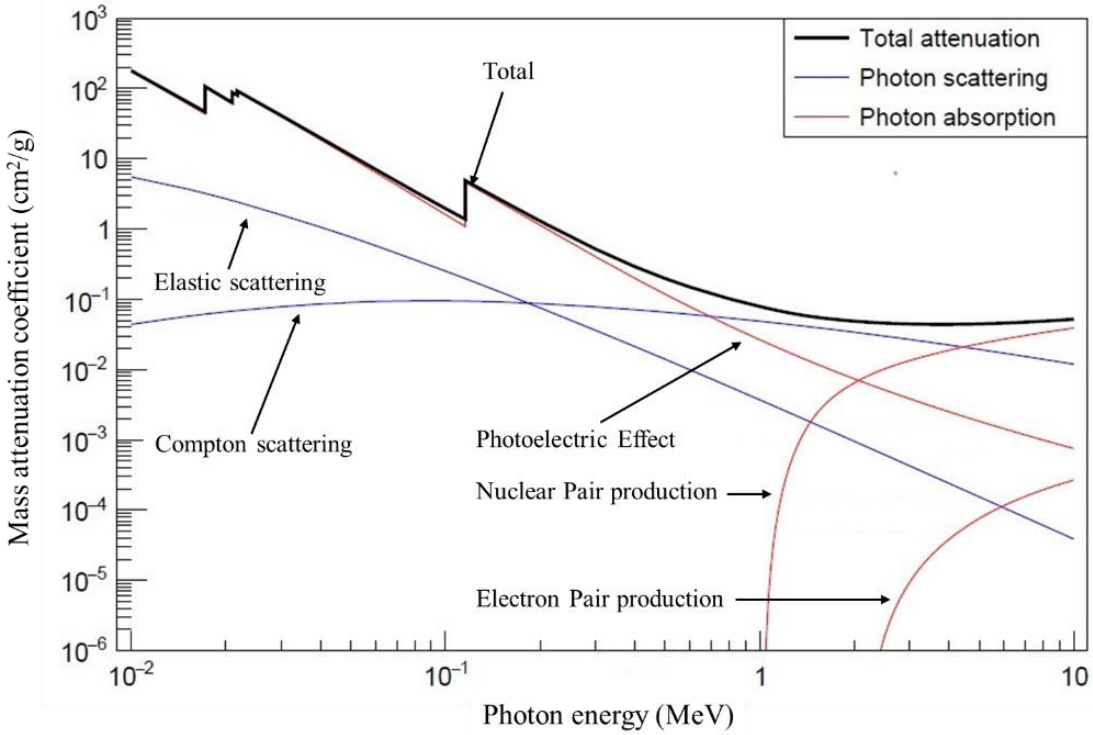

Figure 2. 1. Energy dependence of the mass attenuation coefficients for uranium [56]

The mass attenuation coefficient for composite materials may be calculated using the attenuation coefficients and the weight fraction (wi) of each individual element as follows [57]:

$$\mu = \sum \mu_i w_i \qquad \text{Eq. (2.4)}$$

The mass attenuation coefficient may be stated in terms of the interaction cross-section as follows:

$$\mu = \frac{N_0 \sigma}{A} \qquad \text{Eq. (2.5)}$$

where N_0 refers to Avogadro's number, σ is the cross-section of the interaction, and A is the atomic mass of the absorber [58]. Furthermore, the interaction cross-sections can be expressed as the sum of the individual contributions of the different attenuation processes as follows:

$$\sigma = \sigma_{pe} \pm \sigma_{pair} \pm \sigma_{Comp} \pm \sigma_{coh} \pm \sigma_{incoh} \pm \sigma_{NRF} \pm \cdots \qquad \text{Eq. (2.6)}$$

The individual components of the cross-section may be categorized into two classes based on the photon's interaction mechanism: non-resonant and resonant interactions. The difference between these two categories is that in a non-resonant process, the incident photon does not match the internal frequency of the interacting structure. Non-resonant interactions include the photoelectric effect, Compton scattering, pair production, and elastic scattering. Resonant interactions between a photon and the atomic nucleus can occur below and above the particle separation threshold. There are too many details to describe all these forms of interactions. Therefore, in this dissertation, we will only consider photon-nucleus interactions below the separation threshold, restricting the resonant attenuation coefficient to only NRF.

2.2.2 Non-resonant attenuation

Photon absorption and photon scattering are two types of processes that contribute to non-resonant attenuation. The photoelectric effect, or pair production, is an example of this process in which the primary photon no longer exists after the interaction takes place and secondary particles are released. Photon scattering is an interaction in which the propagation direction or kinetic energy of an incoming photon is changed. In photon scattering, there are four types of interactions: elastic, inelastic, coherent, and incoherent. The

terms “elastic” and “coherent” are frequently used interchangeably; however, they are not equivalent [59]. The kinetic energy of the participants is conserved in an elastic interaction, which limits the energy transfer between the incident photon and the scatterer's internal degrees of freedom [60]. In an inelastic process, however, the kinetic energy of the interaction is not preserved, resulting in excitations, bond breakage, and other phenomena. On the other hand, the coherence of the scattering is concerned with the phase difference between the incoming and scattered waves. Two coherent scattering interactions will result in constructive and destructive interference, which must be included when computing the total differential cross-section because the interaction intensity is proportional to the sum of the square of the scattering amplitudes. In incoherent processes, there is no interference since the interactions are unrelated, and the total cross-section equals the sum of the individual cross-sections.

2.2.2.1 Photoelectric effect

Photoelectric interaction (photon-electron) was one of the first processes that illustrated the quantum nature of light. In this interaction, a photon transmits all of its energy to an electron in one of the atomic shells. This energy causes the electron to leave the atom and move through the surrounding matter. The electron rapidly loses energy and moves just a short distance from its starting point [61]. As a result, the photon's energy is deposited in the matter at the photoelectric interaction site. It takes two steps to transmit energy. In the first step, the photon transmits its energy to the electron. Then, the electron deposits energy into the surrounding matter in the second step. Electrons that are tightly linked to the atom, or those with high binding energy, are more likely to interact photoelectrically. Photoelectric interactions are most likely when the electron binding energy is just slightly lower than the photon's energy.

A photoelectric interaction is impossible if the binding energy is larger than the photon's energy. According to another explanation, photoelectric interaction is only conceivable when the photon has enough energy to overcome the binding energy and remove the electron from the atom. A portion of the energy is used to defeat the binding energy of the electron and remove it from the atom. The leftover energy is kinetically transmitted to the electron and deposited near the interaction site. Because the interaction leaves a hole in one of the electron shells, usually the K or L, an electron goes down to fill it. A distinctive x-ray photon is typically produced as the filling electron's energy drops [62]. Figure 2.2 shows a schematic drawing of the photoelectric effect.

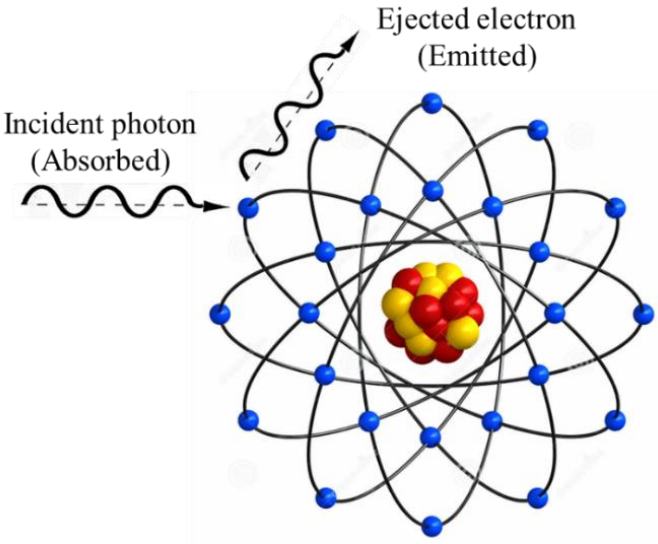

Figure 2. 2. Photoelectric effect

The photon's energy in the photoelectric interaction is divided into two parts. In general, the threshold energy for a two-body interaction can be calculated using the following formula [63]:

$$E_t = \frac{(M_3 + M_4)^2 - (M_1^2 + M_2^2)}{2\,M_2} \qquad \text{Eq. (2.7)}$$

where M refers to the interacting particles' relativistic mass. In the case of the photoelectric effect, we may express equation (2.7) as the flowing formula by

using the photon's rest mass ($M_1 = 0$), the electron's rest mass ($M_3 = M_e$), and the electron's binding energy ($M_4 = M_2 - M_e + E_b$):

$$E_t = \frac{(M_2 + M_b)^2 - M_2^2}{2\,M_2} = E_b + \frac{E_b^2}{2M_2} \approx E_b \qquad \text{Eq. (2.8)}$$

Because of the significant difference between the atom's mass (M_2), which is typically in the GeV range, and the binding energy (E_b), which has maximum values in the tens of keV region, the recoil term $[E_b^2/2\,M_2]$ from equation (2.8) can be easily dropped. Thus, the interaction threshold is equal to the interacting atom's lowest electron binding energy. The following formula is a description of the energy conservation process [61]:

$$E_k = h\nu - E_b \qquad \text{Eq. (2.9)}$$

where E_k refers to the energy of the expelled electron, and $h\nu$ is the energy of the incident photon. The ionized atom generated by the photo-electron emission will go through a stabilization process that involves the absorption of a free electron from the medium or internal rearrangement via atomic transitions, which may be named x-rays or Auger electron emissions. The angular distribution of the emitted photon can be approximated in two cases: in the first case, if the photon energy is higher than the binding energy ($h\nu \gg E_b$), the electron will be released in the direction of the incident photon. In the second case, in which the incident photon energy is close to the binding energy, the emission tends to be in a direction normal to the incident photon. It is difficult to obtain a general formula for the interaction cross-section. The following formula describes an approximate estimate considering the atomic number and incident photon energy:

$$\sigma \approx \frac{z^n}{E_\gamma^{7/2}} \qquad \text{Eq. (2.10)}$$

where z refers to the atomic number, E_γ is the energy of the incident gamma rays, and n can range from 4 to 4.6 as the photon energy increases [53]. The non-resonant attenuation of low-energy photons is dominated by the photoelectric process.

2.2.2.2 Pair production interaction

In physics, pair production refers to the formation of two charged particles, one negative (electron) and the other positive (positron), from a pulse of electromagnetic energy moving through matter, generally near an atomic nucleus. It is a direct conversion of radiant energy to matter. Pair production is one of the principal ways in which high-energy gamma rays are absorbed in matter. Only photons with an energy of more than 1.02 MeV may cause it. This process is allowed above the threshold energy of four times the rest-mass energy of an electron ($4 \times 0.511 = 2.044$ MeV) for interactions in the field of an electron (figure 2.3 (a)) and of twice the rest-mass energy of an electron (1.022 MeV) for interactions in the field of a nucleus (figure 2.3 (b)). The interaction produces a pair of charged particles (electron and positron) with the same mass, each equivalent to a rest mass energy of 0.511 MeV [63].

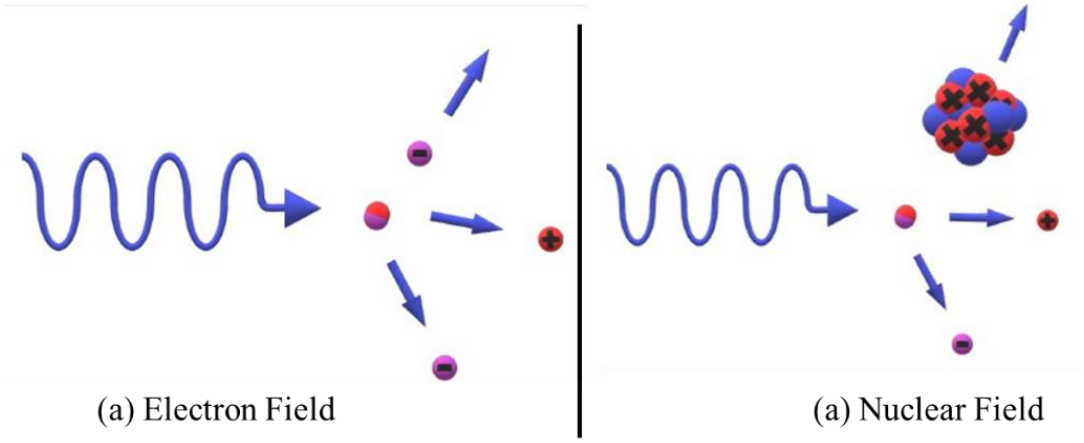

Figure 2.3. Pair production interaction. The process is threshold limited at (a) 2.044 MeV in the field of an electron and at (b) 1.022 MeV for an interaction in the field of a nucleus

The existence of a third body that will collect recoil momentum is needed for momentum conservation. The energy threshold for this interaction may be calculated using the same equation that was used to calculate the photoelectric effect in equation (2.8). To make this a two-body interaction, the emitted positron and electron will be considered as a single particle with twice the mass of the electron ($2M_e$). The energy threshold can be calculated with $M_1 = 0$ as follows [63]:

$$E_t = \frac{(2M_e + M_2)^2 - M_2^2}{2\,M_2} = \frac{2M_e(M_e + M_2)}{M_2} \qquad \text{Eq. (2.11)}$$

For the interaction in the field of an electron field interaction, $M_2 = M_e$ gives $E_t = 4\,M_e$, and for a nucleus $M_2 \gg M_e$, the threshold energy is $E_t = 2\,M_e$. Energy conservation can be expressed as:

$$\begin{cases} h\nu = 2m_e c^2 + E_k^{e+} + E_k^{e-} + E_r^{e-} \text{ (electron field)} \\ h\nu = 2m_e c^2 + E_k^{e+} + E_k^{e-} + E_r^{n} \text{ (nucleus field)} \end{cases} \qquad \text{Eq. (2.12)}$$

where $h\nu$ is the energy of the incident photon, $m_e c^2$ is the rest mass energy for an electron or positron, E_k^{e+} and E_k^{e-} are the kinetic energies of the positron and electron, respectively, and E_r^{e-} and E_r^{n} are the kinetic energies of the electron and recoil nucleus, respectively. The excess energy of the incident photon will be shared as kinetic energy by the electron, positron, and third body. In the nuclear field case, the E_r^{n} term can be ignored, given the significant difference in momentum between the incident photon and the nucleus. Although the energy split between the positron and the electron is not always equal, all energy distributions are allowed with similar probabilities. The exception is the limiting case in which one of the particles receives all the excess energy of the photon. The interaction in the electron field is also known as triplet production, as three particles appear from the interaction point due to the significant recoil energy transferred to the first electron. In this case, not all the possible

combinations of kinetic energy are allowed. The possible values can be calculated and are dependent only on the first photon energy [53]. Following pair production interaction, the electron travels through the material as a charged particle, dissipating its energy before coming to rest. When a positron collides with an electron in the medium, it loses energy and annihilates. Two 0.511 MeV photons will be released in opposite directions during the annihilation process. If the symbol z shows the atomic number and the symbol α refers to the fine structure constant, the following formula may be used to approximate the total cross-section of this process [63].

$$\sigma_t \approx \alpha\, z^2 \qquad \text{Eq. (2.13)}$$

2.2.2.3 Compton scattering effect

In the process of Compton scattering, a photon interacts with a weakly bound outer shell electron. Instead of being completely absorbed as in the photoelectric interaction, in the Compton process, the photon is deflected from its original direction and continues to exist but at a lower energy [64]. Only a portion of the energy is absorbed in this interaction, and a photon is scattered with less energy. This photon leaves the interaction point in a different direction from the initial photon. This form of interaction is classed as a scattering process due to the change in photon direction [63]. In this interaction, the material located on the initial beam path scatters a portion of the incoming radiation. This is necessary for some circumstances because this material functions as a secondary radiation source. If the energy of the incident photon is high compared with the electron binding energy for a photon-material interaction, the electron at rest assumption becomes valid. Figure 2.4 shows a diagram of the Compton scattering effect of a photon with an electron [65].

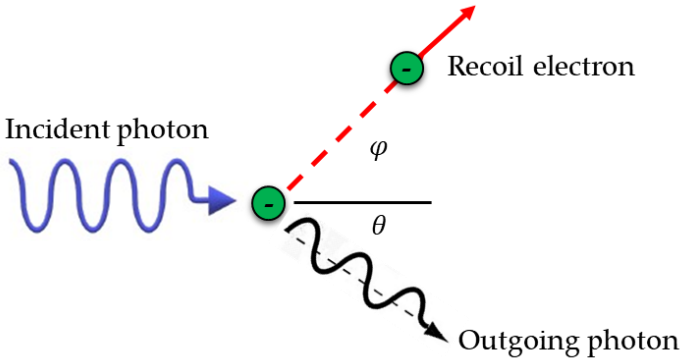

Figure 2. 4. Compton scattering effect

Compton scattering's energy conservation law may be written as [66]:

$$hv + m_e c^2 = hv' + E_e \qquad \text{Eq. (2.14)}$$

where hv and hv' refer to the energy of the incident and scattered photon, respectively, m_e is the rest mass of the electron, c is the speed of light, and E_e is the total recoil energy of the electron. On the other hand, the momentum conservation laws can be written as follows:

$$\begin{cases} p_v = p_{v'} \cos\theta + p_e \cos\varphi \ \text{(incident photon's direction)} \\ 0 = -p_{v'} \sin\theta + p_e \sin\varphi \ \text{(normal to incident photon's direction)} \end{cases} \qquad \text{Eq. (2.15)}$$

where p_v and $p_{v'}$ are the initial and scattered photon momentum, respectively, p_e is the electron momentum, and θ and φ are the scattering angles of the photon and electron, respectively, with respect to the initial propagation direction of the photon. The well-known Compton wavelength shift relation may be calculated using the prior two formulas as follows:

$$\Delta\lambda = \lambda' - \lambda = \lambda_c(1 - \cos\theta) \qquad \text{Eq. (2.16)}$$

where λ' is the wavelength of the scattered photon, λ is the wavelength of the incident photon, and λ_c is the Compton wavelength which can be defined as:

$$\lambda_c = \frac{h}{m_e c} = 0.0243 \ \text{Å} \qquad \text{Eq. (2.17)}$$

where h symbol refers to the Plank's constant. It is worth noting that the scattering photon's wavelength changes solely as the scattering angle changes θ, not as the initial photon energy changes. The energy transfer can range from zero to a considerable proportion of the initial energy, with the largest value reached when the scattering angle (θ) equals 180° , also known as a backscattering interaction. The Klein-Nishina formula may be used to calculate the interaction cross-section for this process as follows [67]:

$$\frac{d\sigma}{d\Omega} = r_e^2 \left[\frac{1}{1+\alpha(1-\cos\theta)}\right]^2 \left(\cos^2\theta + \frac{\alpha^2(1-\cos\theta)^2}{2[1+\alpha(1-\cos\theta)]}\right) \quad \text{Eq. (2.18)}$$

where r_e refers to the classical electron radius, $[\alpha = \hbar w/m_e c^2]$, and θ is the scattering angle. Figure 2.5 illustrates a polar coordinates plot of the Klein-Nishina formula for various values of incident energy [67]. As the incident photon's energy increases, the cross-sections collapse to a 0° scattering angle. By integrating on the solid angle, the total Klein-Nishina cross-section for Compton scattering on a free electron may be calculated as:

$$\sigma_e = \int \frac{d\sigma_e}{d\Omega} d\Omega \quad \text{Eq. (2.19)}$$

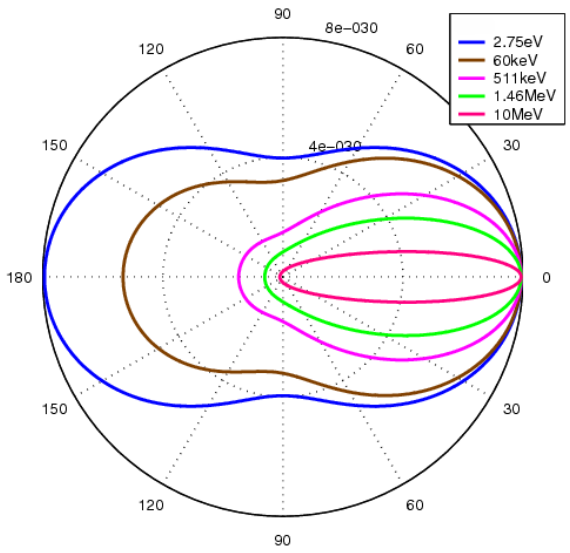

Figure 2. 5. The Klein–Nishina distribution of scattering-angle cross-sections over a range of routinely measured energies [67]

In the case where the incident photon energy is large in comparison to the electron binding energy, the total cross-section may be computed inside a material by using the total integrated cross-section of the above equation (2.19), in which the probability of scattering is proportional to the atomic number z. Compton backscattering is known as the interaction of a photon with a moving electron in which the photon gains energy after the scattering. The photon's energy after the collision may be estimated using the original electron and photon energies as well as the scattering angle. The maximum energy transfer is attained when the electron collides with the photon in head-on mode. The following formula may be used to estimate the photon energy after a collision:

$$E_\gamma \approx 4 \lfloor^2 E_i \qquad \text{Eq. (2.20)}$$

where $\lfloor$ refers to the Lorentz factor of the electron and E_i refers to the initial photon energy [68]. In the case of relativistic electrons, the energy gain of the photons can reach high values, making this interaction a very efficient energy amplification process. Compton backscattering is the mechanism used by LCS gamma-ray sources to produce high-intensity, quasi-mono-energetic photon beams, which will be discussed in depth in Chapter 4 of this dissertation.

2.2.2.4 Elastic scattering

Two terms make up the differential cross-section for elastic scattering; coherent (coh) and incoherent ($incoh$), which can be written as the following formula [69]:

$$\left(\frac{d\sigma}{d\Omega}\right)^{exp} = \left(\frac{d\sigma}{d\Omega}\right)^{coh} + \left(\frac{d\sigma}{d\Omega}\right)^{incoh} \qquad \text{Eq. (2.21)}$$

Each term will be discussed separately in the following sections.

2.2.2.4.1 Coherent scattering cross-section

The coherent term in equation (2.21) of the differential cross-section for elastic scattering can be calculated as:

$$\left(\frac{d\sigma}{d\Omega}\right)^{coh} = 0.5 \times \left[\left|A_{par}\right|^2 + \left|A_{per}\right|^2\right] \qquad \text{Eq. (2.22)}$$

where A_{par} refers to the scattering amplitudes parallel to the scattering plane and A_{per} is the scattering amplitudes perpendicular to the scattering plane. The scattering amplitudes are calculated according to the following formula:

$$A = A^T + A^R + A^D + A^N \qquad \text{Eq. (2.23)}$$

where the indexes T, R, D, N refer to the nuclear Thomson, Rayleigh, Delbrück, and nuclear resonance scattering, respectively. The individual contribution of each process to the total elastic cross-section is summarized in table 2.1 [70].

Table 2.1 The importance of nuclear Thomson, Rayleigh, Delbrück, and nuclear resonance scattering on the total elastic cross-section

Energy range	$<$ 0.1 MeV	0.1 ~ 1 MeV	$>$ 1 MeV
A^T	Non	Insignificant at small θ Important at medium and large θ Dominates at large θ for smaller z	Important at all, but smallest θ
A^R	Dominates at all θ	Dominates at small θ Important at medium and large θ	Importance restricted to smaller θ as energy increases
A^D	Non	Important at medium θ for large z	Important at all, but smallest θ
A^N	Non	Non	Increasingly important at medium and large θ as energy increases

2.2.2.4.2 Nuclear Thomson scattering

The classical scattering of electromagnetic radiation by a free-charged particle is known as Thomson scattering. The case of nuclear Thomson scattering occurs when the charged particle is an atomic nucleus. It is the low-energy limit of Compton scattering, in which the particle's kinetic energy and photon frequency remain unchanged [71]. This limit holds true if the photon energy is significantly lower than the particle's mass energy: $v \ll [mc^2/h]$, or if the photon wavelength is much longer than the particle's Compton wavelength [71]. Nuclear Thomson scattering amplitudes can be calculated analytically by using the following expressions [70]:

$$A_{per} = -r_e\, z^2\, \frac{m_e}{M} \qquad \text{Eq. (2.24)}$$

$$A_{par} = A_{per}\, cos\, \theta \qquad \text{Eq. (2.25)}$$

where r_e refers to the classical electron radius, m_e is the mass of the electron, z is the atomic number, M is the mass of the nucleus, and θ is the scattering angle. Nuclear Thomson amplitudes have no fictitious portion and are energy independent. The angular distribution is contained by A_{par} in the form of $cos\, \theta$. A retardation coefficient can be added to formula (2.24) to correct for the actual size of the nucleus:

$$A_{par} = -r_e\, Z^2\, \frac{m_e}{M} \left[1 - \frac{1}{3} k^2\, \langle r^2 \rangle\right] \qquad \text{Eq. (2.26)}$$

where k refers to the wavenumber of the incoming photon, and $\langle r^2 \rangle$ is the root mean square (RMS) charge radius of the nucleus [72]. The inclusion of the retardation correction coefficient gives the nuclear Thomson amplitudes an energy dependency, resulting in differences of up to 2%. Figure 2.6 shows a schematic depiction of Thomson scattering.

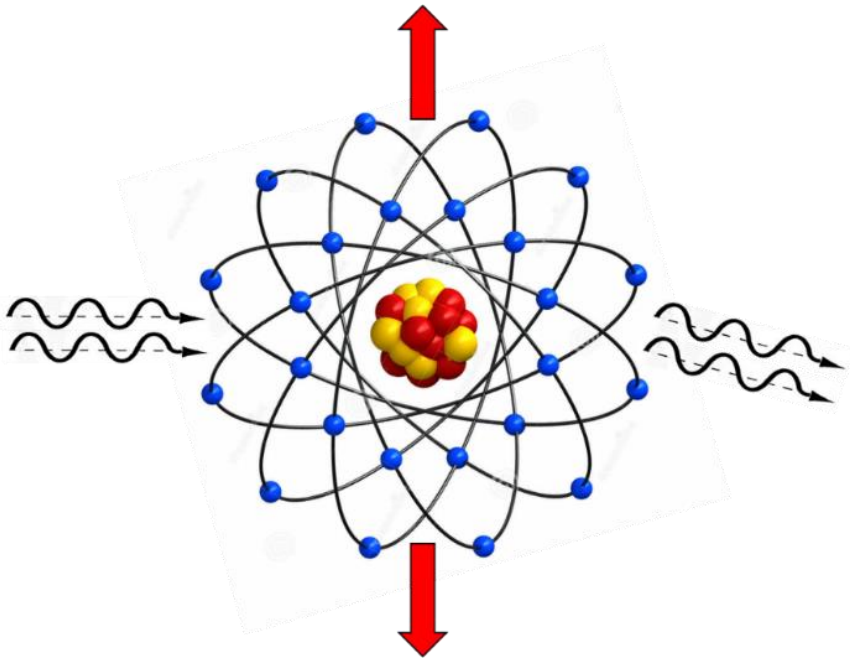

Figure 2. 6. Nuclear Thomson scattering

2.2.2.4.3 Rayleigh scattering

Rayleigh scattering can be defined with several expressions. In our case, it is the scattering of an electromagnetic wave of the bound atomic electrons in a collective and coherent fashion, in which the whole atom recoils to achieve conservation of momentum. A thorough theoretical explanation of the process would need to account for each electron's contribution to the scattering process, but this can become computing-intensive. As a consequence, two approximation approaches for calculating Rayleigh scattering amplitudes have been utilized in the following. The first method is based on atomic form factors and Thomson amplitudes [70], whereas the second method considers the individual contributions of the significant electrons as well as a general description of the rest of them [73, 74].

In the first method, the scattering amplitudes are determined as follows:

$$A_{per} = -r_e \, f(x,z) \qquad \text{Eq. (2.27)}$$

$$A_{par} = -r_e \, cos\,(\theta) \, f(x,z) \qquad \text{Eq. (2.28)}$$

where $-r_e$ is related to Tomson scattering and $f(x, Z)$ refers to the atomic form factor standing for the electronic charge distribution. I addition, the form factor is a function of z and x defined as [70]:

$$x = \frac{sin\,(\frac{\theta}{2})}{\lambda} \qquad \text{Eq. (2.29)}$$

where λ refers to the photon wavelength in angstroms. Several types of form factors have been proposed in previous studies. Kissel et al. [75] studied the non-relativistic, relativistic, modified, and anomalous, and their validity. Many works of literature have tabulated form factor values for various ranges of x and z values. For example, J. H. Hubbell et al. [76, 77] made comprehensive form factor tables available for a wide range of x values. When it comes to low energy photons and for low z scatterers, the form factor approach produces satisfactory results. On the other hand, it deviates from experimental results when high z elements and high energy are concerned. The most precise calculations of Rayleigh scattering amplitudes based on form factors are obtained by combining modified form factors with anomalous corrections [70].

The second method uses the estimation of the second-order scattering matrix $(S - matrix)$ [73, 74]. Although the $S - matrix$ formalism is computationally demanding; it gives the best results. L. Kissel et al. [70] established a simple approach to generating Rayleigh scattering amplitudes in the correct manner, based on $S - matrix$ calculations for the inner-shell electrons that contribute the most, and form-factor-based amplitudes for the outer electrons. The Rayleigh scattering database (RTAB) [78] contains data tables of scattering amplitudes calculated using $(S - matrix)$ calculations for photons up to 2.754 MeV. Figure 2.7 shows a schematic diagram of Rayleigh scattering.

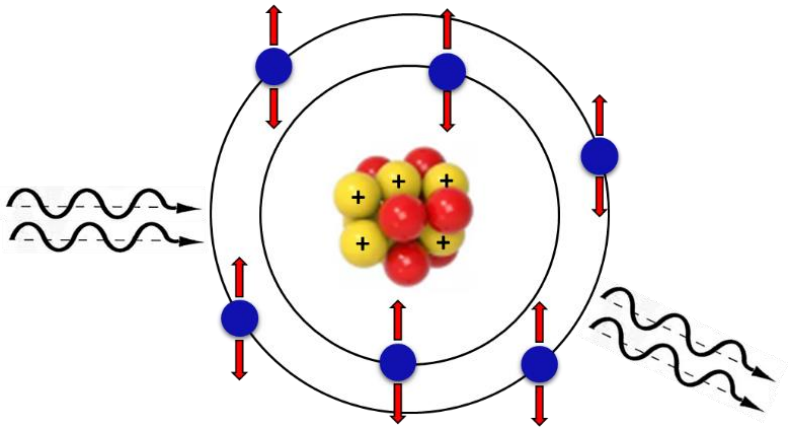

Figure 2. 7. Rayleigh scattering

2.2.2.4.4 Delbrück scattering

Delbrück scattering is the deflection of high-energy photons in the Coulomb field of nuclei due to vacuum polarization, which is one of quantum electrodynamics' nonlinear effects. It is also defined as the production of virtual pairs in the nuclear field followed by their annihilation and the emission of a single photon [79]. Delbrück scattering has been extensively studied both theoretically and experimentally up to a point that its fundamental features are by now well understood. Delbrück scattering has been seen at energies ranging from below the pair production $e^+ - e^-$ threshold to 7 GeV [80]. The amplitude is purely real in the low-energy limit and may be explained as being owing to some form of Coulomb field refractive index. H. Falkenberg et al. [81] estimated and tabulated the results of the Delbrück scattering amplitudes up to 10^2 MeV using the first-order Born approximation. In the high-energy limit, the amplitude is purely fictitious, which may be seen as a shadow scattering process related to $e^+ - e^-$ pair production. To get zero-degree scattering amplitudes in the limited case of forwarding scattering, analytical formulas can be used [63]. A comparison of theoretical and experimental data for high atomic numbers reveals the limits of the first-order Born approximation, with differences up to 40% due to the exclusion of multiphoton exchange [82, 83].

To improve the agreement between experimental and theoretical results, Coulomb corrections must be applied. Many studies proposed empirical [84, 85] and theoretical [82, 83] formulations for the Coulomb corrections, with a little advancement on the theoretical side. Some general features of Coulomb corrections were deduced from experimental data and were shown to be small for scatterers with $z < 50$, i.e., the Born approximation's accuracy is within 5% below $z = 50$ [86]. The photon energy and scattering angle are also factors in these corrections. The corrections appear to add up to the Delbrück scattering amplitudes below 4 MeV. However, it appears to have no impact on total cross-sections between 4 and 7 MeV. On the other hand, there appears to be a large contribution beyond 7 MeV but with an opposite sign regarding the low energy part [84]. The Coulomb corrections' angular dependence follows the same pattern as the lowest order approximation, with a rapid decay from low angles to an almost constant value at angles greater than 90° [79, 85]. Figure 2.8 shows a schematic depiction of Delbrück scattering.

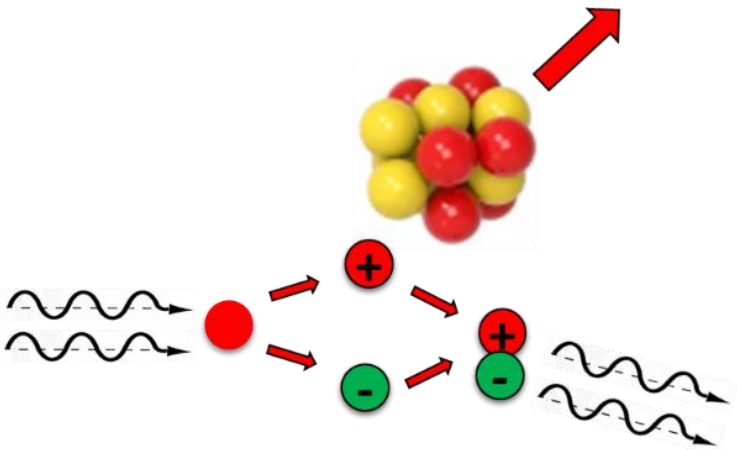

Figure 2. 8. Delbrück scattering

2.2.2.4.5 Giant-dipole resonance scattering

Nuclear resonance scattering is the scattering of the tail of a giant-dipole resonance (GDR). The coherent and incoherent scattering cross-sections are also influenced by this process. Depending on the shape of the nucleus, one or two

Lorentzian lines can be used to approximate the photonuclear absorption cross-section. The dispersion relations and the optical theorem can be used to calculate scattering amplitudes as follows [79]:

$$A_{per}^{N} = \frac{E^2}{4\,\pi\,\hbar\,c\,r_e}\sum_{v=1}^{2}\sigma_v\,\Gamma_v\,\frac{(E_v^2 - E^2 + iE\Gamma_v)}{(E_v^2 - E^2)^2 + E^2\Gamma_v^2} \qquad \text{Eq. (2.30)}$$

$$A_{par}^{N} = A_{per}^{N}\,cos\,\theta \qquad \text{Eq. (2.31)}$$

where E refers to the photon energy, E_v, Γ_v and σ_v refer to the parameters of GDR, with v the Lorentzian line indexes. Only above the (γ, n) threshold does the imaginary part of the first equation in the nuclear resonance scattering section produce a contribution, and it is set to zero below. The $\cos\theta$ part of the parallel amplitude accounts for the angular contribution to the scattering amplitude. In these references [87, 88] , experimental values of the GDR parameters are tabulated for a wide range of z and A values. A schematic diagram of nuclear resonance scattering is shown in figure 2.9.

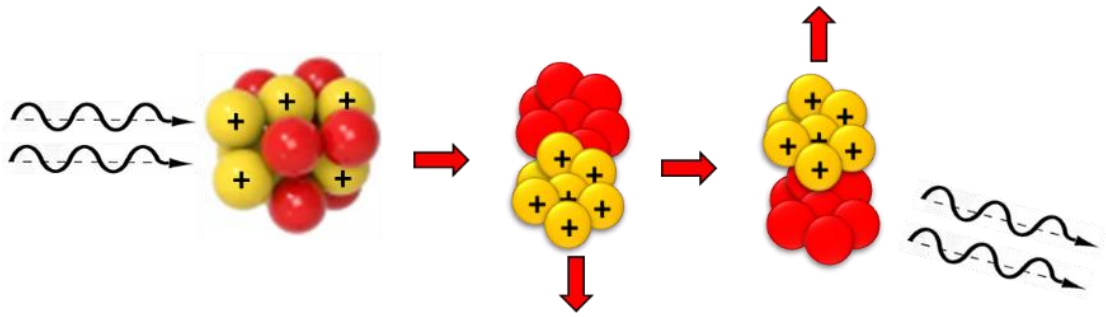

Figure 2. 9. Nuclear resonance scattering

2.2.2.4.6 Incoherent scattering cross-section

The incoherent term of the differential cross-section for elastic scattering corresponds to the transfer of two angular momentum units [72], which can be calculated from the following formula [89]:

$$\left(\frac{d\sigma}{d\Omega}\right)^{inc} = r_e^2\ (I_0\ K_0\ 20|I_0\ 2I_0\ K_0)^2\ [(2\alpha_1 - \alpha_2)^2 + (2\beta_1 - \beta_2)^2]\ \frac{1}{40}\ (13 + \cos^2\theta\ )$$

Eq. (2.32)

where I_0 feres to the nuclear spin, K_0 refers to the projection of I_0 on the symmetrical axis of the nucleus, $\alpha_1, \alpha_2, \beta_1\ \beta_2$ may be calculated using the formula:

$$A_{per}^{N} = \sum_{v=1}^{2} (\alpha_e + i\beta_v) \qquad \text{Eq. (2.33)}$$

where A_{par}^{N} is the coherent part of the nuclear resonance scattering's perpendicular scattering amplitude. The incoherent part's contribution to the overall cross-section is minimal below 7 MeV, but it becomes clear around the elastic scattering cross-minimum section [72]. For nuclei with $I_0 < 1$, the contribution of the incoherent scattering cross-section to the total differential cross-section disappears.

2.2.3 Resonant attenuation

2.2.3.1 Nuclear Resonance Fluorescence

Photons are released during nuclear stabilization steps in the gamma decay of a nucleus, which is known to be an isotope-specific process. Photon absorption is the inverse of photon emission, and it causes the nucleus to get excited. As we mentioned, NRF is the process by which an excited nuclear state emits gamma rays of specific energies to de-excite to its ground state. Herein these photons are referred to as NRF gamma rays. NRF is commonly induced in the context of material testing by exciting nuclear states with a photon beam. Photon detectors like high purity Germanium (HPGe) or scintillation detectors are used to monitor the following scatter of the NRF rays. The photo-absorption and NRF -ray energies, which are equivalent to passive-ray spectroscopy,

identify the nucleus that has undergone NRF since NRF states correspond to excited nuclear levels. When the assay geometry and NRF cross-section are known, the rate at which NRF occurs may be used to calculate the number of atoms in the corresponding isotope. In thin targets, the rate at which a nuclide undergoes NRF is given by:

$$R = \int N\phi(E)\,\sigma\,(E)\,dE \qquad \text{Eq. (2.34)}$$

Because the energy-dependent photon $\phi(E)$ varies as it passes the target, thicker targets require geometrical corrections. The Breit-Wigner distribution [38] gives the cross-section for photo-excitation of a nuclear state as:

$$\sigma(E) = \pi g \frac{(\hbar c)^2}{E^2} \frac{FF_0}{(E - E_i)^2 + (0.5 \times \Gamma)^2} \qquad \text{Eq. (2.35)}$$

where F refers to the full width half maximum (FWHM) of the state, F_0 refers to the partial width of the state for decay by gamma-ray emission to the ground level, E_i refers to the centroid energy of the resonance, and g refers to the statistical factor equal to the ratio of the number of spin states available for the excitation to the number of initial spin states. It is defined as follows for NRF events when the initial nuclear state is the ground level:

$$g = \frac{2J + 1}{2(2J_0 + 1)} \qquad \text{Eq. (2.36)}$$

where J is the angular momentum quantum number of the excited state, and J_0 is the angular momentum quantum number of the ground state. There are $(2J_0 + 1)$ magnetic substrates for a state of angular momentum J, and the additional factor of 2 in the denominator is because the photons inducing excitation can have two helicities. The probability of de-excitation of a state by a specific mode (i.e., neutron emission, gamma-ray emission, etc.) yielding a lower-energy state can be defined by the state's partial width for that mode:

$$p_i = \frac{F_i}{\sum_j F_j} = \frac{F_i}{F} \qquad \text{Eq. (2.37)}$$

where we have used $F = \sum_j F_j$. Implying that the summation over j includes all possible de-excitation modes. We conclude that the NRF cross-section occurs via emission of a single gamma-ray photon, and de-excitation to the ground level is given by:

$$\sigma_{g.s.}(E) = \frac{F_0}{F}\,\sigma(E) = \pi g \frac{(\hbar c)^2}{E^2} \frac{F_0^2}{(E - E_i)^2 + (0.5 \times F)^2} \qquad \text{Eq. (2.38)}$$

2.2.3.1.1 Angular Distributions of the NRF gamma rays

NRF is thought to only occur between states with angular momentum differences of 2 or fewer units. The scattering NRF gamma-rays' angular distribution will be represented using correlation functions, $W(\theta)$, that are specific to multipolarities of electromagnetic radiation. In a non-fixed reference frame, the observed gamma decay has an isotropic angular distribution. In general, more than one electric and magnetic multipole satisfies the selection rules governing a particular transition and can thus contribute to relative intensities that depend upon the detailed overlap of the initial and final states of nuclear wave functions [90 – 92]. As a result, the resulting angular distribution is a superposition of the contributing multipoles' distributions. The mixing ratio is predicted to be unknown in many circumstances when both electric and magnetic multipoles might contribute to the same transition. A correlation function, $W(\theta)$, is used to represent the angular distribution of the emitted NRF gamma-ray photons with respect to the incident photon direction. The multipolarities of the electromagnetic radiation involved in the emission transition affect the correlation function. Because the NRF interaction usually occurs between the levels that differ in angular momenta by 2 or less, the angular correlation function $W(\theta)$ of the scattered gamma photon, γ_2 with

respect to the incoming photon, γ_1 (incident beam), in cases of $L \leq 2$, can be written as [92]:

$$W(\theta) = \sum_{v=1,2,4} A_v(1)\, A_v\,(2)\, P_v\, cos\,(\theta) \qquad \text{Eq. (2.39)}$$

where θ refers to the scattering angle between the incoming and scattered photon, and $(P_v\, cos\,(\theta))$ is the Legendre function. The coefficients $A_v(1)$ is the photons in the entrance channel that have multi-polarity l_1 or $\left(l_1^{'} = l_1 + 1\right)$ and a mixing ratio δ_1. Furthermore, the $A_v(2)$ describes the scattered photons that have multi-polarity l_2 or $\left(l_2^{'} = l_2 + 1\right)$ and a mixing ratio δ_2. The mixing ratios can be written as:

$$\delta_{1(2)} = \frac{< \psi_f \left| l_{1(2)}^{'} \right| \psi_i >}{< \psi_f \left| l_{1(2)} \right| \psi_{i>}} \qquad \text{Eq. (2.40)}$$

The coefficients $A_v(1)$ and $A_v(2)$ also can be expressed in terms of F-coefficients as:

$$A_v(1) = \left(\frac{1}{1+\delta_1^2}\right)[F_v(l_1 l_1 J_0 J)] + 2\delta_1 F_v\left(l_1 l_1^{'} J_0 J\right) + \delta_1^2 F_v\left(l_1^{'} l_1^{'} J_0 J\right) \qquad \text{Eq. (2.41)}$$

$$A_v(2) = \left(\frac{1}{1+\delta_2^2}\right)\left[F_v\left(l_2 l_2 J_f J\right)\right] + 2\delta_2 F_v\left(l_2 l_2^{'} J_f J\right) + \delta_2^2 F_v\left(l_2^{'} l_2^{'} J_f J\right) \qquad \text{Eq. (2.42)}$$

In general, the angular distribution of the scattered NRF photons with respect to the beam directions can be described by the angular correlation function and written with the following formula [90]:

$$W_{i\to j\to k}(\theta) = \sum_{v=even} A_v^{-}\left(\gamma_{i\to j}\right) A_v^{+}\left(\gamma_{j\to k}\right) P_v\, cos\,(\theta) \qquad \text{Eq. (2.43)}$$

The angular distribution of photons scattered off an even–even nuclei through pure dipole $(Dip.)$ transitions with a spin sequence of $(0 \to 1 \to 0)$ for a non-polarized gamma-ray beam is given by:

$$W(\theta)_{Dip.} = \frac{3}{4}\,(1 + \cos^2\theta) \qquad \text{Eq. (2.44)}$$

Whereas the angular distribution for a pure quadrupole ($qdr.$) transition with a spin sequence of $(0 \rightarrow 2 \rightarrow 0)$ can be given by:

$$W(\theta)_{qdr.} = \frac{5}{4}\,(1 - 3\cos^2\theta + 4\cos^4\theta\,) \qquad \text{Eq. (2.45)}$$

Figure 2.10 shows the angular distribution function, $W(\theta)$ of a dipole transition with a spin sequence of $(0 \rightarrow 1 \rightarrow 0)$ as well as a quadrupole transition with the spin sequence of $(0 \rightarrow 2 \rightarrow 0)$ for an even-even isotope, such as ^{238}U transitions, in a case in which the incident gamma-rays' photons are un-polarized.

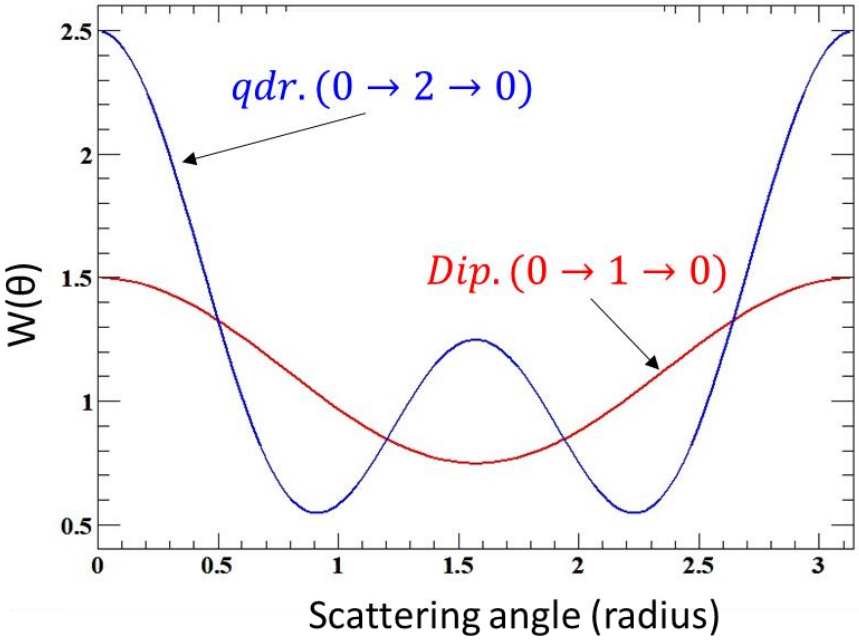

Figure 2. 10. The angular distribution function compared to the scattering angle (θ)

The angular distribution of gamma rays in the case of a linearly polarized gamma-ray beam of the Dipole transitions is given by:

$$W(\theta,\varphi)_{Dip.} = W(\theta)_{Dip.} \pm \frac{3}{4}\,(1 + \cos^2\theta\,)\,cos\,2\varphi \qquad \text{Eq. (2.46)}$$

where the minus sign for electric dipole ($E1$) and the plus sign for magnetic dipole ($M1$). Moreover, the angular distribution of gamma rays in the case of a linearly polarized gamma-ray beam of the Quadrupole transitions is given by:

$$W(\theta,\varphi)_{qdr.} = W(\theta)_{qdr.} \pm \frac{5}{4}\,(1 - 5\cos^2\theta + 4\,\cos^4\theta\,)\,cos\,2\,\varphi \qquad \text{Eq. (2.47)}$$

In the general case of $L = 1$ a dipole transition for which there is no mixing transition between $M1$ and $E2$, i.e., the maxing ratio of $M1/E2$ equals zero, the angular correlation function is given by:

$$W(\theta,\varphi)_{Dip.} = 1 + (F_2)^2\left[P_2 \times\ 0.5\,P_2^{(2)} \times cos\,2\varphi\,\right] \qquad \text{Eq. (2.48)}$$

where the F-coefficients can be found in various compilations [93, 94] and:

$$P_2 = 0.5 \times (3\ \cos^2\theta - 1\,) \qquad \text{Eq. (2.49)}$$

$$P_2^{(2)} = 3 \times (1 - \cos^2\theta\,) \qquad \text{Eq. (2.50)}$$

For quadrupole transitions with $L = 2$, the general equation for the angular distribution is:

$$W(\theta,\varphi)_{qdr.} = 1 + (F_2)^2\left[P_2 \pm 0.5\,P_2^{(2)}cos\,2\varphi\,\right] + (F_4)^2\left[P_4 \pm \frac{1}{12}P_4^{(2)} \times cos\,2\varphi\,\right] \qquad \text{Eq. (2.51)}$$

where:

$$P_4 = \frac{1}{8}(35\ \cos^4\theta\ - 30\ \cos^2\theta\ + 3) \qquad \text{Eq. (2.52)}$$

$$P_4^{(4)} = -\left[\frac{105}{2}\ \cos^4\theta + 60\ \cos^2\theta + \frac{15}{2}\right] \qquad \text{Eq. (2.53)}$$

In case of the consideration of the $E2$ transition only the angular distribution of quadrupole transitions will become:

$$W(\theta,\varphi)_{qdr.} = 1 + (F_2)^2\left[P_2 + 0.5\,P_2^{(2)}cos\,2\varphi\,\right] + (F_4)^2\left[P_4 - \frac{1}{12}P_4^{(2)}cos\,2\varphi\,\right] \qquad \text{Eq. (2.54)}$$

If there is a maxing ratio between $M1$ and $E2$, the dipole transition ($L = 1$) is given by:

$$W(\theta,\varphi)_{\left(\frac{E1}{M1}\right)} = 1 + (A_2)^2\,[P_2] + A_2\,a_2\,cos\,2\varphi\,P_2^{(2)} \qquad \text{Eq. (2.55)}$$

where:

$$A_2 = \left(\frac{1}{1+\delta^2}\right)\left[F_2(j_i j_f 11)\right] + 2\delta F_2(j_i j_f 12) + \delta^2 F_2(j_i j_f 22) \qquad \text{Eq. (2.56)}$$

$$a_2 = \left(\frac{1}{1+\delta^2}\right)\left[\frac{1}{2}F_2(j_i j_f 11)\right] - \frac{1}{3}\delta F_2(j_i j_f 12) + \frac{1}{2}\delta^2 F_2(j_i j_f 22) \qquad \text{Eq. (2.57)}$$

[a] ^{241}Am = 0.135%; ^{239}Pu = 81.9%; ^{241}Pu = 1.3%. the signal from 2 gm disk of plutonium metal, 1 cm diameter × 0.13 cm thickness.

2.2.3.1.2 NRF States

There are various methods to physically define states whose angular momentum deviates from the ground state by one or two units of angular momentum. The simplest example of such an idealized state is one in which a single nucleon is excited to a higher level. The nuclear structure suggests that these states will often have the same parity as the ground state. States with this property are easiest to detect close to closed nuclear shells. However, the majority of nuclear states require far more elaborate explanations. This section provides a simple framework for understanding NRF states and does not claim to contain an exhaustive list of all possible modes describing states that may undergo NRF [90]. The GDR consists of the most common NRF states. As we previously stated, the GDR is considered to be a collection of states in which the nuclear protons and neutrons collectively oscillate with respect to one another. The GDR is a parity-odd excitation mode because translation via the origin would swap the neutron-and proton-rich regions. GDR excitations have large cross-sections and effective widths because their angular momentum is unity. Since all nuclides have a GDR and the resonances overlap in energy, the

isotopic-specificity that may be inferred from the measurement of GDR-scattered photons is constrained by large GDR widths. As a result, measurement does not provide identification-relevant nucleus-specific information. Due to increasing backgrounds brought on by subsequent neutron capture, the tendency for neutron emission following GDR excitations further restricts the possibility of monitoring the GDR for NRF assay applications. Measured discrete resonances that are smaller than the GDR have been attributed to more complex collective excitation models. In contrast to the GDR's translational oscillation, the scissors-mode excitation model believes that nuclear states are caused by the combined rotating oscillation of neutrons and protons with regard to one another. A simple analysis of the mean relative separation between neutrons and protons would imply that the scissors mode excitation is only possible in non-spherical nuclei and that it has lower energy than the GDR. Translation via the origin for scissors mode oscillations is parity-symmetric, and thus scissors mode excitation is $\Delta J^{\pi} = 1^{+}$ and consequently M1 [90]. A schematic drawing of nuclei undergoing GDR, scissors-mode, and PDR excitations are shown in figure 2.11. White space inside the ellipses denotes proton-rich space, dark-color denotes neutron-rich space, and light-dark denotes nucleon concentrations that are similar. The nucleon oscillation's direction is shown by the arrows.

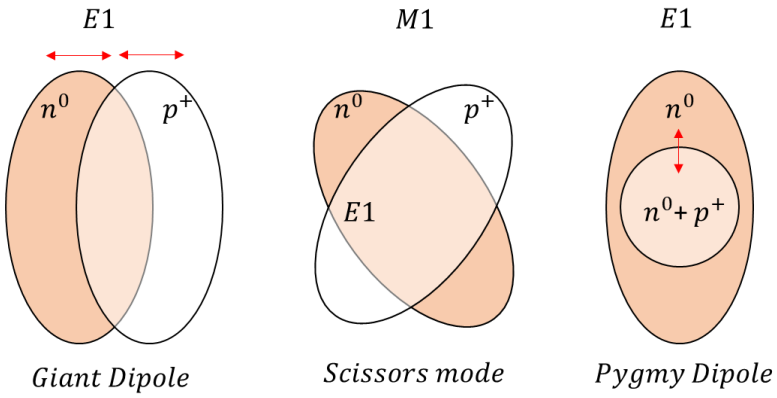

Figure 2. 11. Schematic of nuclei undergoing GDR, scissors-mode and PDR excitations

It has been shown that neutron-rich nuclei undergo lower-energy E1 excitations known as pygmy dipole resonances. The excess neutron skin oscillations with regard to the proton and neutron core are the model for these excitations, which have been investigated in tin isotopes [95]. Pygmy dipole resonances, like the GDR, are excited from the ground state via $E1$ transitions. The entire non-spherical nucleus rotating along an axis parallel to the nucleus' symmetry axis is another paradigm for defining collective nuclear states. The spins and parities of rotational states for even, even nuclei often follow the following pattern: $2^+, 4^+, 6^+, ...$, although odd-angular momentum excitations are also possible for odd-A nuclei. According to quantum mechanics, a rigid body's rotating excitation energy is given by:

$$E_{rot} = \frac{\hbar^2}{2 \times \Im} I(I+1) \qquad \text{Eq. (2.58)}$$

where I refer to the rotational quantum number, and $\Im$ refer to the rotational inertia of the nucleus. If the symbols a and b are referring to the lengths of the semi-major and semi-minor axis, respectively, the rotational inertia of an ellipsoid of mass M can be given by:

$$\Im_{class} = \frac{M}{5}(a^2 + b^2) \qquad \text{Eq. (2.59)}$$

M, a, and b will typically increase with increasing atomic number, which causes the rotational excitation energies to sharply decrease. The lowest excitation state for ^{12}C is a 2^+ state at 4439 keV [96]. This state's pattern and that of the 4^+ state at 14.083 MeV both point to a rotational spectrum. The first four excited states in ^{238}U follow the spectrum predicted by the rigid rotor model quite closely; however, the excitation energies of these states are only 44.92, 148.38, 307.18, and 518.1 keV for the $2^+, 4^+, 6^+$, and 8^+ states, respectively. Thus, it is clear that rotational excitation can lead to potential $\Delta J = 2$ NRF states in nuclides with low atomic numbers and even numbers of protons and neutrons, but in nuclides with high atomic numbers, the energies of rotational states

become too low to be useful for applying an assay method that uses NRF to observe these types of states. The rotating model grows more complicated for nuclei with non-zero ground-state angular momentum. A single nucleus may experience a number of excited states that follow rotational energy systematics because the angular momentum generated from a purely rotational excitation may be linked to the intrinsic angular momentum of the nuclear state. The energy scales of the excitations are expected to stay constant despite the more complex spectra [97]. Therefore, the utilization of an NRF assay technique for materials with low atomic numbers is only relevant for pure rotationally excited states. Another collective excitation model is known as nuclear vibration, in which the shape of the nuclear matter oscillates around the ground-state shape. The restorative force that tends to return deformed nuclear shapes to the ground state is proportional to the amount of deformation. Therefore, simple nuclear vibrations may be described as a form of the harmonic oscillator problem. The nuclear shape may be described as a sum of spherical harmonic functions, each with a given amplitude $(\alpha_{\lambda\mu})$. Each spherical harmonic $(Y_{\lambda\mu})$ corresponds to a state of specific angular momentum.

$$R(\theta,\phi) = R_0\left[1 + \sum\nolimits_{\lambda\mu} \alpha_{\lambda\mu}\, Y_{\lambda\mu}\,(\theta,\phi)\right] \qquad \text{Eq. (2.60)}$$

Any integer number greater than one ($\lambda > 1$) is possible. Because $\lambda = 1$ would require a translation of the entire nucleus, which is not conceivable without an external restorative force, it is not allowed. The vibrational excitation model produces distinct energy spectra, where the energy difference between a vibration mode's subsequent states is constant. Similar to vibrational modes in solid crystal lattices, it is generally accepted that the excitation between vibrational levels is caused by a single phonon. The parity of the phonon mode follows the rule $\pi = (-1)^{\lambda}$ [97]. With increasing atomic numbers, the excitation energy of quadrupole vibrational states tends to decrease.

Nevertheless, the decline is not as pronounced as for rotational excitations [98]. Another model describing collective ($\Delta J = 1$) states is the coupling of nuclear octupole ($\Delta J^{\pi} = 3^{-}$) vibrations with vibrational or rotational excitations of ($\Delta J^{\pi} = 2^{+}$). For even, even nuclei, this coupling results in states of spin and parity $1^{-}, 2^{-}, 3^{-}, 4^{-}$ and 5^{-} whose energies are near the sum of the octupole phonon and quadrupole state energies [99]. When the GDR is present, the transition strength for the 1^{-} state can be strengthened, producing potent E1 NRF resonances that frequently have energies between 2 and 4 MeV [90, 100]. The fact that the relatively straightforward forms discussed here in this section can couple with one another, producing states that would be characterized by considerably more complex models, complicates the explanation of NRF levels even more. For instance, reference [101] discusses 2^{+} NRF states of even mass Sn isotopes. The lowest phonon quadrupole vibrational states in the Sn isotopes lie between 1100 and 1300 keV. More 2^{+} NRF states were measured between 2 and 4 MeV that were classified as weakly collective states coupled with single-particle states. The same experiment also found strong E1 excitations for all isotopes between 3.2 and 3.5 MeV, which were determined as two phonons octupole-quadrupole coupling [102]. The creation of an exchange current by interacting nucleons within a nucleus might further complicate matters by leading to more intricate explanations of nuclear states and transitions. Although the difficulties in characterizing $\Delta J \leq 2$ excited nuclear states, the most important characteristics are their energies and the strength by which they are coupled to the ground state. A state's energy must be high enough for resonant gamma rays to be seen above inelastic and non-resonant elastic scattering background photons in order for it to be significant for NRF assay techniques. In contrast to higher-energy states that include extremely large admixtures of the GDR and may overlap in energy, the excitation energy of the state must also be low enough for it to be observed as a discrete state.

2.2.3.1.3 The strengths of the NRF transitions

Most commonly, the integrated cross-section of an NRF transition, measured in eV barns, is used to describe the strength of an NRF transition. Due to the singularity at $E = 0$, the integration of equation 2.35's total energies $E \geq 0$ does not converge. Since $E = 0$ photons are non-physical, the integral converges at a tiny lower energy integration limit $\in$.

$$\int_{\in}^{\infty} \sigma(E)dE \approx \int_{0}^{\infty} \pi g \frac{(\hbar c)^2}{E_0^2} \frac{F\, F_0}{(E - E_c)^2 + \left(\frac{F}{2}\right)^2} dE$$

$$= 2\pi^2 g F_0 \frac{(\hbar c)^2}{E_0^2} \qquad \text{Eq. (2.61)}$$

$$= 7648\ [b.\mathrm{MeV}^2] \frac{F_0}{E_0^2}\ g \qquad \text{Eq. (2.62)}$$

F can vary for nuclear states from virtually zero to several MeV. A state with $F \approx 0$ implies it has a long live time, such as the 3.167 MeV excited state of ^{91}Zr, which has a live time of 5.28 μs, corresponding to a width, $F = 1.5 \times 10^{-10}$ [103]. It is uncommon for long-lived states to be created from photon excitation since they frequently contain spins that are considerably different from the ground state. The 3.167 MeV state in ^{91}Zr is suspected of having a spin of 21/2, compared with the ^{91}Zr ground state spin of 5/2. F has high values when the state is short-lived. Relative to the ground state, the lowest excited state in ^{9}Be has a width of $F = 217$ keV and energy of 1684 keV [104]. The 1.684 MeV state can de-excite via neutron emission since ^{9}Be's neutron separation energy is 1.67 MeV [105]. When de-excitation by neutron emission is energetically permitted, it frequently occurs, drastically shortens level live times, and increases F. A state must have a high chance of being excited by ground state photo-absorption and de-excited by gamma-ray emission in order to be helpful for NRF assay. Neither of the levels mentioned in the paragraph above satisfies these requirements. Weisskopf et al. [106]

have calculated the rates of unhindered photon emission based on single-particle models for different multipolarity transitions. The shortest live times anticipated for levels that de-excite via gamma-ray emission is provided by the model, despite the fact that it tends to overestimate E1 transition rates.

$$t_{1/2s.p.}(E1) = \frac{6.76 \times 10^{-6}}{E^3 A^{2/3}} \qquad \text{Eq. (2.63)}$$

where E refers to the excitation energy of the state in keV. For the 4842 keV level in ^{208}Pb, the $E1$ transition to the ground state, reference [106] estimate results in a half-life of $t_{1/2s.p.} = 1.7 \times 10^{-18}$ s, and a width, $F = 270$ eV. However, the actual width of this level has been measured to be 4.78 eV, which corresponds to a half-life of 9.5×10^{-17} s [107]. This state is a relatively large NRF state. The majority of states that have been observed to undergo NRF have widths between 5 MeV and 10 eV, and while smaller resonances are likely to occur, it is challenging to discover them by looking for NRF gamma rays above background levels. The previous equation (2.63) indicates that for $E1$ transitions, F values tend to increase as E^3, whereas equation (2.35) showed that NRF cross sections are proportional to $F\ F_0/E^2$. According to this, the total strength of NRF resonances would rise linearly with energy if obstruction were ignored. However, the previous section (NRF states) reported that many states excited during NRF are distinctly collective, and as a result, their transition rates may exhibit hindrance due to structure effects. The formalism defining equation (2.63), on the other hand, assumes single-particle levels undergoing transitions. According to Weisskopf [106], live time estimates are also susceptible to underestimation. It is routinely found that electric quadrupole ($E2$) transitions for deformed nuclei occur at rates quicker than predicted by the Weisskopf $E2$ estimate:

$$t_{1/2s.p.}(E2) = \frac{9.52 \times 10^{6}}{E^5 A^{4/3}} \qquad \text{Eq. (2.64)}$$

The deformed nucleus's ground state and almost all of its excited states have high inherent electric quadrupole moments, which explains why the matrix element, $< \Psi^* | E2 | \Psi_0 >$, can grow when the state, $|\Psi_0 >$, has a significant collective component brought on by a quadrupole phonon. The 2^+ states of Sn are an example where the lowest states, thought to be predominantly vibrational, have transition rates approximately 10 times those predicted by equation (2.64). Theoretically, it was expected that the higher-energy observed 2^+ NRF states would have a more complex particle-phonon coupling and transition rates that are a little slower than those predicted by the Weisskopf single particle model. Any state that is allowed by energetics and spin conservation can be de-excited by gamma rays generated by NRF states. According to the Weisskopf estimations [106], the highest-energy gamma rays are preferred, although, for some NRF states, the nuclear structure may be crucial. An additional quantum number, K, which connects the total spin, J, to its projection onto the nuclear symmetry axis, can be used to explain the spins of highly deformed nuclei. For even, even nuclei with low-lying rotational states, theory indicates that the de-excitation of a $J = 1, K = 1$ state is twice as probable to occur to the ground state as to the first rotational state, whereas for a $J = 1, K = 0$ state the de-excitation is twice as probable to occur to the first rotational state [107, 108].

2.2.3.1.4 Nuclear recoil and thermal motion

In the case of the excited state, because the excited state's energy is not "sharp," absorption occurs even when the gamma energy differs from the resonant value. The energy of the emitted photon, generated in the decay process, will also need corrections due to the recoil energy transferred to the nucleus. Recoil energy of about 0.1 keV is expected for gamma rays in the 5~8 MeV energy range. The energy width of an excited nuclear state is defined by:

$$\Gamma = \frac{\hbar}{\tau} \qquad \text{Eq. (2.65)}$$

where Γ is known as the state's natural width. ħ is the reduced Plank constant and τ refers to the mean live time. If we were to pass photons beam through a collection of bare nuclei (to cut scattering and absorption processes due to atomic electrons), then the cross-section of the resonant absorption can be expressed as:

$$\sigma(E_\gamma) = \sigma_0 \frac{\left(\frac{\Gamma}{2}\right)^2}{\left[E_\gamma - (\Delta E + E_R)\right]^2 + \left(\frac{\Gamma}{2}\right)^2} \qquad \text{Eq. (2.66)}$$

where E_R, refers to the recoil correction $(E_\gamma^2)/(2Mc^2)$. Figure 2.12 shows the plot of this distribution [109].

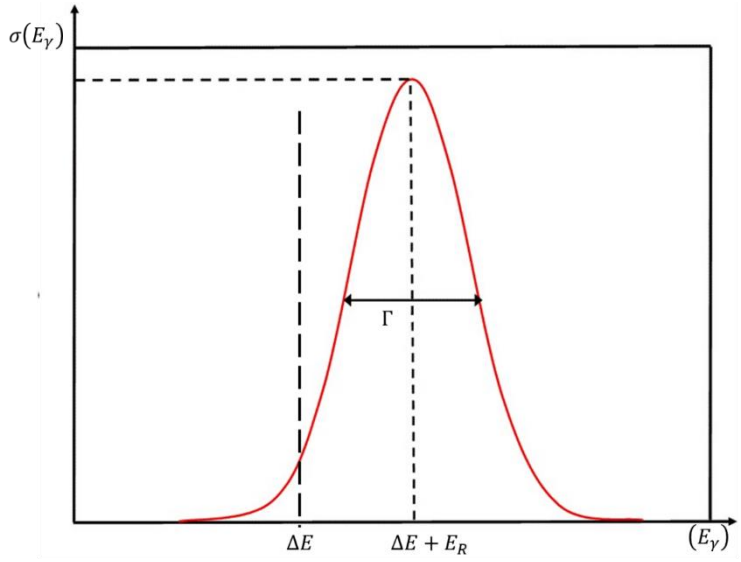

Figure 2. 12. The cross section of resonant absorption

The widths will be in the range of 10^6 to 10^3 eV for typical nuclear states with mean live times of ns to ps. However, we are unlikely to observe the natural linewidth in practice Γ. The Doppler broadening, which occurs because the nuclei are not at rest, as we assumed, but rather in thermal motion at any temperature T, is a major contributor to the measured linewidth. The photons as emitted or absorbed in the lab frame appear Doppler-shifted with energies:

$$E_{\gamma}^{'} = E_{\gamma}(1 \pm \frac{v_x}{c}) \qquad \text{Eq. (2.67)}$$

where v_x, refers to the velocity part along the photon direction. If the motion of the nuclei is represented by the usual Maxwell velocity distribution:

$$e^{-\left[\frac{(0.5\, m\, v_x^2)}{kT}\right]} \qquad \text{Eq. (2.68)}$$

There will be a distribution of energy in the form:

$$e^{-\left[\left(\frac{mc^2}{2kT}\right)\left(1-\frac{E_{\gamma}^{'}}{E_{\gamma}}\right)^2\right]} \qquad \text{Eq. (2.69)}$$

This gives a Gaussian distribution of width as follows:

$$\Delta = 2 \times \left(ln2\, E_{\gamma}\right)^{1/2} \times \left[\frac{2\, k\, T}{m\, c^2}\right]^{1/2} \qquad \text{Eq. (2.70)}$$

where k refers to the Boltzmann constant and T refers to the absolute temperature [109]. At room temperature, Δ takes values between 5 and 8 eV for transitions in the 5~8 MeV range. The recoil energy loss separates the emission and absorption peaks, excluding the possibility of resonant re-absorption. However, a minimal overlap can be seen between the emission and absorption lines due to the Doppler broadening effects, as shown in figure 2.13 [109].

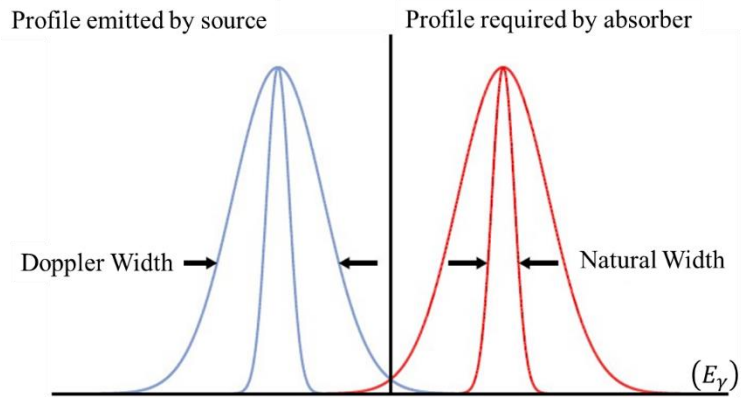

Figure 2. 13. Energy distribution of emission and absorption photons

3 NON-DESTRUCTIVE INSPECTION OF NUCLEAR MATERIALS

The isotopic signature of the NRF at the MeV scale of energy allows the technique to be applicable for a variety of applications, beyond the detection of SNMs, with reasonable sensitivity. Concepts for potential applications of the NRF were gathered from a wide variety of sources in this chapter. To help distinguish NRF from other technologies, applications were evaluated to see if they required NDI and isotopic information. We refer to NDI when we talk about sealed measurement samples or samples that cannot be accessed directly. For example, if a small portion of the sample could be destroyed, conventional technologies, such as mass spectrometry, would very certainly surpass NRF techniques. Other possible applications were chosen because NRF might provide a faster and/or less expensive method of determining isotopic composition. The following is a summary of a few of the most intriguing applications with a mention of the challenges for the NRF to be commonly applicable for each category.

3.1 Confirmation of U enrichment in UF_6 canisters

Enriched uranium is frequently delivered in canisters as UF_6. The canisters are available in a variety of sizes, ranging from a fraction of a liter to hundreds of liters. Inspection of these containers to determine that the claimed uranium enrichment is correct is difficult due to the low energy emissions of ^{235}U. The 186 keV gamma ray of ^{235}U, for example, will be suppressed by 95% in 6.5 mm of UF_6 at a density of 3 gm/cm^3. When compared to the 600 mm radius of the bigger canisters, this range is negligible. The ^{238}U signature, at 1001 keV, penetrates material much better than the ^{235}U signature. However, because ^{238}U is only one factor in figuring out enrichment, a direct measurement of ^{235}U is still desirable. Therefore, NRF has the potential to measure uranium enrichment inside a UF_6 container. The relevant energies used in NRF allow for

substantially more material penetration. NRF's relevant energies allow for far higher material penetration. The attenuation length of the 186 keV line is 30 times higher than the 1733 keV line, which is the strongest NRF line of ^{235}U. The second reason is that by increasing the intensity of the photon source, the NRF signal intensity may be raised, which is not possible with a passive measurement [110, 111]. The application's scenario is an in-field standoff measurement to determine the uranium enrichment in the canister. The canister will be around 3 meters away from both the source and the detector. The measurements will have to be completed in one hour. However, this technique has significant technological challenges, such as sensitivity across vast amounts of materials, several layers of materials, and sensitivity to small amounts of isotopes in a larger matrix.

3.1.1 Geo-sourcing of material (Cu, Pb)

In many cases, the geographic provenance of material can provide crucial information to decision-makers. Examining isotope ratios is one method of geo-sourcing a material. K. J. Moody [46] discovered a relationship between the $^{207}Pb/^{206}Pb$ ratio in aerosols and gasoline and their geographic origins. According to the same reference, the $^{18}O/^{16}O$ ratio in uranium oxide fuel is dependent on the geographic region where the UF_6 was converted to uranium oxide. For many of the isotopes of interest, the NRF process generates isotopic signatures. For example, the responses of ^{206}Pb and ^{207}Pb are around 4 MeV, while the responses of ^{16}O and ^{18}O are around 7 MeV and 6 MeV, respectively. The laboratory measurements of lead and copper are the scenarios envisioned for this application. We will look at two different scenarios: a lead sheet and a copper pipe. The measurement will have to be done on a specific day. The question being investigated is whether NRF may provide a response more quickly and simply than present approaches, which may entail extensive

laboratory work. T. Hayakawa et al. [41] reported that they could measure the ratio of $^{12}C/^{14}N$ in the shielded melamine ($C_3H_6N_6$) by comparing the NRF spectra of ^{12}C with that of ^{14}N. O. Beck et al. [45] proved that the NRF technique was able to detect the content of ^{13}C in diamond with a sensitivity that agreed well with Raman spectra. The sensitivity to lesser amounts of isotopes in a larger matrix is the technical challenge of such an application of NRF.

3.1.2 Dismantlement verification of the explosives

The NRF may be able to supply invaluable verification capabilities at two critical stages in the explosive's dismantlement process. The first stage is to confirm that the explosive that has been manufactured is indeed a threat. In general, the NRF procedure may be used to confirm the presence, form, geometry, isotopic content, and fissile mass of SNMs, as well as the presence, geometry, and separation of high explosives from fissile material. The second stage, where NRF might be incredibly valuable, is confirming that the components of the dismantled explosives are consistent with the nuclear material. Direct access to the dismantled components is not feasible since they are kept in sealed containers. NRF techniques, on the other hand, may permeate the container walls. Another benefit of NRF is the ability to achieve individual isotope selectivity. The isotopes of interest must be present in the secondary target for transmission measurements, which we call the witness target. By selecting appropriate samples, one may reduce the quantity of isotopic information available from these sorts of measurements. This capability may be critical as the isotopic content of nuclear material is considered classified by some governments [112]. The scenario for this application is a resolute, fixed system installed at a facility. Measurements need to be conducted on a time scale of hours, and the geometry can be as close as allowed by the sample geometry. However, this technique has considerable technological obstacles,

including sensitivity through numerous layers of materials, minute amounts of isotopes in the broader matrix, and enormous quantities of materials. In addition to the absence of understanding of NRF signatures of specific isotopes, such as plutonium isotopes other than ^{239}Pu, ^{6}Li, and ^{9}Be, this technique confronts a barrier in 3D isotopic mapping.

3.1.3 Direct measurement of Plutonium in spent fuel

The appropriate accounting for the ^{239}Pu content in nuclear fuel is a critical concern in safeguarding nuclear fuel. To deduce the isotopic content of the fuel, current methodologies depend on observations of long-lived and non-fissile isotopes (e.g., ^{137}Cs) combined with burn-up code calculations. The measurements confirm the operator-provided information. This method falls well short of the IAEA's need for direct and operator-independent measurements of ^{239}Pu in spent fuel [113]. The tremendous activity of spent fuel, which may potentially overwhelm an HPGe detector if suitable collimation and shielding are not addressed, is one of the obstacles to conducting experiments on it. It has been demonstrated that by carefully selecting the beam energy, NRF signatures may be generated that can be observed against the background of spent fuel [114, 115]. The inspection of a Westinghouse 17 × 17 pin assembly is the scenario for this application. The fuel is an oxide with a density of 11 gm/cm^3. Without any constraints on the measurement time, the nominal target measurement uncertainty is 2%. The distance between the detector and the used assembly is considered to be 1 meter. The technical hurdles of this approach can be summarized as the limitation of the high background rate from spent fuel, the sensitivity through massive quantities of materials, and the lack of knowledge of the NRF signatures of isotopes.

3.1.4 Self-irradiating samples

Consider a sample that is highly radioactive and has a wide range of isotopes, causing gamma rays of varying energies to be emitted. If the sample is large enough or if it is in a matrix of material, there will be a substantial down scattering of those gamma rays, resulting in a quasi-continuous distribution of photons. Those photons might trigger NRF within the sample in this situation. This geometry differs from the more common NRF setup, which involves a pencil photon beam being incident on a sample. The NRF process isotopically redirects the pencil beam such that geometry may be used to differentiate between incoming and fluorescence photons. This will not be the case in the self-irradiating sample, for instance, because the sample and source are the same. There are two techniques for resolving this scenario. In the first technique, a transmission-like measurement is used to take advantage of the energy difference between incident and fluorescent photons. If the isotope of interest is present in the sample, the energy of the photons on the resonance will be slightly below the resonance due to the nucleus's recoil. This process will create a notch in the transmitted spectrum, which can be exploited by looking for resonant scattering on a witness target, like how transmission measurements are conducted. The second technique takes advantage of known geometrical discrepancies between the sample and the matrix of material that surrounds it. Consider a sphere of ^{235}U surrounded by lead as an example. By determining the difference between spectra with a collimated detector focused on the lead and those with the same detector focused on the ^{235}U sample, one may be able to extract information about the sample's isotopic content. This approach assumes that the source releases gamma rays with energies much surpassing the resonance energy. The 9/2 state at 46.2 keV, which is produced by the down scattering of lines from the 186 keV level, might be the resonant state in the case of ^{235}U. For this application, two situations are foreseen; first,

consider the ^{235}U sphere inside a Pb shell for a moment. Second, consider a solid sphere of material that is mostly formed of iron but also contains a lot of fission products and ^{235}U. We will suppose that the measurements are done in a laboratory setting with no significant time constraints in either situation (up to a day may be taken to figure out whether or not a particular isotope is present). However, there are some technological challenges with this technology, such as establishing a mechanism to utilize the NRF signature and determining whether the scattering of the initial gamma rays generates an appropriate spectrum for NRF processes or not [111].

3.1.5 Gas samples

Air sampling and analysis can provide valuable insight into operations that produce considerable gas or aerosol outputs. The present approach typically entails treating the sample for measurements such as chemical separation. In such cases, the NRF may provide a speedier method of figuring out the isotopic content of a sample. The identification of stable isotopes is another advantage of NRF over passive measurements. There are two scenarios: a compressed air sample within a container and an aerosol sample collected on filter paper. The measurement will take place in a laboratory with a one-day measurement time limit. In terms of geometry, it will be as compact as possible [111, 116]. The sensitivity to tiny amounts in a larger matrix and to small samples is a technical challenge for such an approach.

3.1.6 Suspect material identification

When a potentially hazardous sample of material is first acquired, the first step in investigating it is to perform an initial survey to determine what the sample contains. This method can be challenging since the sample may have numerous layers of material and the specific components present may be unknown. It may be possible to conduct an initial survey of the sample using

NRF as a screening tool to acquire some insight into its contents in an NDI manner. In such a scenario, a laboratory measurement is conducted on a sample. K. J. Moody et al. [46] provided two examples of probable samples. Both of which were genuine samples that were subjected to forensic analysis. The first example was of an HEU powder that was contained in a glass ampoule that was wrapped in paper, covered by wax, and encased in a lead pig. The HEU consisted of 1.1% ^{234}U, 11.9% ^{236}U, 13.9% ^{238}U, and 72.7% ^{235}U. The second example is a bottle of thorium nitrate, with a uranium/thorium ratio of around 4%. Other isotopes orders of magnitude lower than the actinide material itself were found at trace levels in both samples. If one has direct access to this material, he might be able to employ other methodologies to conduct more sensitive testing of these minor substances. However, it is crucial to figure out how little of a sample NRF can detect in a sample. The approach's technological problems are confined to sensitivity to small amounts of isotopes in a larger matrix and through layers of materials. This approach also has a challenge in 3D isotopic mapping, in addition to a lack of understanding of NRF signatures of specific isotopes.

3.1.7 Verification of SNMs in a cargo container

The possibility of detecting dangerous nuclear material in intermodal cargo containers was one of the primary motivations for studying the potential of NRF. This application is challenging because of the cargo container's enormous dimensions; the unknown matrix of materials around the suspected SNMs, the requirement to conduct the tests fast, and the low tolerance for false-positive alerts. In this case, we will presume that another method, such as photofission or radiography, was used to locate a suspicious zone within the cargo container, and that all that remains is to confirm that the region contains SNMs [28, 117]. A stationary facility at a domestic border crossing is envisioned in the scenario.

The measurement must be conducted in a ten-minute period. The measurements will be focused on a physical region of interest inside the container that has previously been appointed. Acceptable geometries acceptable for cargo container inspection will be assumed. The SNMs will be surrounded by three different types of material matrices; an empty container to provide a baseline sensitivity; a container filled with 1.4 gm/cm^3 Celotex as an approximation for shielding from incidental material; and finally, an engineered shield made up of a moderate amount of lead and borated-polyethylene. The shielding proposed would be effective in removing 95% of plutonium neutrons and 95% of ^{238}U's 1001 keV gamma rays. ^{235}U and ^{239}Pu materials will be considered. The sensitivity to small amounts of isotopes in a larger matrix, as well as sensitivity through layers of materials, are technological obstacles in using the NRF for SNMs.

3.2 NDI techniques for nuclear material

Radiation-based methods have become standard procedures for material studies and characterization over the last century. Radiation can now be used for a wide range of applications due to technological advancements in radiation production and detection. The imaging techniques based on particle attenuation in the matter have evolved into a well-established family of treatments known as radiography. This series of procedures tries to supply information on an item's internal structure while inflicting the object with as slight damage as possible. Many radiography branches have been established based on the probing particles and their interaction with the material. Radiography attempts have been made with a variety of particles. The most popular incident probes are photons and neutrons. To obtain specific characteristics of the investigated material, the specific mechanism by which the particle interacts with the material can be utilized. The non-resonant

attenuation part can supply information on the areal density and effective atomic number, while the resonant attenuation part can supply isotope-specific information. The NDI for nuclear material refers to a set of nuclear fuel material measurement procedures or techniques. The techniques check radiation generated or emitted spontaneously from nuclear material, and they are non-destructive in the sense that they do not change the nuclear material's physical or chemical state [16]. The emitted radiation is unique to the isotope or isotopes of interest, and the intensity of the radiation is often related to the mass of the isotopes. Other methods for measuring nuclear material include taking a sample and analyzing it using destructive chemical operations. The necessity for increasing nuclear material safeguards was the primary driver for NDI development. As more nuclear material measurements were required by safeguards agencies around the world, it became clear that quick measuring procedures that did not affect the status of nuclear material objects were needed. Rapid non-destructive measurement procedures are required by the safeguards inspectors who must verify the inventories of nuclear material kept around the world. NDI techniques of SNMs are classified as passive or active depending on whether they measure radiation emitted by the material's spontaneous nuclear decay or radiation emitted by an external source. The active non-destructive inspection (ANDI) supplies an external probing means such as a neutron source or gamma-ray source, and the detection is dependent on the material's response to that probe. In passive non-destructive inspection (PNDI), the detection of SNMs is based on the natural radioactive signatures of the material. Therefore, if the material has a faint radioactive signature, b- or a-emission, the PNDI becomes unhelpful. If the signatures of the material are of high energy to penetrate any possible shielding conditions, the PNDI may be beneficial and cost-effective in the case of neutron or gamma-ray emission. Because the natural radioactive signature of the materials is uncontrollable, the

ANDI is more dependable than the PNDI. The different methods of the ANDI are described in the following sections, which will focus on photon-based radiography and will target both non-resonant and resonant methods.

3.2.1 Non-resonant attenuation-based methods

The mass attenuation coefficient is the basis for imaging methods that rely on photon interactions with matter. The relationship between the coefficient with the incident photon's energy and the material atomic number can be utilized to obtain the data needed to differentiate between various material samples. The mass attenuation coefficient for photons in the MeV energy range may be explained by three physical processes: the photoelectric effect; Compton scattering; and pair creation. When photons with energies of more than 1 MeV are considered, the photoelectric effect is ruled out. If the atomic number $z > 25$ is considered, the mass attenuation coefficient is dominated by Compton scattering for photon energies between 1 and 10 MeV and by pair production for photon energies above 10 MeV [109]. Figure 3.1 shows the mass attenuation coefficient vs incident photon energy for a wide range of atomic numbers [118].

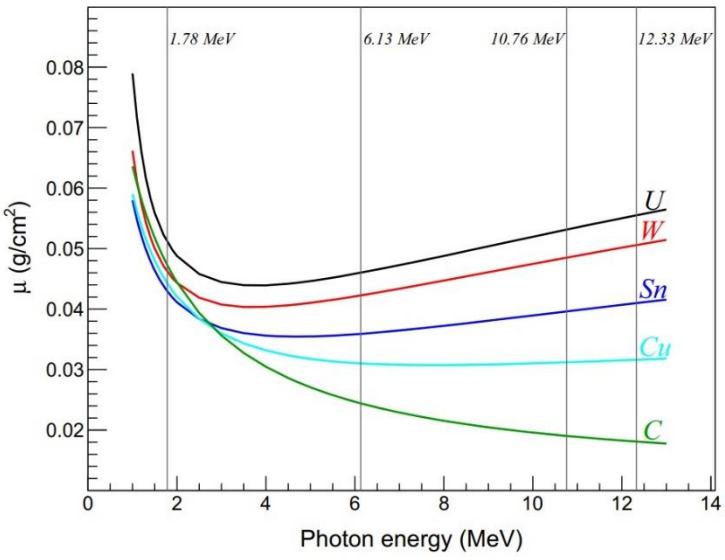

Figure 3. 1. The mass attenuation coefficient versus photon energy for many atomic number values

3.2.1.1 Photon attenuation radiography for cargo inspection

Non-destructive techniques based on x-ray or gamma-ray non-resonant attenuation are now widely employed in medical, industrial, and border control applications [119]. Cargo screening systems are used all over the world to prevent illegal items from being disguised in lawful cargo movement [120]. The photon source, the object, and the detector are the three factors that define the configuration of the measurement setup in every radiography measurement. A typical photon attenuation image is generated by counting the photons that pass through an unmodified sample material. The object is split into discrete pixels, which can be defined by the beam or by the detection system. The cone beam and the pencil beam are two limit scenarios for this kind of measurement. In the cone-beam configuration, the beam fully covers the object, and the physical discretization of the detector defines the image pixels. In the pencil-beam configuration, the image is constructed using single-point attenuation measurements collected by scanning across the width and height of the object. In addition, the image resolution is defined by the size of the beam. In practice, a combination of the two techniques is employed for cargo scanning applications. Photon attenuation radiography is now an effective technique for studying an object's internal structure. The method performs well across a broad range of atomic numbers and areal density values. Concerning the atomic number, the method does show shortcomings for complex materials, in which high z components shield low z components. There are obvious restrictions for objects that entirely attenuate the incident beam on the areal density side. Figure 3.2 shows how structural information may be extracted directly from the obtained images, which can also supply quantitative geometrical details if the measurements are performed using a well-defined setup [121].

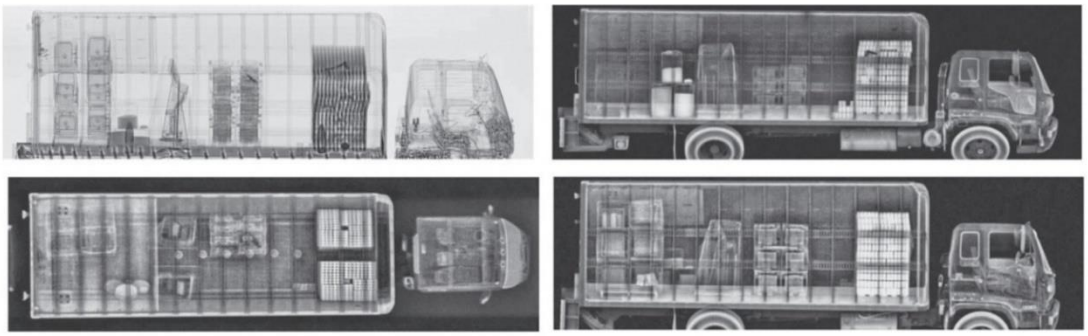

Figure 3. 2. Example of cargo x-ray images of cargo transport containers from different views [121]

Due to the tiny size of probable contraband goods in comparison to the container size, cargo screening images supply extra challenges in terms of object detection. Automated image segmentation and object identification for x and gamma-ray attenuation images is an active topic of research. There are some critical limitations to the method's ability to be widely effective. Such obtained images may show a large region of increased attenuation. However, no details about individual items can be extracted. The described method is unable to solve the atomic number, areal density, or uncertainty, meaning that it is unable to discriminate between thick-low z and thin-high z objects. This flaw leaves the method vulnerable to being deceived by a competent criminal.

3.2.1.2 Effective z-assessment with dual gamma attenuation

The dual-attenuation method is one solution to the atomic number-areal density uncertainty. The method requires taking measurements of attenuation at two different photon energies. This measurement can supply additional information about the object's atomic number and density. Figure 3.3 shows an example of a four-color segmentation used for such a measurement. Each color stands for an atomic number value. Orange stands for hydrocarbons, green stands for aluminum, blue stands for iron, and lilac stands for lead. Similar images with an areal density-based segmentation of the scanned object may also be generated using this method [122].

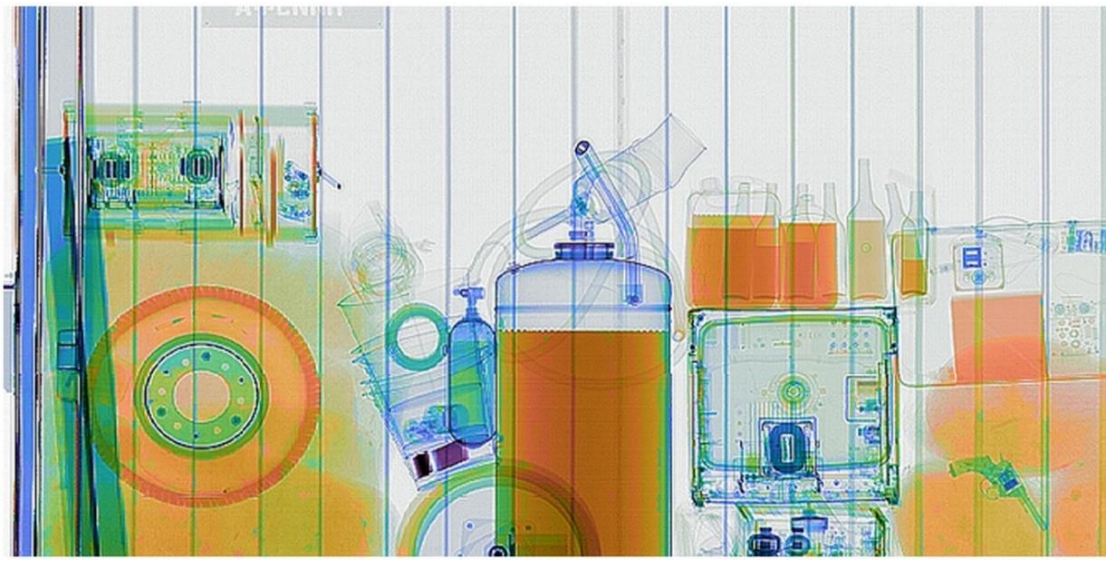

Figure 3. 3. Dual-attenuation radiography colorized image of a shipping cargo container with color assignment [122]

3.2.2 Isotopic analysis using NRF

NRF has been offered as an NDI technology that can provide a sample object's isotope-specific characterization. The method is based on detecting resonant photons created when an incident beam interacts with sample material. The photons are generated in specific nuclear transitions that can be assigned to isotopes. Typical NRF transitions are excited by photons in the MeV energy range, with increasing energies as the atomic number decreases [28]. Bremsstrahlung, which is caused by high-energy electrons colliding with a converter target, has traditionally been used to create these photon beams. Due to the continuous nature of the process, high-intensity bremsstrahlung beams may be generated with relative simplicity but with significant limits in terms of energy bandwidth. Recent technological improvements have enabled the production of quasi-mono-energetic photon beams through laser-electron scattering. The LCS gamma rays are obtained due to the interaction between a laser pulse and a relativistic electron beam through inverse Compton scattering. The photon's energy obtained after colliding with the relativistic electron can be calculated using the following formula:

$$E_\gamma = 2\,\gamma_E^2\,\frac{1+\cos\theta_L}{1+\left(\lfloor\theta_\gamma\right)^2+a_0^2+\frac{4\gamma_E E_L}{m_0 c^2}}\,E_L \qquad \text{Eq. (3.1)}$$

where ⌊ refers to the Lorentz factor, θ_L and θ_γ are the angles of the incoming and outgoing photons, E_L is the energy of the incident photon, m_0 is the rest mass of the electron, and a_0 is defined as:

$$a_0 = \frac{eE_0}{m_0 c w_0} \qquad \text{Eq. (3.2)}$$

where E_0 is the electric field, e refers to the elementary charge, c refers to the speed of light, and w_0 is the laser frequency [68]. The interaction shows a strong energy-angle correlation that can be used to obtain small bandwidth beams through collimation. The incident energy of the electrons and the collimator hole may be adjusted to optimize the beam's spectral parameters, mean energy, and bandwidth. As such, the incident photon beam can be tuned to target individual NRF resonances allowing the detection of specific isotopes inside the material. As a result, the incident photon beam may be tuned to target individual NRF resonances allowing specific isotopes to be detected within the material. The scattering setup and the transmission setup were proposed as measurement configurations for NRF isotope analysis. It will be described in full below.

3.2.2.1 Scattering measurements

The detectors in this configuration will be positioned around the object to record the beam-sample interaction. The photon flux reaching the detectors will be composed of resonant scattering, non-resonant scattering, and radioactive decays from the target. To minimize the non-resonant scattering contribution, the detectors can be positioned at backward angles to diminish the background. The inclusion of high-atomic-number filters in front of the

detectors can help minimize the low-energy element of the background even further. The scattering setup has benefits in terms of simplicity of deployment and measurement speed. However, it has some drawbacks. One of the method's major flaws is that it requires a lot of shielding to suppress the additional background for highly radioactive sample materials. Another drawback is that the method might give mistaken results for large non-homogeneous samples due to the attenuation of the resonant photons inside the material. The NRF rate for incident (E) energy from a position r within a target volume can be calculated using the following formula [123]:

$$\frac{d^2R_{NRF}}{dVdE} = N\phi(E,r)\sigma_{NRF}(E)W_e(\theta)e^{[-\mu(E_\gamma)r_0]}\left[\epsilon(E_\gamma)\frac{\Omega(r)}{4\pi}P_f(E_\gamma)\right] \quad \text{Eq. (3.3)}$$

where N is the number density for the atoms with an NRF cross-section $\sigma_{NRF}(E)$, $\phi(E,r)$ is the photon flux at the position r, $W_e(\theta)$ is the angular correlation function, E_γ is the energy of the emitted NRF photon with total attenuation $e^{[-\mu(E_\gamma)r_0]}$, $\epsilon(E_\gamma)$ is detection efficiency, $\Omega(r)$ is the solid angle of the detector, and $P_f(E_\gamma)$ is the probability that a photon E_g passes through the radiation shield. The isotopic concentration may be figured out for material analysis by finding the number density of atoms N. The precision with which the parameters of the previous equation may be assessed is attributed to the errors associated with these methods. Simulation-backed proposals for non-destructive analysis for radionuclide inspection or nuclear waste using scattering measurements have been reported in the literature [124, 125]. On the experimental side, the method has been successfully employed for the detection of ^{208}Pb shielded by iron in a single [44] and multi-pixel configuration [126], using LCS sources. O. Beck et al. [45] employed the scattering configuration to measure the ^{13}C isotopic content of natural and artificial diamonds. Figure 3.4 shows a schematic illustration of the scattering configuration.

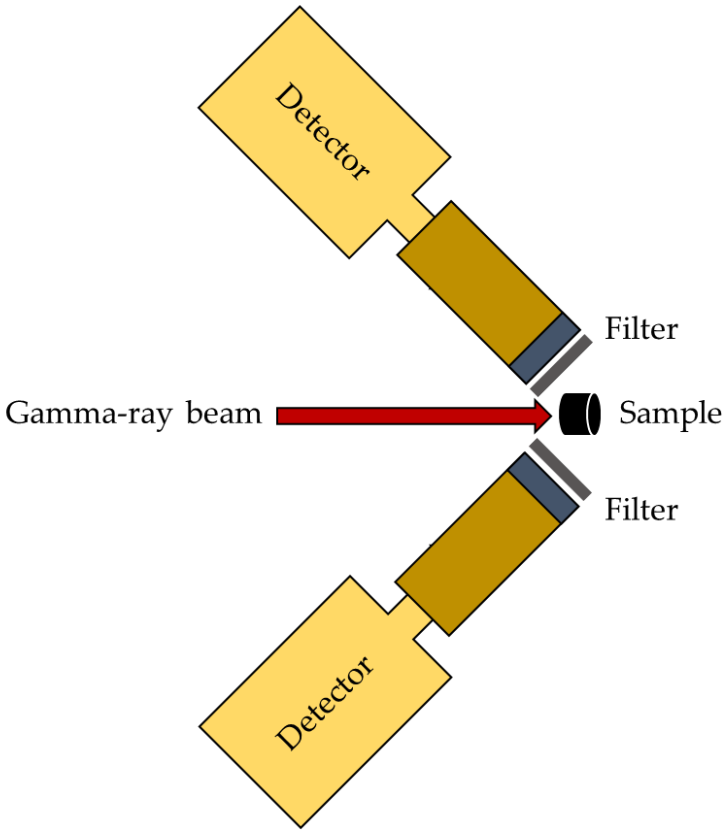

Figure 3. 4. Scattering set-up configuration for NRF-based isotope analysis

3.2.2.2 Transmission measurements

The transmission configuration, or the notch detection configuration, was developed to address some of the scattering method's limitations for NDI measurements of the isotopes of interest [28]. In this configuration, the gamma-ray beam is transmitted through the sample material and injected into a material made of the isotope of interest (witness target). The detecting system is arranged around the witness target, which is shielded from the sample material's background. The sample decay is removed from the background spectrum by decoupling the detecting system from the measured sample. Figure 3.5 shows the transmission configuration.

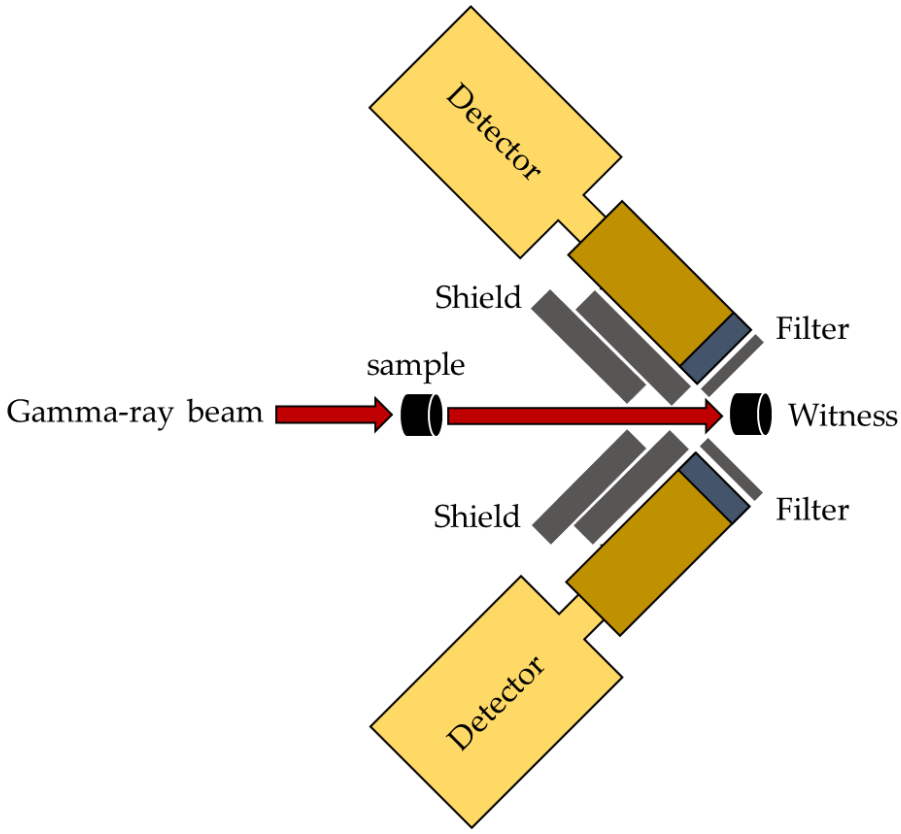

Figure 3. 5. Transmission set-up configuration for NRF-based isotope analysis

To minimize incoherent scattering, the detectors are positioned at backward angles, like the scattering configuration. A two-step measuring technique is needed for the analysis of the transmission configuration. In the reference run, the sample object is not part of the measurement setup. The detectors will measure the photons generated by the incident gamma-ray beam on the witness target. The incoming beam is initially attenuated by the sample object before hitting the witness target. This interaction will be recorded by the detection system. So, the number of resonant photons collected from the two measurements is used to obtain the isotope composition of the sample material. The separation of the sample from the detection system improves the signal-to-background ratio, which is one of the advantages of the transmission configuration. Decoupling is particularly useful if scanning a variety of different-sized items is necessary because the detection system does not require any adjustments. Two significant limitations must be considered for the

transmission configuration. First, the method needs photon transmission through the sample, which is constrained by the object's size. Second, witness material made of the same material as the isotope of interest is needed, limiting the method to isotopes for which a witness target is available. Resonance widths are less than the energy width of an incident gamma-ray beam, generally 1 eV after Doppler broadening, with gamma-ray absorption by nuclear resonance happening solely in the nuclide of interest [38]. When an isotope of interest is already present in the measured sample, resonant absorption reduces the spectral flux of the transmitted photons at the resonant energy, resulting in a narrow and severe drop (known as a notch) in the transmitted gamma-ray energy spectrum [127]. This process is illustrated in figure 3.6. Gamma rays are released from the isotope of interest when the transmitted gamma rays irradiate witness material that holds the same isotope of interest. The amount of isotope in the sample along the beam path determines the NRF yield from the witness, which is a negative exponential function of the amount of isotope in the sample.

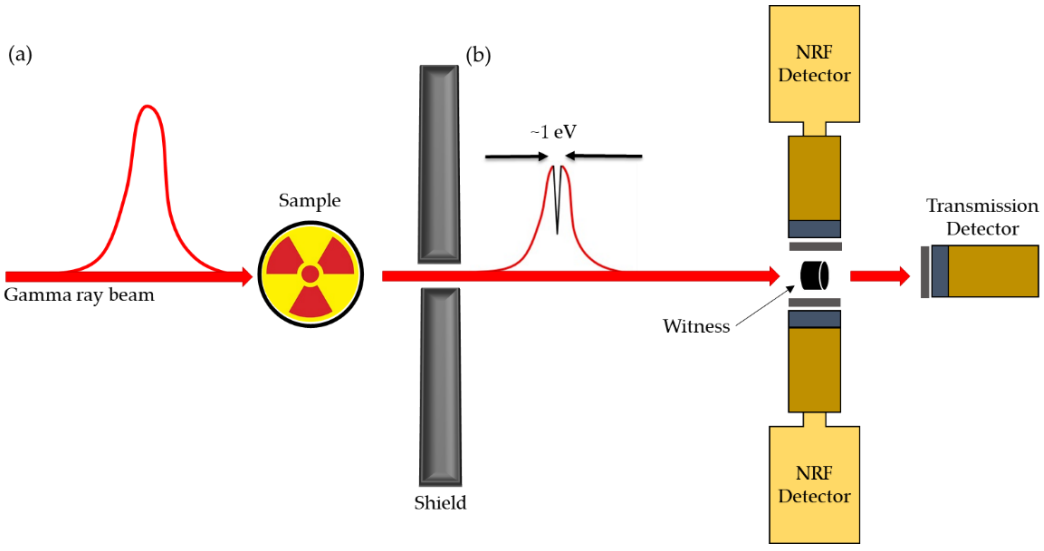

Figure 3. 6. NRF transmission method. (a) Detect resonantly absorbed portion of gamma ray by witness material. (b) Detect resonantly scattered gamma ray

To account for the notch filling, more corrections are required as compared to the scattering method. The notch filling describes the process in which photons are down-scattered from the sample to the resonant energy and interact resonantly with the witness material. The true content of the isotope of interest in the sample is underestimated if notch filling corrections are not applied. The NRF rate at the witness target position can be evaluated starting from the equation defined for the scattering measurement. An additional attenuation term must be included to account for the attenuation of the incident beam through the sample object. The attenuation in the sample holds resonant and non-resonant factors that can be calculated according to the following formula:

$$\phi_0(E) \approx \phi_i(E)\, e^{[-N\sigma_{NRF}(E)x]}\, e^{[-\mu_{atom}\, x]} \qquad \text{Eq. (3.4)}$$

where N refers to the atom number density, x refers to the sample thickness, and μ_{atom} refers to the non-resonant attenuation coefficient. The rate can be calculated by substituting the flux obtained from the previous equation as the incident flux in the scattering rate equation. The above equation can be simplified for a rectangular-shaped witness target and written as the following formula [56, 123]:

$$\frac{dR_{NRF}}{dE} = \lambda(E, t_{TD}) \left[e^{[-N\, x\, \sigma_{NRF}\,(E)]}\, \sigma_{NRF}(E)\right] \times \left[N_{WF}\phi_i(E)\, e^{[-\mu x]}\, W_e(\theta) \frac{A\epsilon}{4\pi r_d^2}\right] \qquad \text{Eq. (3.5)}$$

where A is the detector's surface area with α and $\lambda(E)$ defined as:

$$\alpha = \mu_{nr}\left(1 + \frac{1}{\cos\theta}\right) \qquad \text{Eq. (3.6)}$$

$$\lambda(E, t_{TD}) = \frac{1 - e^{[-(\alpha+\mu_{NRF}(E))t_{TD}]}}{\alpha + \mu_{NRF}(E)} \qquad \text{Eq. (3.7)}$$

where θ refers to the angle between the photon path and the detector. Experimental transmission measurements for the detection of ^{238}U in depleted uranium samples have been tried using both LCS and bremsstrahlung beams [128, 129]. The waste canister scenario is one of the applications that takes advantage of the separation between the sample target and the detection system. Experimental measurements using realistic spent fuel storage canisters with lead as a proxy material for uranium have been demonstrated by C. T. Angell et al. [130]. The transmission setup is not necessarily limited to isotopic analysis. For instance, NRF thermometry has been proposed as a method to measure ion temperatures in laser-induced plasma [131]. The principal NDI techniques are classified as gamma-ray assay, neutron assay, and calorimetry [16].

3.3 NDI – CT imaging for nuclear materials

CT is an imaging technique for reconstructing a sample's cross-sectional image from multiple projections obtained at various projection angles. CT scanning produces cross-sectional images that can be reformatted in several planes and even two or three-dimensional images that may be seen on a computer display, printed on film, or transmitted to electronic media. Gamma-ray CT scanners that use atomic interaction to attenuate x-rays are used in a variety of medical applications. It is usually the most effective way of identifying a variety of malignancies since the images allow the medical check to confirm the presence of a tumor and determine its size and location. CT scans are quick, painless, non-invasive, and accurate. It can disclose internal injuries and bleed quickly enough to save lives in emergency situations [132]. On the other hand, CT systems are used for checking luggage at airports worldwide to detect explosives [133 – 136]. Furthermore, gamma rays from radioisotopes [137], Bremsstrahlung gamma rays in the MeV energy region

[138], and quasi-monochromatic gamma rays [139] have been employed for CT scanning of high-density and high-industrial objects. Earlier studies have proposed a method for measuring CT images for high density and high-z objects using NRF to identify a specific nuclide [140, 141]. The NRF transmission method can be integrated with the CT, known as "NRF − CT", using gamma rays in the MeV energy region to obtain isotope-specific CT images, which can be used for isotope imaging inside massive materials. The NRF with LCS gamma-ray beams has been proposed as an effective modality for the NDI of hidden materials [28, 43, 137, 142, 143]. Kikuzawa et al. [44] used LCS gamma-ray beams to perform a proof-of-principle experiment for NRF nondestructive inspection. They experimentally used NRF activated by a quasi-monochromatic LCS gamma-ray beam with energy up to detect a lead block hidden beneath thick iron plates. The study was based on measuring the gamma-ray line scattered from ^{208}Pb and obtaining its one-dimensional (1D) mapping in the iron box (figure 3.7). Due to the low gamma-ray flux, this experiment was limited to the detection of a single nuclide, ^{208}Pb, and the mapping of its one-dimensional profile.

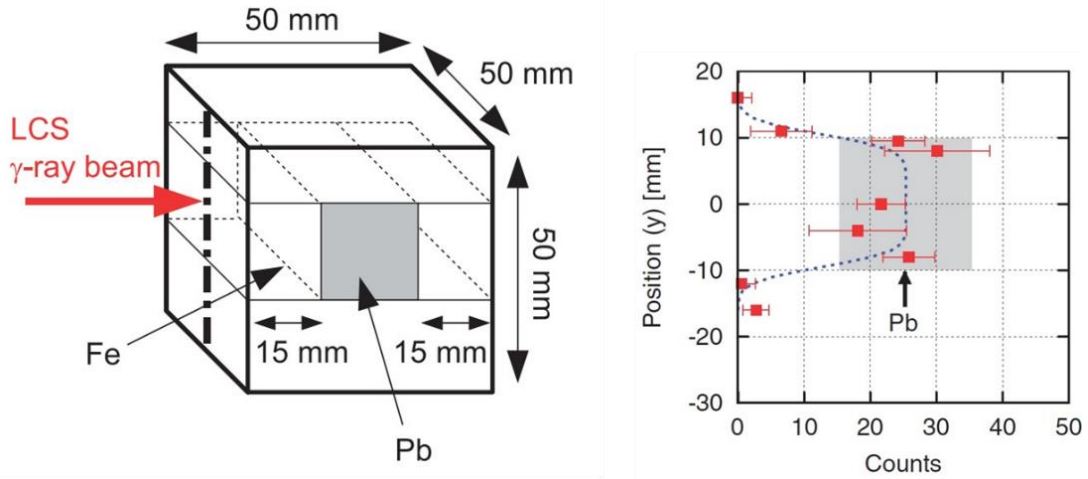

Figure 3. 7. Experimental result of isotope mapping in 1D for target made from a lead block concealed in an iron box [44]

T. Hayakawa et al. [41] proposed an inspection method for measuring molecules and chemical compounds hidden by heavy shields, such as iron, at a thickness of several centimeters using the LCS gamma rays provided from an electron storage ring TERAS [144, 145]. They measured a shielded chemical compound of melamine, $C_3H_6N_6$. H. Ohgaki et al. [146] used the LCS gamma-ray beam available in the UVSOR facility to conduct a preliminary $NRF-CT$ imaging experiment. They were able to generate LCS gamma rays with a maximum energy of 5.4 MeV and a flux of 10^7 photons/s without collimation. The gamma rays irradiated a natural lead to obtain an NRF level of 5292 keV [107] for measuring an $NRF-CT$ image for a sample made up of aluminum, stainless steel, and 8 mm diameter lead rods arranged in a 5×5 rod array. The image of the isotope of interest distribution was successfully created. However, the reconstructed images (figure 3.8) were not of sufficient quality to discuss $NRF-CT$'s capabilities.

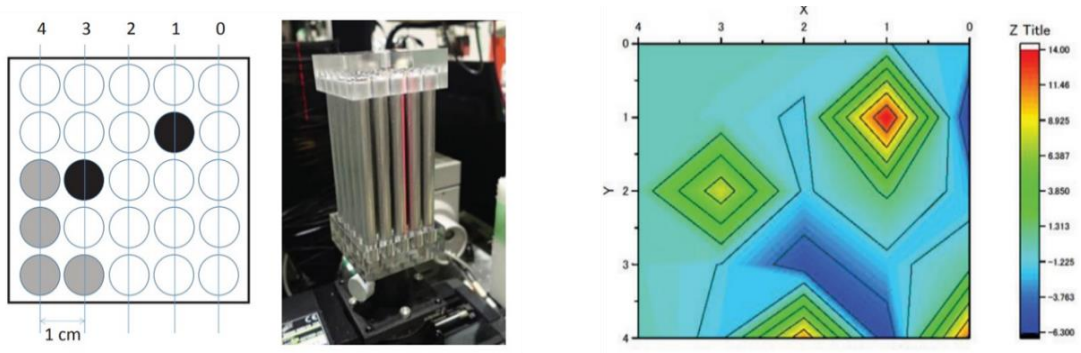

Figure 3.8. $NRF-CT$ imaging experiment for a sample made up of aluminum, stainless steel, and 8 mm diameter lead rods arranged in a 5×5 rod array [146]

One of the most impressive features of the $NRF-CT$ imaging technique is the ability to identify the specific isotope from a sample holding several isotopes. The $NRF-CT$ technique was developed further until H. Zen et al. [127] presented the experimental results of $NRF-CT$-based isotope imaging of a sample holding a lead isotope (^{208}Pb) in a natural lead rod concealed inside an iron cylinder filled with aluminum, as well as an iron rod and a vacancy. Using

the LCS gamma-ray beams available in the UVSOR − III facility, a clear tomographic image for the isotope of interest (^{208}Pb) was successfully obtained (figure 3.9). H. Zen's study clearly proves the possibility of isotope-specific CT imaging based on nuclear resonant attenuation, which they expect to become a practical approach once the next generation of incredibly powerful LCS gamma-ray sources becomes accessible. They also discussed the expected measurement time in the next generation of extremely high flux LCS gamma-ray sources, because increasing the gamma-ray flux is the key to reducing the required measurement time at one observation point and obtaining CT images with higher resolution at a reasonable measurement time.

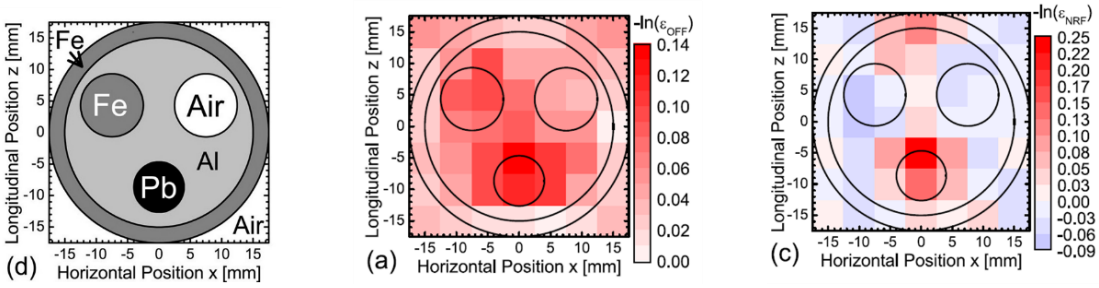

Figure 3. 9. 2D NRF − CT image of the ^{208}Pb isotope in a natural lead rod concealed inside an iron cylinder filled with aluminum [127]

4 EXPERIMENTAL PROCEDURES

4.1 Implementation of NRF measurements

The photon source and the detecting system are the two most important components of the NRF technique. Proper selection of those components is essential for the implementation of the NRF technique in the NDI measurements. In the following sections of the current chapter, we will go over these components in more detail.

4.1.1 Source of photons

The optimum source of photons for the NRF measurement should meet the following criteria: high flux density, high monochromaticity, and photon energy tunability. There are many methods to generate gamma rays with these kinds of features. The source of photons to investigate NRF has traditionally been a high-energy bremsstrahlung source [37]. The bremsstrahlung source's photon spectrum is a continuous energy distribution that extends to the electron beam's maximum energy in which photons are produced because of an electron beam with energy in the MeV range colliding with a heavy material (radiator), causing them to slow down. Therefore, severe background and high Compton continuums are always seen in an NRF measurement. However, this source has the drawback of being unable to create an NRF signal using a significant portion of the photon flux. Furthermore, this flow enhances the sample dosage as well as the background of the measurement. Gamma rays released by radioactive sources or nuclear reactions could provide a high-flux photon source with limited bandwidth. However, there was a problem that the energy and the width of the resonant level did not match the gamma-ray energy and width of the photon's source [90]. Many researchers have utilized Compton scattering to tune the energy of a gamma-ray source by changing the scattering angle. However, the source's intensity is reduced. One of the more

common techniques is the LCS gamma rays, which will be described in the following section.

4.1.1.1 Laser Compton Scattering Interaction

In the laser Compton scattering interaction, the collision between a high-power laser beam and a relativistic electron beam generates gamma-ray photons [147]. Figure 4.1 shows the mechanism of the laser Compton scattering interaction. Let us assume that a laser photon with an energy of E_p collides with a relativistic electron with an initial energy of E_e at an incident angle of θ_p. The energy of the incident laser photon is up-converted to the scattered gamma-ray photon (E_γ) which is expressed as the following formula:

$$E_\gamma = \frac{E_p \left[1 + \frac{v}{c} cos\left(\theta_p\right)\right]}{1 - \frac{v}{c} cos\left(\theta_\gamma\right) + \frac{E_p}{\lfloor m_0 c^2} \left[1 - cos\left(\theta_s\right)\right]} \qquad \text{Eq. (4.1)}$$

where m_0 is the rest mass of the electron, v is the electron velocity within the storage ring, c is the speed of light, θ_γ is the scattering angle of the emitted gamma photons, θ_p is the is the angle between the incident laser photon and the scattered gamma photon, and $\lfloor$ is the Lorentz factor which can calculated as:

$$\lfloor = \frac{1}{\sqrt{1 - \left(\frac{v}{c}\right)^2}} \qquad \text{Eq. (4.2)}$$

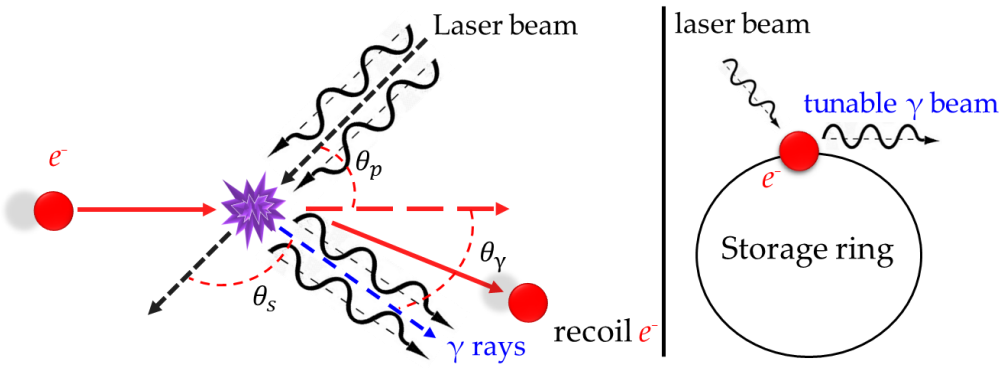

Figure 4. 1. laser Compton scattering interaction

To obtain the maximum energy of the scattered gamma-ray photons, the head-on collision, as shown in figure 4.2, between the incident laser beam and the relativistic electrons [148] will be considered in which the photons from the laser are deflected 180° by the high-energy electron beam with hundreds of MeV in energy to create MeV-scale photons in these sources. Therefore, the LCS gamma-ray energy in equation (4.1) can be simplified as the following formula:

$$E_{\gamma\,max} = 4\,E_p\,\text{ł}^2 \qquad \text{Eq. (4.3)}$$

According to the previous equation, the energy of a laser photon is up-converted to approximately 4ł^2 times greater energy by interacting with the relativistic electrons.

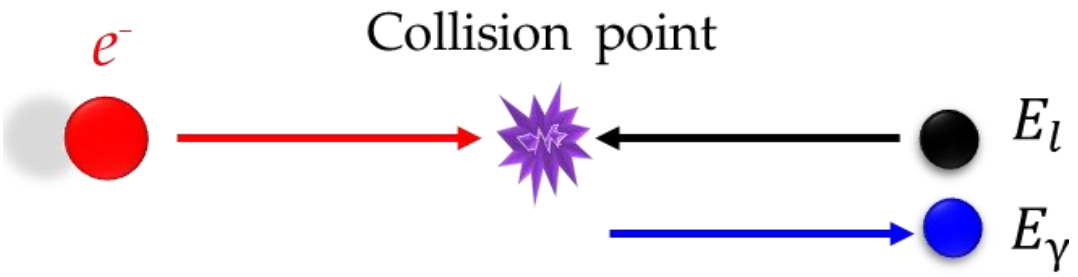

Figure 4. 2. The incident laser photon colliding head-on with a relativistic electron

The LCS gamma ray is a quasi-monochromatic photon source that provides an energy-tuning photon beam as well as a monochromatic energy distribution with 1% energy speared [147, 149]. The energy of the electron beam, the energy of the laser wavelength, and the scattering geometry, which includes the collision and scattering angles, all influence the energy of the generated gamma rays [150, 151]. Although this source of photons provides a significantly higher fraction of incident photons within the resonance than a bremsstrahlung source, it is also a far more complicated instrument. A ruby laser was used to generate the LCS gamma rays (600 MeV) in the first

demonstration experiment at the Lebedev Physical Institute of the Academy of Science synchrotron [152]. The LCS gamma rays in the MeV energy range are currently available at many facilities around the world for basic research and applications. These facilities can fix scattering geometry and laser wavelength. Thus, the energy of the generated-ray beam is controlled solely by the electron beam energy [142, 153 − 160]. In a different installation, the energy of the generated gamma-ray beam is adjusted by the scattering geometry that uses a set electron beam energy and laser wavelength [161, 162]. The unique features of the LCS gamma rays, such as quasi-monochromaticity, energy tunability, excellent directivity, and high polarization, lead to a wide range of usage in nuclear physics and the NDI analytical applications. One of the most intriguing uses for the LCS gamma rays is non-destructive isotope imaging using NRF [43, 142]. Such kind of isotope imaging techniques was demonstrated at the electron storage ring TERAS at the National Institute of Advanced Industrial Science and Technology in Japan (AIST) [44]. Unfortunately, the TERAS facility was damaged and shut down after the Great East Japan Earthquake in 2011. The High-Intensity Gamma-ray Source (HIγS) located at Duke University in North Carolina, USA, is the most powerful facility for generating LCS gamma rays [151, 163]. It is an example of a narrow bandwidth source. The electron beam energy and laser wavelength are both variables in this facility, while the geometry is fixed to the backscattering case. It can generate gamma rays with energies up to 100 MeV and a flux density of 1000 photons/s/eV. A very high-intensity LCS facility based on an energy recovery linear accelerator has recently been proposed at the Los Alamos Shufflers with a photon flux density of 10^7 photons/s/eV [164]. B0L1 is a beamline in the NewSUBARU at the University of Hyoho, Japan, dedicated to the development of novel light sources and their applications [165]. It is being used to generate LCS gamma rays with energies ranging from 1 to 40 MeV. The NewSUBARU's gamma-ray

beam is a one-of-a-kind light source with tunable energy, quasi-monochromaticity, tunable polarization, and beam directivity that has been employed in a variety of research, including photonuclear reaction, electron pair production, nuclear transmutation, and CT imaging [165]. The Extreme Light Infrastructure—Nuclear Physics (ELI – NP) in Romania is currently building a new LCS gamma-ray facility. The spectral density flux of the LCS gamma-ray beam is expected to be in the range of 5000 photons/s/eV, which is suitable for practical application [166]. The development of the LCS gamma-ray source in the UVSOR – III facility has been proposed to perform fundamental research on the NDI for isotopes. Since the experimental procedures for the current studies were conducted at the beamline BL1U in the UVSOR – III facility, we will describe the details of the LCS gamma-ray beam generation within this facility in the following sections.

4.1.1.2 LCS gamma rays in the UVSOR – III facility

The phrase "UVSOR" is an acronym for "ultraviolet synchrotron orbital radiation." It is a compact and low-energy synchrotron light source located in the Institute of Molecular Science of the National Institutes of Natural Sciences in Okazaki, Japan. It is regarded as the world's brightest low-energy synchrotron light source. The third-generation synchrotron "UVSOR – III" features an electron storage ring with a circumference of 53 m and experimental stations on 6 undulators and 8 dipole beamlines. The energy of the electrons circulating in the ring is designed to be 750 MeV. This facility is used by many researchers all around the world for a broad variety of applications and experiments. UVSOR – III is made up of 4 long straight portions (4 m) and 4 short straight portions (1.5 m). One of the long straight portions of the UVSOR – III facility is the beamline named "BL1U". It focuses on the research and development of novel photon sources such as free-electron

lasers (FEL) in the visible to deep UV range, coherent harmonic generation in the deep UV and VUV, LCS gamma rays, and undulator radiation with various polarization properties such as optical vortex beam and optical vector beam. The BL1U has a dual polarization variable undulator system with a buncher section that can be used for both an FEL oscillator and a VUV CHG. It also has a synchronized femtosecond laser system, which is utilized for a variety of applications, including LCS gamma-ray beams [148]. The development of the LCS gamma-ray source at the UVSOR − III facility's storage ring has been proposed to conduct the experimental procedures for the current dissertation's studies for non-destructive isotope imaging research. Recently, we upgraded the old laser source used in the prior system [127] with a new one capable of doubling the laser power by ten times as a kind of development for the parameters of the generated LCS gamma rays, where the generated flux was ten times higher. The new laser source is a Tm-fiber laser (TLR-50-AC-Y14, IPG Laser GmbH, Köttinger Weg 188, Wissen, Germany). This laser source has advanced parameters for the laser beam compared with the old system [127], such as the lasing wavelength of 1.896 μm, the spectral linewidth of 0.7 nm, the beam quality M^2 of 1.05, and the maximum average power of 50 Watt (W). The laser beam was randomly polarized during the run in the continuous-wave (CW) operation mode [168]. The development of this isotope imaging system was based on a first-generation CT scanner [169]. Figure 4.3 shows a schematic of the beamline BL1U [167] followed by table 4.1, including a list of the main parameters of the UVSOR − III storage ring.

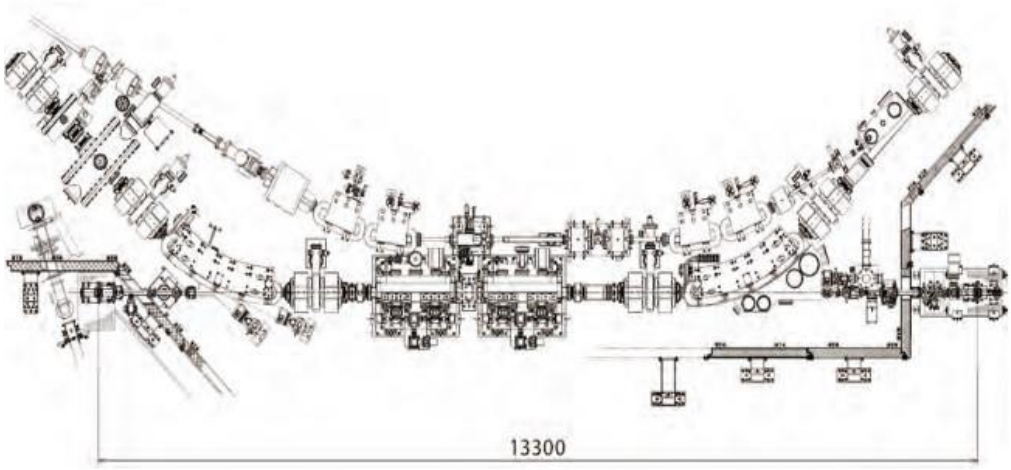

Figure 4. 3. Schematic of the beamline BL1U in the UVSOR − III facility [167]

Table 4.1 The UVSOR − III storage ring's main parameters

The electron beam energy	746 ± 1 MeV* (measured)
• Current in the normal operation • (Top-up Mode)	• 300 mA (multi-bunch) • 50 mA (single-bunch)
Natural Emittance	17.5 nm-rad
Storage Ring's Circumference	53.2 m
RF Frequency	90.1 MHz
Harmonic Number	16
Bending Radius	2.2 m
Straight Section	• 4 portions (4 m) • 4 portions (1.5 m)
Energy Spread	5.26×10^2 %
Natural Bunch Length	128 ps

The generated LCS gamma-rays' distinctive characteristics, such as maximum gamma-ray energy and total flux at the beamline BL1U in the UVSOR − III facility, are discussed below.

4.1.1.2.1 Energy of the LCS gamma rays in the UVSOR − III facility

In the case of electromagnetic waves, the relationship between wave speed (V), wavelength (λ), and frequency (v) can be expressed as follows:

$$V = \lambda \times v \qquad \text{Eq. (4.4)}$$

where the speed of the electromagnetic waves $V = 2.99792458 \times 10^{10}$ cm. s^{-1}, and the laser wavelength of the new source $\lambda = 1.896$ μm. As a result, frequency v can be calculated as:

$$v = \frac{V}{\lambda} = \frac{2.99792458 \times 10^{10}}{1.896 \times 10^{-4}} = 1.58 \times 10^{14}\ \text{Hz} \qquad \text{Eq. (4.5)}$$

The energy carried by a single photon is known as photon energy. The quantity of this energy is directly proportional to the photon's electromagnetic frequency according to the following formula:

$$E_p = hv \qquad \text{Eq. (4.6)}$$

where $h = 6.626 \times 10^{-34}$ J. Hz^{-1} is the Planck constant. Then, the energy of the incident laser photon can be calculated as:

$$E_p = (1.58 \times 10^{14}) \times (6.626 \times 10^{-34}) = 1.05 \times 10^{-19}\ \text{J} \qquad \text{Eq. (4.7)}$$

By converting the obtained energy value from Joule (J) unit to eV unit, the energy value of the laser photon will be as follows:

$$E_p = 1.05 \times 10^{-19} \times 6.242 \times 10^{18} = 0.6539\ \text{eV} \qquad \text{Eq. (4.8)}$$

Since the rest mass of the electron $m_0 = 9.12 \times 10^{-28}$ gm, and the energy of the electron beam $E_e = 746$ MeV [148], we could calculate the electron beam speed within the storage ring as:

$$V = c \times \sqrt{1 - \frac{m_0 c^2}{E_e + m_0 c^2}} = 2.99792387 \times 10^{10}\ \text{cm. s}^{-1} \qquad \text{Eq. (4.9)}$$

Therefore, the Lorentz factor can be calculated as:

$$\lfloor = 1460.8856 \qquad \text{Eq. (4.10)}$$

According to the obtained values of the laser photons' energy in equation (4.8) and the Lorentz factor in equation (4.10), we could calculate the energy of the scattered gamma-ray photons in the case of the head-on collision from equation (4.3) as:

$$E_{\gamma max} = 5.54 \text{ MeV} \qquad \text{Eq. (4.11)}$$

This energy of the generated gamma rays is able to excite the $J^{\pi} = 1^{-}$ state at 5.512 MeV of ^{208}Pb (the isotope of interest in our studies).

4.1.1.2.2 The flux of the LCS gamma rays before collimation

To compute the total flux (F_{γ}) of generated gamma rays, we shall utilize T. Suzuki's formula [170] as follows:

$$F_{\gamma} = \left[2cfN_e\lambda_p\left[\frac{\theta_p}{2}\right]\int_{-\infty}^{\infty}\rho_e\,(x,y,z,t)\rho_p\,(x,y,z)\,dx\,dy\,dz\,dt\right]\times\sigma(\theta_{\gamma}) \qquad \text{Eq. (4.12)}$$

where c refers to the speed of light, f is the collision's number per unit time, N_e is the electrons' number in bunch, λ_p is the density of laser photons, ρ_e is the electron beam's distribution function, ρ_p is the laser beam's distribution function, and $\sigma(\theta_{\gamma})$ is the Compton scattering's cross section in the scattering angle of θ_{γ}. In the case where the electron beam and laser beam have a gaussian distribution and make a head-on collision on the z-axis, the previous equation (4.12) can be rewritten as:

$$F_{\gamma} = \frac{fN_e\lambda_p\sigma(\theta_{\gamma})}{\pi}\int_{-\frac{1}{2}}^{\frac{1}{2}}\left[\left(\sigma_{xe}^2+\sigma_{xp}^2\right)\left(\sigma_{ye}^2+\sigma_{yp}^2\right)\right]^{-\frac{1}{2}}dz \qquad \text{Eq. (4.13)}$$

where σ_{xe} and σ_{ye} refer to the RMS electron beam size in both horizontal and vertical directions, respectively, and σ_{xp} and σ_{yp} as well refer to the RMS laser

beam size in the horizontal and vertical directions, respectively. Under the experimental conditions of the UVSOR − III facility [148], the number of electrons in a single revolution per unit current may be given as follows:

$$\frac{N_e}{I_e} = 1.1 \times 10^{12}\ A^{-1} \qquad \text{Eq. (4.14)}$$

where I_e is the beam current. The collision rate f is a value of 5.635 MHz. Therefore, the laser photon line density can be expressed as:

$$\lambda_p = \frac{P}{e \times c \times E_p} \qquad \text{Eq. (4.15)}$$

where the symbols P and e refer to laser power and elementary charge, respectively. According to the previous equation (4.15), the laser photon line density per unit of power is figured out as follows:

$$\frac{\lambda_p}{P} = 3.3 \times 10^{10}\ (\mathrm{m^{-1}W^{-1}}) \qquad \text{Eq. (4.16)}$$

For simplicity, we assume constant electron beam size and laser beam size in the collision region as $\sigma_{xe} = 420$ μm, $\sigma_{ye} = 15$ μm, $\sigma_{xp} = 1.5$ mm, and $\sigma_{yp} = 1.5$ mm [171]. Then the flux equation can be written as:

$$F_\gamma = \frac{f\ N_e\ \lambda_p\ \sigma\left(\theta_\gamma\right) r}{\pi} \times \left[\left(\sigma_{xe}^2 + \sigma_{xp}^2\right)\left(\sigma_{ye}^2 + \sigma_{yp}^2\right)\right]^{-\frac{1}{2}} \qquad \text{Eq. (4.17)}$$

where r is the length of the interaction region, which in the UVSOR − III storage ring is 6.3 m. In the case of laser Compton scattering with a high-energy electron, we may assume the cross-section of the Compton scattering is almost equal to the cross-section of the Thomson scattering, which is the low energy limit of the Compton scattering, 6.652×10^{-29} m^2. The highest overall gamma-ray flux is estimated to be 1.6×10^8 photons/s with 100% energy bandwidth under the maximum condition of operation in the UVSOR − III facility with an electron beam current of $I_e = 300$ mA and the maximum power of the laser

source is $P = 50$ W. Under current developments in the gamma-ray source in the UVSOR − III facility, the quality of the generated LCS gamma rays is sufficient to execute a basic investigation into non-destructive isotope imaging. The characteristics of the upgraded LCS gamma rays are shown in table 4.2.

Table 4.2 The upgrading of the LCS gamma-ray beam source in UVSOR − III

	Parameter	Old conditions [127]	Current conditions
Laser source	Model	AP-Tm-1950-SM-05-LP	TLR-50-AC-Y14
	Company	AdValue Photonics Inc.	IPG Laser GmbH
	wavelength	1.94 μm ($E_p = 0.6375$ eV)	1.896 μm ($E_p = 0.6539$ eV)
	Maximum power	5 W	50 W
	Polarization	Linearly	Randomly
	Spectral line width	$<$ 1 nm	0.7 nm
	Beam quality	$M^2 <$ 1.1	$M^2 <$ 1.05
LCS gamma-ray beam	Maximum energy	5.414 MeV	5.54 MeV
	Total flux[1]	1.6×10^7 photons/s	1.6×10^8 photons/s

4.1.1.2.3 The total flux of the LCS gamma rays after collimation

The energy of the scattered LCS gamma-ray beam photons depends on their scattering angle [171]. Therefore, a lead collimator with a quadrangular prism shape and a circular hole (1 mm diameter) was positioned in the path of

[1] The total flux refers to the calculated values before the collimator

the gamma-ray beam to define the diameter and energy spectrum of the LCS gamma-ray beam on the investigated sample and obtain a quasi-monochromatic gamma-ray beam. The dimensions of the quadrangular prism shape were 200 mm in length, 100 mm in width, and 100 mm in height. In a subsequent investigation of this dissertation, we upgraded our experimental set-up system to include a new collimator with a wider circular hole (2 mm diameter), which resulted in an increase in the LCS gamma-ray beam flux. The LCS beam has a tiny divergence (order of 10^{-3}). Therefore, the LCS gamma-ray beam diameters at the examined sample were roughly 1 mm and 2 mm, respectively, while employing the collimator with a hole diameter of 1 mm or 2 mm. Figure 4.4 depicts the gamma-ray spectrum and flux of the LCS gamma rays at the investigated sample as determined by the EGS5 Monte Carlo simulation [172], which considers the electron beam emittance, energy spread, special angular distributions, and linewidth of the laser beam [173].

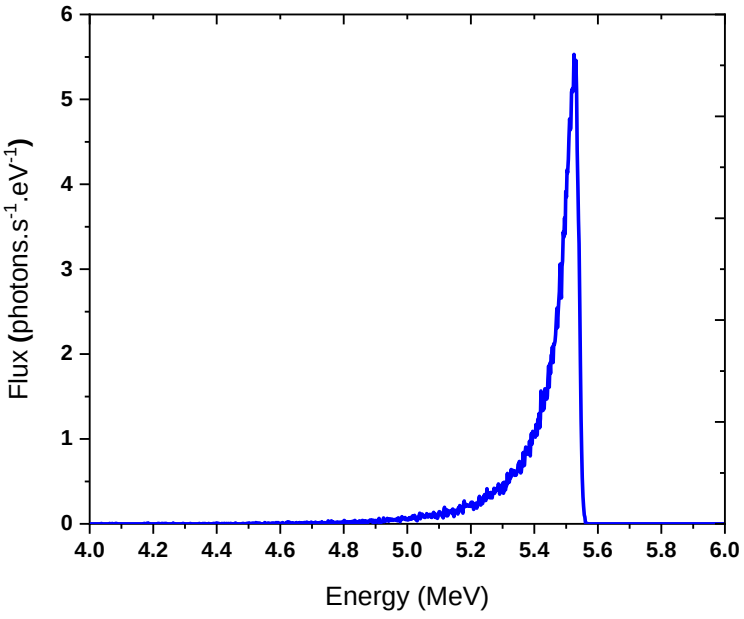

Figure 4. 4. Simulation of LCS gamma-ray spectra after 1 mm collimation using EGS5 Monte Carlo simulations [173]

After collimation of 1 mm, the flux of the LCS gamma-ray beam was calculated to be 5.5 photons/s/eV at the maximum energy of 5.54 MeV, with a 1.1% energy bandwidth at the FWHM. The energy distribution in the gamma-ray spectrum reveals characteristic properties of the LCS gamma-ray beam, such as a steady increase at low energies and a dramatic decrease at high energies. The flux of the LCS gamma-ray beam was predicted to be 10 photons/s/eV at the maximum energy of 5.54 MeV after collimation of 2 mm, with 2.9% energy bandwidth at the FWHM. Reference [171] lists the predicted gamma-ray spectra for different hole sizes of collimators calculated from numerical simulation.

4.1.2 Measurements system

Gamma rays, like visible light, are made up of photons, which are energy packets. On the other hand, gamma-ray photons have millions of times the energy of visible light photons. The detection of gamma rays can be performed by observing their effects on the matter [174]. A gamma-ray photon can either collide with an electron and bounce back, or it can move an electron to a higher energy level (photoelectric ionization). Furthermore, because gamma rays contain so much energy, some of it may be directly transformed into matter by forming an electron and another particle called a positron (pair production). All of these interactions cause electrons to move in some way, creating an electric current. The energy and direction of the original photon may then be estimated by amplifying and measuring these currents. There are two main categories of gamma-ray detectors. Detectors in the first category are known as spectrometers or photometers, which can be used in optical astronomy. These detectors are basically "light buckets," capturing as many photons as possible from a region of the sky that includes the object of interest. In these detectors, scintillators or solid-state detectors are often utilized to convert gamma rays

into optical or electrical signals that may be recorded. Detectors in the second category, which are called imagers, are capable of performing the difficult task of gamma-ray imaging. These detectors either depend on the nature of the gamma-ray interaction process, such as pair production or Compton scattering, to compute the arrival direction of the input photon, or they use a device like a coded mask to allow an image to be reconstructed [48].

4.1.2.1 The high purity germanium detectors (HPGe)

In general, the detectors for gamma rays measure the photons generated by the interaction of the incident photon beam with the target material [174]. Both the NRF process and normal electronic processes in which the incoming photon interacts with the sample's atomic electrons produce scattered photons. The typical NRF measuring setup uses HPGe detectors due to the narrow energy width of the resonances. For the requisite MeV range of photons, these detectors provide both excellent resolution and great intrinsic efficiency. However, because the HPGe's typical energy resolution is roughly 2 keV, which is 3 to 6 orders of magnitude wider than the NRF level, far superior energy resolution detectors are required. Unfortunately, even with HPGe detectors, there is another constraining factor: detection rates. HPGe detectors have a typical maximum counting rate of roughly 10 kHz. An NRF interaction, on the other hand, provides a high background that rapidly boosts the counting rates when employing the available photon sources. The type of photon source is limited by the rate constraint of HPGe detectors. Estimating the photon's energy is essential for NRF measurements. A pileup event, or accumulation, occurs in the detector if the scattered photon rate is too high. This pileup lowers measurement quality by eliminating events from the peak and increasing the background levels. A continuous photon source on the time scale of detector response time is widely utilized to minimize the problems of pileup events

(time structure faster than a microsecond). As a bremsstrahlung gamma-ray source, a CW electron beam is usually utilized. Unfortunately, because most electron accelerators are pulsed, with a temporal structure on the millisecond scale, this constraint limits the research facilities in which these measurements may be performed.

4.1.2.2 The Scintillation detectors

Although scintillation detectors may operate at frequencies up to MHz, their energy resolution is an order of magnitude poorer than the HPGe detectors [175]. The development of lanthanum halide scintillation detectors has been influenced by recent developments in scintillation materials, resulting in improved energy resolution. We preferred the $LaBr_3$(Ce) scintillation detector due to a better energy resolution, 2.7% at 0.662 MeV, than the NaI(Tl) scintillation detector, whose typical energy resolution is approximately 6% to 8% at 0.662 MeV. In addition, the availability of a high counting rate of the $LaBr_3$(Ce) scintillation detector due to the short decay time is suitable for our measurement. The intrinsic radiation of the $LaBr_3$(Ce) scintillation detector contributes significantly to the background radiation in the region below 1.6 MeV [176], which is far below our energy of interest (~ 5.5 MeV). On the other hand, scintillation detectors run at room temperature, and detector arrays make it simple to create large detection areas. Consequently, the $LaBr_3$(Ce) detectors meet several criteria for a reliable NDI detection system in NRF measurements with the LCS gamma rays, despite their low energy resolution. Another essential factor that should be considered is the detector time resolution, especially when the photon source has a noticeably fleeting time structure (nano-second scale). The time resolution of the $LaBr_3$(Ce) detectors is around 300 ps, whereas the time resolution of the HPGe detectors is about 500 ns.

4.2 CT Sample description

A cylindrical aluminum container of 20 mm in height and 25 mm in diameter was used as a specimen holder for the CT sample in all of the experiments in the current dissertation. Three circular holes of a similar size of 6.1 mm were drilled into the holder body at a pitch angle of 120°. Different types of materials have been used to conduct the experiments, such as iron (Fe) and aluminum (Al). In addition, two enriched lead isotopes (^{206}Pb purity > 93.3% with less than 1% of ^{208}Pb and ^{208}Pb purity > 97.8% with less than 1% of ^{206}Pb). Furthermore, some of the holder apertures were left empty, and the air was considered a material among the examined materials. These varied materials were filled inside the holder's body in a different arrangement according to each requirement goal. These arrangements will be discussed further in the following chapters of this dissertation. Figure 4.5 shows the (a) structure and (b) a photo of the CT sample holder.

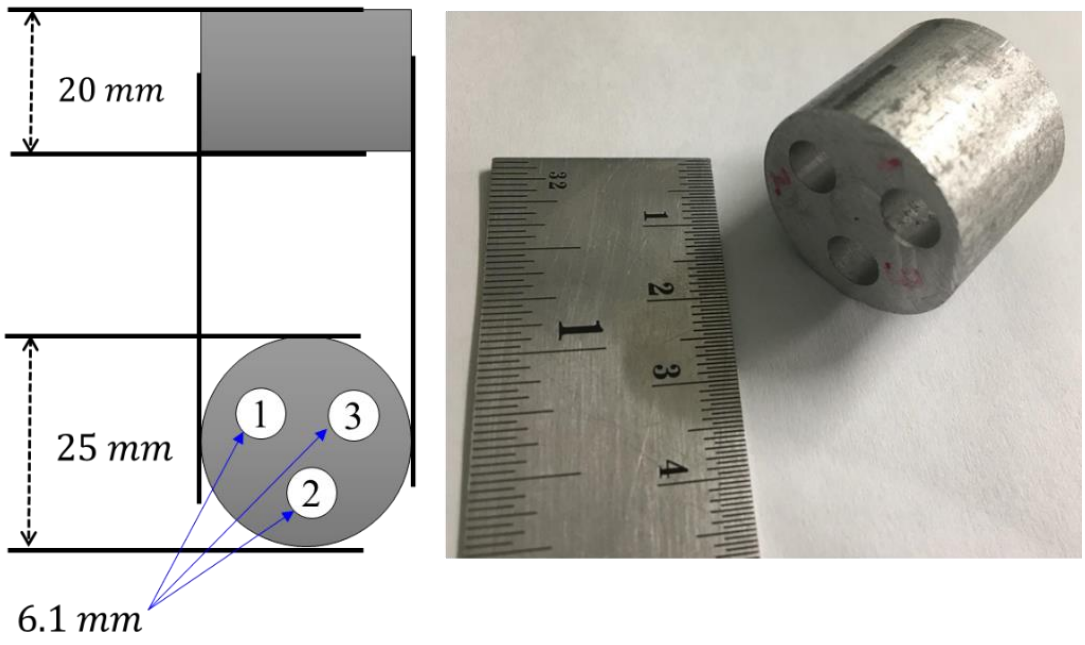

Figure 4. 5. (a) CT sample holder structure. (b) CT sample picture

5 ISOTOPE IMAGINING IN TWO-DIMENSIONS

5.1 Overview

The goal of this work was to verify the isotope selectivity of the NRF − CT imaging technique for two different enriched lead isotope rods (^{208}Pb and ^{206}Pb). Because these two materials have the same gamma-ray attenuation in atomic processes, the standard CT imaging techniques based on the atomic attenuation of gamma rays cannot differentiate them. Since the NRF cross-section at 5.512 MeV of ^{208}Pb is 2 times wider than that at 5.292 MeV, the energy of the gamma-ray beam was raised to permit excitation of $J^{\pi} = 1^{-}$ state at 5.512 MeV of ^{208}Pb. In comparison to the prior system [127], we were able to generate a 10-fold intensity of the LCS gamma-ray beam after upgrading the laser source to a new one with advanced capabilities.

5.2 The experimental procedures for the 2D NRF − CT imaging

5.2.1 The CT sample and scanning plan in 2D

The cylindrical aluminum holder was utilized as a CT sample after filling two of its apertures with two rods of ^{206}Pb and ^{208}Pb, while the third aperture was left as an air vacancy. Each lead rod was cylindrical, measuring 6 mm in diameter, 18 mm in height, and 6 gm in weight. The sample was positioned on a controllable two-axes traveling stage for scanning in 2D. The scanning was performed in the horizontal direction (x-direction) with a step size of 2 mm in the range of −14 to 14 mm, and in the rotational direction (θ-direction), with 30° increments from 0° to 150° around the y-axis. Figure 5.1 shows the scanning geometry of the sample in both directions of (x and θ). In addition to one scan in the absence of the investigated sample, 90 data points, (15 steps along x-direction × 6 steps along θ-direction), were acquired. The average measurement time for a single position of scanning was 40 minutes, and the

overall measurement time for the 2D NRF − CT image was 60 hours. Table 5.1 summarizes the scanning procedures for the NRF isotope CT imaging in 2D.

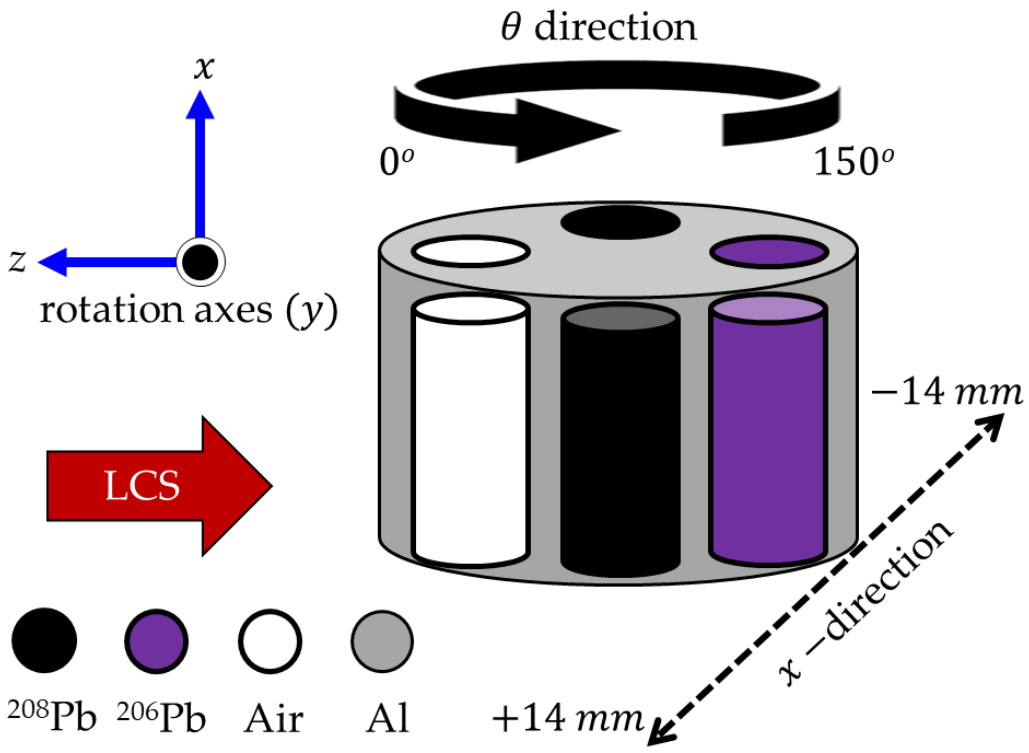

Figure 5. 1. CT sample geometry for the NRF − CT imaging in 2D, including scanning geometry in the x-direction and θ-direction

Table 5.1 Scanning procedures for the CT sample in 2D

	Step size	Range	No. of points
θ	30^o	0^o~150^o	6
x	2 (mm)	$-14 \sim +14$ (mm)	15
Acquiring Time for one position			40 minutes
Overall measurement time			60 hours

5.2.2 The parameters of the LCS gamma-ray beam

We employed the Tm-fiber laser source with a typical power of 36 W (CW) with random polarization to generate an LCS gamma ray with a maximum energy of 5.54 MeV via a head-on collision with an electron beam at a

maximum energy of 746 ± 1 MeV and beam current of 300 mA at the UVSOR $-$ III storage ring's beamline BL1U. The energy of the generated LCS gamma-ray beam was able to excite the $J^{\pi} = 1^{-}$ state at 5.512 MeV of ^{208}Pb. To define the LCS gamma-ray beam diameter and energy on the sample, we used a lead collimator with a 1 mm diameter hole. Therefore, the diameter of the LCS gamma-ray beam at the sample was approximately 1 mm. Before the collimator, the flux of the LCS gamma-ray beam was estimated to be 1.15×10^{8} photons/s with a 100% energy bandwidth at the FWHM. After the collimator, the LCS gamma-ray flux was calculated using the EGS5 Monte Carlo simulation code [172] to be 5.5 photons/s/eV at maximum energy 5.54 MeV with 1.1% energy bandwidth at the FWHM.

5.2.3 Detectors

The measuring setup of the present experiment included four types of detectors: a plastic scintillator (Pl), an HPGe, a $LaBr_3$(Ce) detector, and a flat panel detector (FPD). The Pl scintillator with a 5 mm thickness, manufactured by OHYO KOKEN KOGYO Co., Ltd. In Kumagawa, Fussa City, Tokyo, Japan, was used to measure the flux of the incident LCS gamma-ray beam. To measure the scattered gamma rays from the witness material, two HPGe detectors with efficiencies of 120%, manufactured by AMETEK ORTEC, Tennessee, USA, and 130%, manufactured by Mirion Technologies (CANBERRA), Connecticut, USA, were used. The efficiencies of the HPGe detectors were relative to a 3" 3" NaI(Tl) scintillator. The energy calibration of the HPGe detectors was conducted using energy lines coming from the natural background gamma rays of ^{208}Tl (2614.5 keV) and ^{40}K (1460.8 keV). The energy calibration was extrapolated to the energy line of 5.512 MeV with a 2–4 keV deviation, which was validated by both the energy peak of 5.512 MeV and its single escape at 5.001 MeV. The 3.5” × 4” $LaBr_3$(Ce) scintillation detector, manufactured by SAINT-GOBAIN, Courbevoie, France, was employed to measure the flux of the transmitted

gamma rays from the witness material, which was used to evaluate the atomic attenuation in the CT sample. The position of the gamma-ray beam and CT sample was verified using the FPD detector. The spectra of all detectors were recorded using an 8-channel digital signal processor (APU8008) manufactured by Techno-AP Co., Ltd. Mawatari, Hitachinaka-shi, Ibaraki, Japan, and a conventional multichannel analyzer (MCA8000D), manufactured by Amptek, Deangelo Dr, Bedford, MA 01730, USA. The dead time of each of the detectors was less than 1% of the total real time.

5.2.4 Experimental set-up

Figure 5.2 shows the experimental setup of the NRF − CT imaging in 2D. The collimated LCS gamma-ray beam was injected into the CT sample after passing through the Pl scintillator detector. The Pl was installed 145.5 cm downstream of the collimator. The CT sample, which was positioned on the controllable traveling stage, was 198.5 cm downstream of the collimator. The witness target was manufactured from the isotope of interest (^{208}Pb) with a purity greater than 97.8 % with a longitudinal length and diameter of 12 mm and 6 mm, respectively. The transmitted gamma-ray photons beyond the CT sample were then projected onto the witness target, which was 43 mm downstream from the CT sample on the LCS gamma-ray beam path. The two HPGe detectors were positioned at an angle of 120° to the LCS beam axis. The $LaBr_3$(Ce) detector was placed 113 cm downstream from the CT sample to receive the photons transmitted by the witness target. A bismuth attenuator (Bi absorber) with a thickness of 10 cm was placed in front of the $LaBr_3$(Ce) detector crystal surface to prevent pile-up events caused by the high flux of the LCS gamma rays. We used bismuth as an absorber because of its high density. In addition, in the NRF − CT imaging technique, we measure the scattered NRF gamma rays from a witness material made from the isotope of interest, such as the lead isotope ^{208}Pb in our experiments. If we used lead material as an

absorber, the NRF gamma rays would be contaminated by the NRF gamma rays scattered from the absorber material. Therefore, it is preferable to avoid using the isotope of interest material as an absorber. Other high-density materials, such as tungsten, can be used as absorbers as well. However, bismuth is less expensive than tungsten. The FPD was likewise placed in front of the $LaBr_3(Ce)$ detector at 60 cm from the witness target. Figure 5.3 shows a photo of the experimental setup during the experiment at the beamline BL1U in the UVSOR facility.

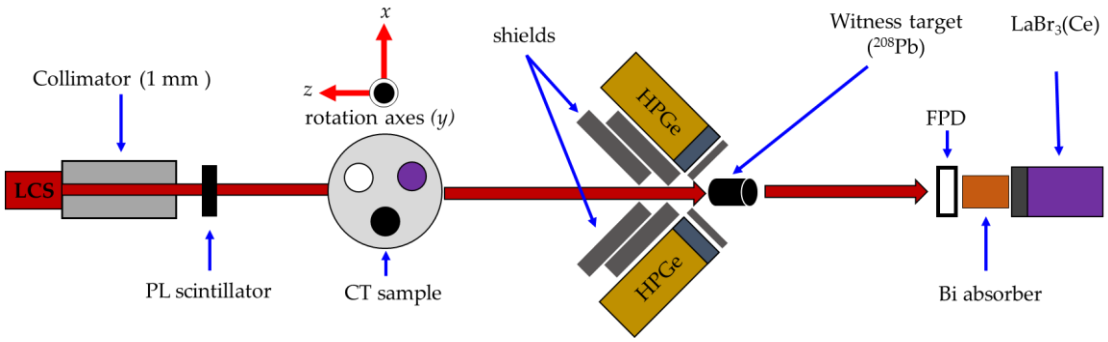

Figure 5. 2. Schematic of the experimental setup of the 2D NRF – CT imaging technique at the beam line BL1U in the UVSOR – III facility

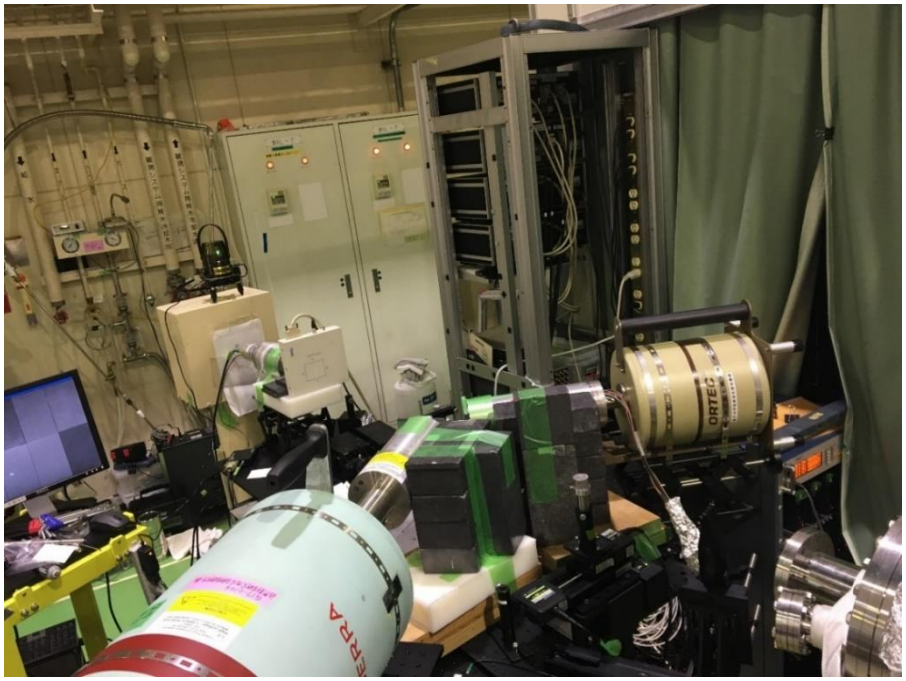

Figure 5. 3. Photo of the experimental setup to measure the 2D NRF – CT at the beam line BL1U in UVSOR – III

5.3 Results and discussion of the 2D NRF − CT isotope imaging

In the following steps, we will use the gamma-ray transmission factor measurements to measure an isotope selective CT image of the ^{208}Pb distribution buried within an aluminum holder, considering both atomic effect and nuclear resonance attenuation. Increasing the number of the scanned positions by employing an LCS gamma-ray beam (1 mm) with a scanning step of 2 mm in the x-direction, resulted in a clear image with higher spatial resolution compared to prior investigations conducted by H. Zen et al. [127]. The difference between the NRF yields obtained with and without the CT sample is used to determine the depth of the notch in the spectrum of transmitted photons through the sample caused by the isotope of interest (figure 5.4). However, these NRF yields are affected by atomic attenuation as well as nuclear resonant attenuation in the investigated sample [177]. The attenuation produced by atomic processes partly influences the transmission of incident gamma-ray photons through the measured sample.

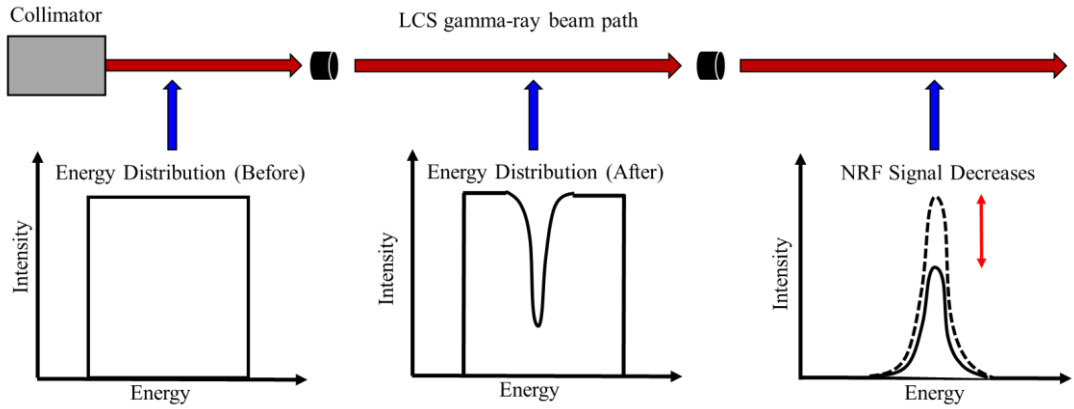

Figure 5. 4. Energy distribution of the LCS gamma-ray beam along the beam path

The energy spectra obtained with the $LaBr_3$(Ce) detector and the PL scintillator, respectively, are shown in figures 5.5 and 5.6. The colored area in each spectrum stands for the region of interest (ROI). The $LaBr_3$(Ce) detector's energy resolution was sufficient to discriminate between the LCS gamma-ray peak and its single escape. As a result, the ROI was chosen to cover the energy

range of 5260 to 5885 keV in order to include the whole energy peak. In contrast, the PL scintillator exhibited limited energy resolution and no visible peak in the spectrum. Therefore, the ROI was chosen to cover channels 650 to 7100 to get the relative flux of the incident LCS gamma-ray photons. For each measurement circumstance, the ROI's integrated count was divided by the measurement system's live time.

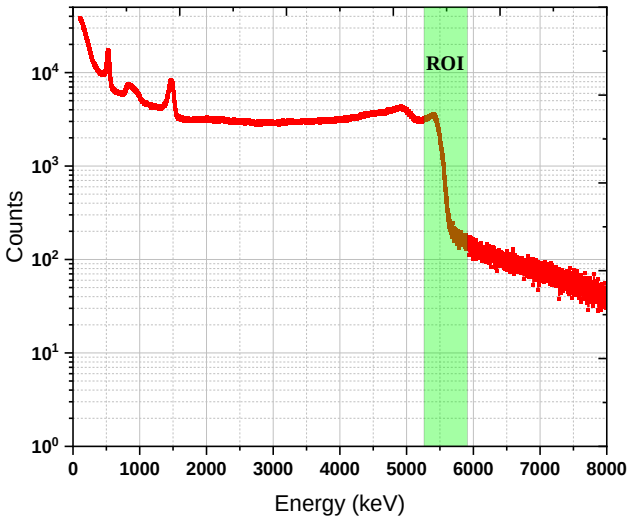

Figure 5. 5. Typical spectra recorded by the $LaBr_3$(Ce) scintillation detector

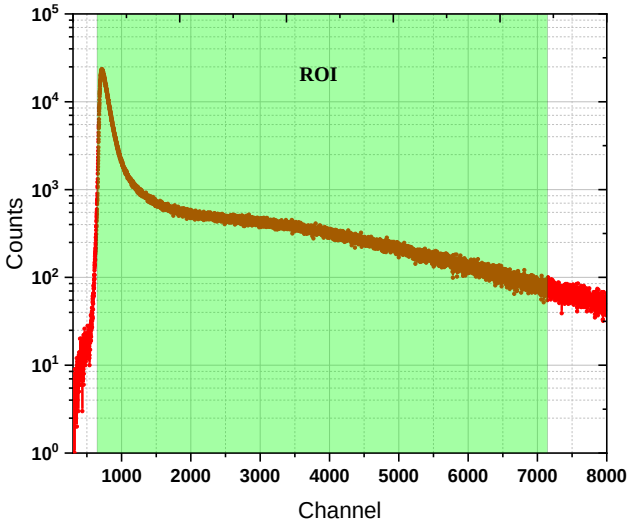

Figure 5. 6. Typical spectra recorded by the PL scintillator

The transmission factor of the off-resonance gamma ray is a function of the CT sample's rotation angle (θ) around the y-axis and its horizontal location (x) along the x-axis. Therefore, it can be calculated using the formula below for each scanning position (x, θ) as:

$$\varepsilon_{\text{off}} = e^{\left[-\left(\frac{\mu}{\rho}\right)_{\text{ave}} \times \rho_{\text{ave}} \times L\right]} \qquad \text{Eq. (5.1)}$$

where ε_{off} is the transmission factor of the off-resonance gamma rays, $(\mu/\rho)_{\text{ave}}$ is the mass attenuation coefficient on average, ρ_{ave} is the average density, and L is the length of the path through the sample [127, 178]. The transmitted gamma rays were attenuated by the bismuth attenuator, but this absorption was neutralized throughout the treatment. The normalized count rate of the transmission detector was calculated by dividing the count rate of the $LaBr_3$(Ce) detector by the total integrated count rate of the PL scintillator. As a result, the ε_{off} at each position is as follows:

$$\varepsilon_{\text{off}} = \frac{C_{\text{off}}\,(\text{sample on})}{C_{\text{off}}\,(\text{sample off})} \qquad \text{Eq. (5.2)}$$

where, $C_{\text{off}}\,(\text{sample on})$ is the normalized count rate of the transmission detector in the presence of the sample, and $C_{\text{off}}\,(\text{sample off})$ is the normalized count rate of the transmission detector in the absence of the sample. Because the ROI was 4– 5 orders of magnitude broader than the NRF resonance, the effect of resonance attenuation on the yield recorded by the $LaBr_3$(Ce) detector was insignificant and can be neglected. The acquisition time of the measurements for each position was insufficient to obtain the requisite high statistics of the recorded spectra by the HPGe detectors. Therefore, each spectrum was compressed with a numerical re-binning process along the energy axis from 1 keV per channel to 2 keV per channel. Furthermore, to maximize statistics, each two-spectrum recorded by the HPGe detectors in one

position (x, θ) was summed up into a single spectrum with a 2 keV energy interval. Figure 5.7 shows a spectrum generated by merging two energy spectra recorded with the two HPGe detectors. There were several energy levels appear in the spectrum, including the NRF level of the ^{208}Pb at the energy of 5512 keV, in addition to two clear energy levels at 1460 keV and 2614 keV that originated from the naturally unstable isotopes of ^{40}K and ^{208}Tl, respectively.

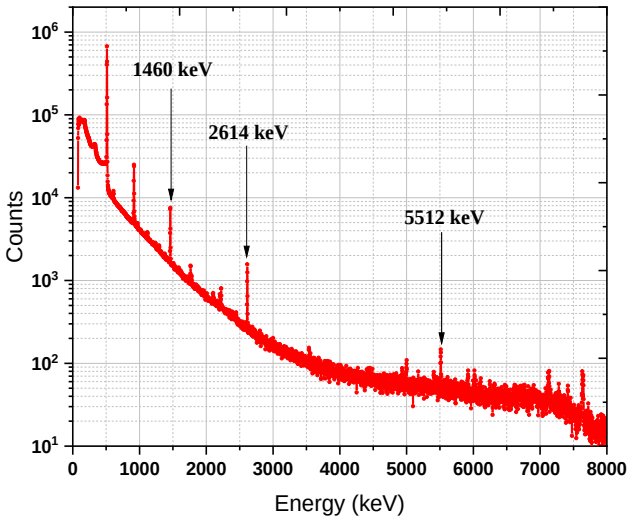

Figure 5. 7. Combination of two spectra recorded by the HPGe detectors with 2 keV energy intervals

Figure 5.8 shows a zoomed-in plot of the region around the energy level of the NRF of ^{208}Pb at 5512 keV. The NRF peak's FWHM values were 7.6, 7.8, and 8.8 keV for the 120% HPGe detector, 130% HPGe detector, and merged spectra, respectively. A least-squares Gaussian function was used to fit the NRF peak of ^{208}Pb at 5512 keV. The area under the peak was used to determine the NRF yield. The ROOT C++ scripts [179] were used for all data analysis and calculations in this investigation.

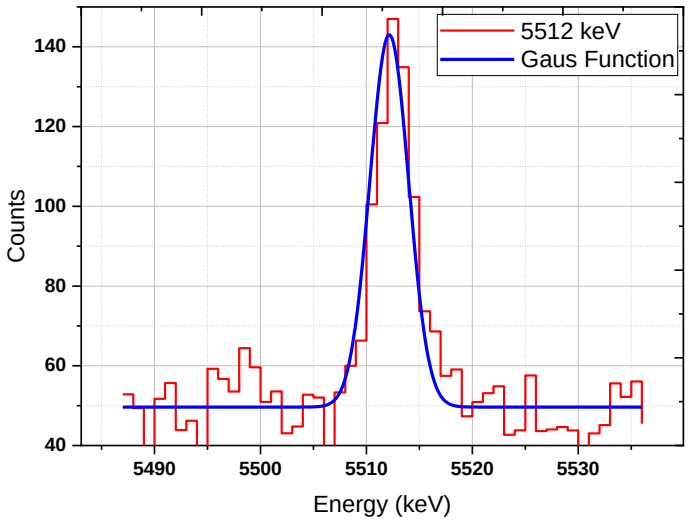

Figure 5. 8. The NRF peak corresponding to the 5512 keV level of ^{208}Pb

The normalized NRF count rate can be calculated by dividing the NRF yield by the measurement live time and then normalized by the total count of the PL scintillator. The transmission factor at the resonance energy is a function of the rotation angle (θ) and the horizontal location (x). Therefore, it can be calculated using the formula below for each scanning position (x, θ) during the measurements:

$$\varepsilon_{\text{on}} = e^{\left[-\left(\left(\frac{\mu}{\rho}\right)_{\text{ave}} \times \rho_{\text{ave}} \times L + \sigma_{\text{NRF}} \times N_{\text{t}}\right)\right]} \qquad \text{Eq. (5.3)}$$

where ε_{on} is the transmission factor at the resonance energy, σ_{NRF} is the isotope of interest's NRF cross-section, and N_{t} is the nuclide of the sample's areal density in the direction of the LCS gamma-ray beam. The ε_{on} at each position can also be stated as follows:

$$\varepsilon_{on} = \frac{C_{\text{on}}\ (\text{sample on})}{C_{\text{on}}\ (\text{sample off})} \qquad \text{Eq. (5.4)}$$

where the normalized NRF count rate obtained in the presence and absence of the sample, respectively, is denoted by C_{on} (sample on) and C_{on} (sample off).

We assume that the atomic effect causes the same attenuation of resonant photons as it does for beam photons. We converted the transmission factor to a logarithmic expression and calculated nuclear resonance attenuation by subtracting atomic attenuation using the following equation to obtain the $\mathrm{NRF}-\mathrm{CT}$ image of the isotope of interest:

$$-ln(\mathcal{E}_{\mathrm{NRF}}) = -[ln\,(\mathcal{E}_{\mathrm{on}}) - ln\,(\mathcal{E}_{\mathrm{off}})] \qquad \text{Eq. (5.5)}$$

Because the number of isotope or scattering sources in the CT sample is proportional to the sign-inverted natural logarithm of the attenuation factor $[-ln(\mathcal{E})]$, the images in $2\mathrm{D}-\mathrm{CT}$ are reconstructed using the sign-inverted natural logarithm of the attenuations $[-ln(\mathcal{E}_{\mathrm{NRF}}), -ln(\mathcal{E}_{\mathrm{on}})$, and $-ln(\mathcal{E}_{\mathrm{off}})]$.

Reconstruction algorithm

Two kinds of CT reconstruction algorithms could be used for the $\mathrm{NRF}-\mathrm{CT}$ images: an analytical algorithm and an iterative algorithm. The analytical algorithm has the advantage of being fast, but when there are few observation angles, significant disturbances, or "artifacts," degrade the quality of the reconstructed images. Artifacts are commonly generated during the sample scanning process because of the limited number of observation angles. Due to the limited number of measured projections in the studies of this dissertation, one of the iterative algorithms, called the algebraic reconstruction technique (ART) [180 – 182], was employed for the image's reconstruction. The ART algorithm is defined as a sequential approximation method for image reconstruction from a series of projections (sinogram). Since attenuation in $\mathrm{NRF}-\mathrm{CT}$ is always positive in principle, it is preferable for the CT reconstruction algorithms used for image reconstruction to be free of non-negative restrictions, such as the ART algorithm. To implement the ART algorithm, the data points within the sinogram were processed in a series of

steps as follows: First, we created a primary image in the form of a 2D matrix with zero value in each cell. The primary image was given the name $image_0\ (x, y)$. The number of cells in the matrix was figured out based on the projection numbers obtained throughout the sample scanning. In our study, each primary matrix was in the dimensions of 14×14. If the symbol character k refers to the primary image's iteration number, then the processed image with k iterations for the primary image is first rotated by the observation angle as:

$$image_k(x, y) = A_{\theta_j,k}\left[x\ cos\ \theta_j\ - y\ sin\ \theta_j, x\ sin\ \theta_j + y\ cos\ \theta_j\right] \qquad \text{Eq. (5.6)}$$

If $A_{\theta j}(x, y_i)$ and $p(x, \theta_j)$ are the projections corresponding to the x-axis, and observation angle θ_i, respectively, and where N is the number of data points in a single projection date, the difference matrix $D_{\theta j,k}(x, y)$ can be calculated as:

$$D_{\theta_j,k}(x, y) = \frac{1}{N}\left[p(x, \theta_j) - \sum_{i=1}^{N} A_{\theta_j,k}(x, y_i)\right] \qquad \text{Eq. (5.7)}$$

If the matrix $D_\theta(x, y)$ has no y dependence, the difference matrix in equation (5.6) is rotated back as:

$$D_{\theta_j,k}(x, y) = D'_{\theta_j,k}\left(x\ cos\ \theta_j + y\ sin\ \theta_j - x\ sin\ \theta_j + y\ cos\ \theta_j\right) \qquad \text{Eq. (5.8)}$$

At the current step, the image starts to be constructed. The reconstructed image for the next iteration $(k + 1)$ can be calculated by adding the summation of the difference matrix as the following formula:

$$image_{(k+1)}(x, y) = image_k(x, y) + \frac{r}{n}\sum_{j=1}^{M} D'_{\theta_j,k}(x, y) \qquad \text{Eq. (5.9)}$$

where r refers to the relaxation parameter used to control the strength of the feedback, and n is the total number of observation angles. The value of r

should be smaller than one. Therefore, it was set as 0.7 in the CT reconstruction of the NRF − CT images for the studies in this dissertation. The convergence of the reconstruction is evaluated by the root-mean-square-difference ($RMSD$) between reconstructed images of the iteration k and the iteration $(k+1)$ is given by the following formula:

$$RMSD = \sqrt{\left[\frac{1}{N^2}\sum_{i=1}^{N}\sum_{j=1}^{N}\left[image_{(k+1)}(x_i, y_j) - image_k(x_i, y_j)\right]\right]} \qquad \text{Eq. (5.10)}$$

Subsequently, the iteration process for the image will continue until the value $RMSD$ gets smaller than the user-specified value. At that point, the iteration process will be stopped and the final reconstructed image $image_{(k+1)}(x, y)$ can be obtained. The developed ART algorithm requires matrix rotation using the previous equations. This matrix rotation is astonishingly easy and may be applied to any size of the reconstructed image or projection data. However, when the quantity of data points is minimal, the matrix rotation's accuracy suffers. To address this issue, we included two additional steps before and after reconstruction. These two steps are the preprocessing and the postprocessing stages [127]. During the preprocessing stage, we split the attenuation value of each projection point into a minor grid of a certain number of points to increase the points within the matrix. As a result, the matrix rotation's precision will be enhanced. In our case, each projection data point was divided into 4 points with the same value as the original grid point before the division. Consequently, the spatial frequency of the data fed into the ART reconstruction procedure was artificially boosted fourfold. Once the image reconstruction is complete, we restore it to the initial resolution by implementing the postprocessing stage, which combines all 4 × 4 points in the reconstructed image. Therefore, the resulting reconstructed image will have the same grid size as the original projection data. Figure 5.9 shows a

schematic for both the preprocessing and postprocessing stages during the CT reconstruction using the ART reconstruction algorithm. Our research group at Kyoto University developed a framework in LabVIEW software (National Instruments, Austin, Texas, USA) to reconstruct CT images based on the ART algorithm.

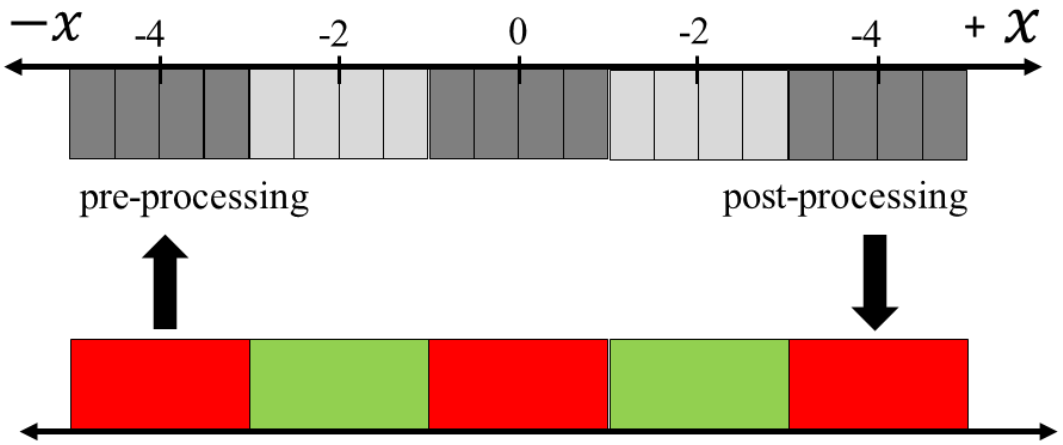

Figure 5. 9. A flowchart for both preprocessing and postprocessing steps of a CT reconstruction using the ART algorithm

Three reconstructed images (14×14) with a pixel size of 2 mm were created. The geometry of the CT sample utilized in this investigation is shown in figure 5.10 (a). The reconstructed gamma − CT image due to the off-resonance attenuation measured by the $LaBr_3$(Ce) detector is shown in figure 5.10 (b). These images clearly display two regions of strong attenuation generated by the atomic process, which correspond to the locations of the enriched lead isotope rods (^{208}Pb and ^{206}Pb). Because the intensities at the ^{208}Pb and ^{206}Pb rod's locations within the CT sample measured via atomic attenuation were virtually equal, distinguishing between these two isotopes was nearly impossible. Figure 5.10 (c) shows the reconstructed image of the on-resonance gamma-ray attenuation measured from the calculation of the transmission factor $ln(\mathcal{E}_{on})$. While the ^{208}Pb rod was clearly visible, the ^{206}Pb rod, while visible, was fainter. The absolute magnitude of the on-resonant attenuation

($-ln(\mathcal{E}_{on}) = 0.23$) at the ^{208}Pb rod position was approximately 3 times as high as that of the off-resonant attenuation ($-ln(\mathcal{E}_{off}) = 0.08$). In contrast, the on-resonant attenuation at the ^{206}Pb rod position was nearly equal to that of the off-resonant attenuation, implying that the ^{206}Pb intensity seen in figure 5.10 (c) might be attributable to atomic attenuation. Figure 5.10 (d) shows the reconstructed CT image of the NRF attenuation distribution (pure NRF) caused only by the ^{208}Pb isotope. While the ^{206}Pb rod is just slightly visible in figure 5.10 (c), it totally disappeared here. On the other hand, the white area refers to the location of the ^{208}Pb rod.

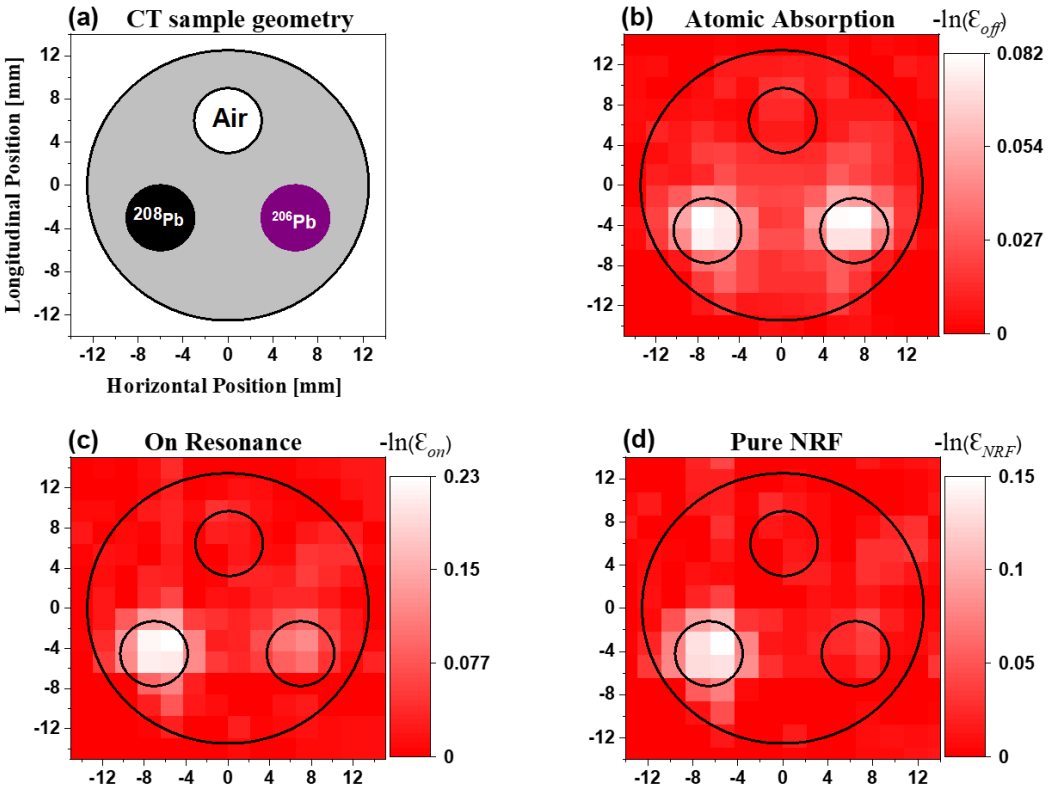

Figure 5. 10. Geometry of the CT sample under investigation. Reconstructed CT images of (b) atomic absorption, (c) on-resonance, and (d) pure NRF

From the obtained images, we conclude that the NRF − CT imaging technique can clearly differentiate between the two enriched lead isotopes (^{208}Pb and ^{206}Pb) hidden inside the same volume and that isotope-selective CT

imaging is achievable. Because a 2D NRF − CT image of a sample with a diameter (height) of 25 mm (20 mm) with a resolution of 2 mm/pixel took about 60 hours to be created, a 3D NRF − CT image of the same sample with equal pixel resolution should take roughly ten times as long (600 hours). For the NRF − CT imaging technique to be used in industrial applications, at least 3 orders of intense gamma-ray flux and an immense number of detectors must be provided. Furthermore, the current sample's NRF level ($J^{\pi} = 1^{-}$ state at 5.512 MeV) in ^{208}Pb has a large NRF cross-section, $\Gamma^{0} = 28.3$ [107], whereas a standard NRF level, i.e., $J^{\pi} = \left(\frac{7}{2}\right)^{+}$ state at 2.212 MeV in ^{27}Al ($\Gamma^{0} = 17.1$ meV) has a 3 order smaller NRF cross-section [183]. As previously stated, the ELI − NP in Romania is now constructing a new facility for LCS gamma rays [166]. The LCS gamma-ray beam's spectral density flux is projected to be in the 5×10^{3} photons/s/eV zones, allowing for practical usage of the NRF − CT imaging technique.

6 ISOTOPE IMAGING IN THREE DIMENSIONS

6.1 Overview

In principle, if a 3D visualization of a particular isotope hidden inside an assay volume is available, the hidden isotopes are fully perceived. In the preceding study of this dissertation in Chapter 5, we performed the NRF − CT proof-of-experiment for isotope selective imaging using an LCS gamma-ray beam accessible at the UVSOR − III facility's beamline BL1U [173]. We measured a 2D NRF − CT image of a ^{208}Pb rod implanted in a specimen holder manufactured from aluminum based on the NRF transmission method. The reconstructed image had a resolution of 2 mm/pixel and an acquisition time of 60 hours. Obviously, the NRF − CT imaging technique is time-consuming. Therefore, we should clarify the limitations of the NRF − CT imaging technique for isotopes using the LCS gamma-ray beams to perform the imaging in 3D under the current experimental conditions of the UVSOR − III facility and improve the measurement and analysis procedures accordingly. In the present study of this dissertation, we demonstrate the NRF − CT imaging technique in 3D with three layers of 2D NRF − CT images within the time constraints of the machine (60 hours). To accomplish this, some upgrades in the previous system's experimental setup were made, including increasing the flux intensity of the LCS gamma rays and lowering the number of scanning steps for the 2D images in each layer of scanning.

6.2 The experimental procedures for 3D NRF − CT imaging

6.2.1 The upgrading in the LCS gamma ray's source

The experiment of isotope selective CT imaging in 3D was also conducted at the beamline BL1U in the UVSOR − III facility. Similarly, the LCS gamma rays were generated by a head-on collision between the randomly polarized intensive laser beam generated by the Tm-fiber laser source (50 W,

CW) and the high-energy electrons in the UVSOR − III storage ring (electrons energy of 746 ± 1 MeV and beam current of 300 mA) in the top-up mode [148]. In the present condition of the experimental setup, the maximum energy of the generated gamma rays was 5.54 MeV with a 100% energy bandwidth at the FWHM and a total flux of 1.15×10^8 photon/s before collimation. This maximum energy, as mentioned, is capable of exciting the state $J^\pi = 1^-$ at 5.512 MeV in ^{208}Pb [107]. A lead collimator (20 cm × 10 cm × 10 cm) with a hole diameter of 2 mm was positioned in the LCS gamma-ray beam path to define the LCS beam diameter and the energy spectrum in the investigated sample. The gamma-ray flux density flowing through the collimator was determined to be 10 photons/s/eV at the resonance energy of 5512 keV, as calculated using the EGS5 Monte Carlo simulation code [172]. The duplication of the gamma-ray flux density in the current setup was due to the utilization of a collimator with a hole diameter twice that of the earlier collimator [173]. Table 6.1 summarizes the upgrades to the LCS gamma-ray source during the current experiment.

Table 6. 1. The upgrading in the LCS gamma rays' source for NRF − CT imaging technique from 2D to 3D

	LCS beam parameters	2D NRF − CT	3D NRF − CT
Inputs	LCS beam diameter	1 mm	2 mm
	e^- energy	746 ± 1 MeV	746 ± 1 MeV
	e^- current	300 mA	300 mA
	Laser power	36 W (CW)	36 W (CW)
	Laser wavelength	1.896 μm	1.896 μm
	Polarization	Random	Random
Outputs	LCS intensity	5.5 photons/s/eV	10 photons/s/eV

6.2.2 CT sample and scanning plan in 3D

The sample container was the same cylindrical aluminum holder described in Section 4.2 of Chapter 4. The sample holder's apertures were filled with a set of cylindrical rods measuring 6 mm in both diameter and height. One of the enriched lead isotope rods (^{208}Pb) was inserted in the bottom hollow of hole 1, followed by a Fe rod, and the third hollow was left unfilled. One of the enriched lead isotope rods (^{206}Pb) was placed at the bottom of hole 2, followed by a hollow Al rod and a ^{208}Pb rod. The bottom of hole 3 was filled with a ^{208}Pb rod, followed by a Fe rod and a ^{206}Pb rod at the top. Figure 6.1 shows the arrangement of the rods within the sample holder.

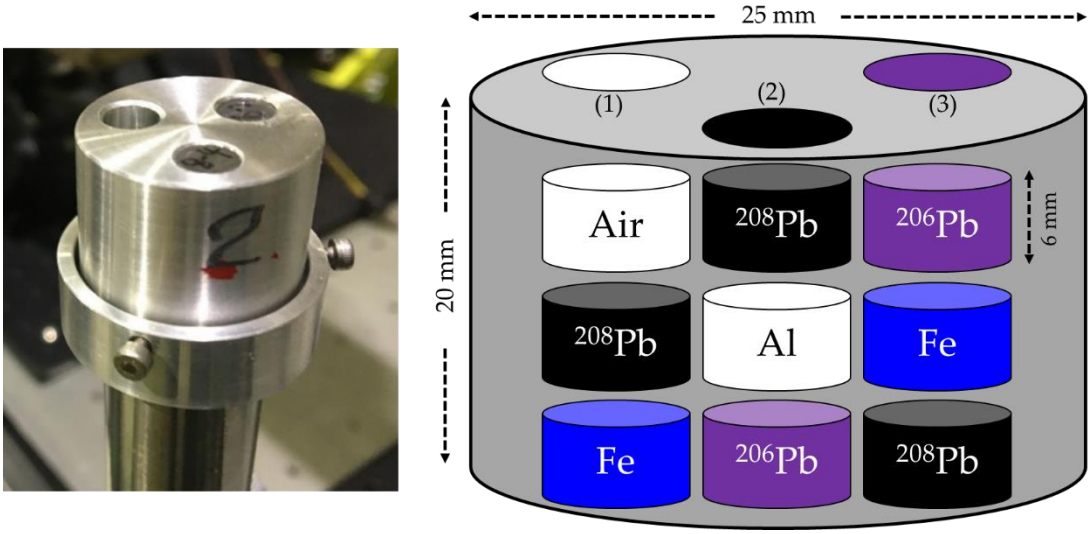

Figure 6. 1. The CT sample used in 3D NRF − CT imaging consists of a set of dissimilar materials (^{206}Pb, ^{208}Pb, Fe, Al, and Air) implied in a thick aluminum holder

The sample was mounted on a three-axis controllable traveling stage that could scan in three directions: vertical (z), rotating (θ), and horizontal (x). Figure 6.2 shows the CT sample's scanning directions. We choose the smallest number of scanning locations and step sizes in each scanning direction that will allow us to obtain a 3D NRF − CT image with an adequate resolution by utilizing the available LCS gamma rays while considering the CT sample geometry and the machine time constraints. Since the gamma-ray beam

diameter (2 mm) was half the size of the reconstructed image's pixels, it was sufficiently smaller than the item being investigated (6 mm). Because there were 3 rows of rods in the z-direction, 3 layers were chosen at the vertical distances of $z = 3$, 11, and 17 mm measured from the sample holder bottom to reconstruct the 2D NRD − CT image for each horizontal row of rods. The sample was rotated around the rotational axis (θ) with an angle step of 30° from 0° to 150°. The scanning was also conducted in the x-direction, with a step size of 4 mm in the range of −12 to +12 mm. Therefore, we recorded 126 data points of measurements (7 steps along x-direction, 6 angles along θ-direction, and 3 layers along z-direction). In addition, we recorded one data point for each horizontal scan in the x-direction in the absence of the investigated sample from the LCS beam path. As a result, a total of 144 positions were scanned with an average measurement time of 20 minutes for each position, and a total measurement duration of 48 hours. Table 6.2 summarizes the scanning procedures for the NRF − CT isotope imaging in 3D.

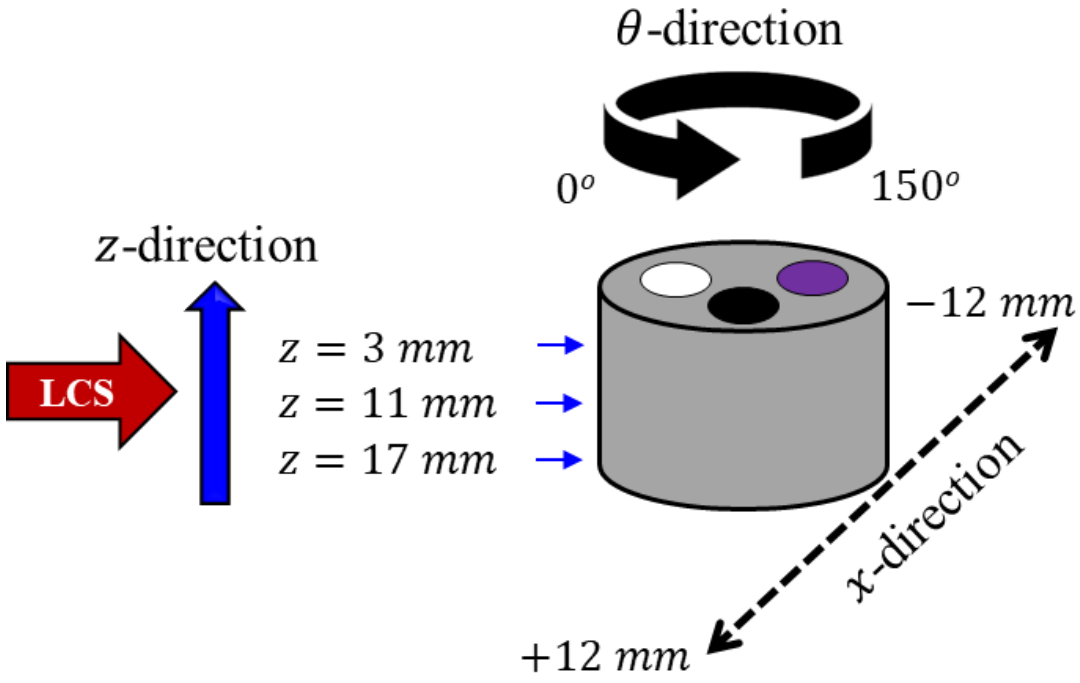

Figure 6. 2. Scanning geometry of the NRF − CT imaging in 3D

Table 6.2. The scanning procedures for NRF − CT imaging in three dimensions

Direction	Step size	Range	No. of points
θ	30°	0° ~150°	6
x	4 mm	$-12 \sim +12$ mm	7
z	@ $z = 3, 11, 17$ mm		3 Layers
Acquiring Time for one position			20 minutes
Overall measurement time			48 hours

6.2.3 Experimental set-up

The experimental setup for the isotope selective CT imaging in 3D was comparable to the preceding setup [173] except for the inclusion of one dimension of scanning in the z-direction. Figure 6.3 shows a schematic diagram of the experimental setup. One recommendation for reducing the acquisition time of the measurements was the ability to control the scanning process, data analysis, and storage of the recorded spectra automatically. Therefore, we developed an automated scanning system that was programmed with LabVIEW software. The scanning system includes: (i) a controller for the traveling stage in 3D; horizontal (x), vertical (z), and rotational (θ), (ii) a live data processing system, and (iii) storing for the recorded spectrum. The lead collimator was positioned in the path of the LCS gamma-ray beam. The flux of the incident beam was measured using the Pl scintillator detector installed 1.6 meters downstream from the collimator. The CT sample was positioned 2.14 meters downstream from the collimator. The transmitted gamma rays were injected into the sample after passing through the Pl scintillator. The LCS gamma-ray beam then irradiated a witness material (^{208}Pb) in diameter and height of 6 mm located 0.65 meters far from the CT sample. Two HPGe detectors (100% and 130%) were placed in two positions at an angle of 120° to

the gamma-ray beam axis and at a vertical distance of 8 cm from the witness material. Like in the earlier study [173], the HPGe detectors were utilized to measure the scattered NRF gamma rays from the witness material. To protect the HPGe detectors from the photon buildup and reduce the dead time, heavy lead shields were installed around the gamma-ray beam axis. In addition, lead absorber plates with a thickness of 6 mm were inserted between each HPGe detector and the witness material. We measured the flux of gamma rays transmitted from the witness material using the $LaBr_3(Ce)$ scintillation detector placed 0.4 meters downstream from the witness material to evaluate the atomic attenuation in the investigated sample. To prevent signal pile-up on the $LaBr_3(Ce)$ detector, a bismuth absorber with a thickness of 10 cm was placed in front of the detector. The gamma rays transmitted from the witness target were attenuated by the Bi absorber, but this attenuation was negated during image reconstruction. The signals from each detector were independently recorded by a multichannel analyzer, USB-MCA4 (APG7400).

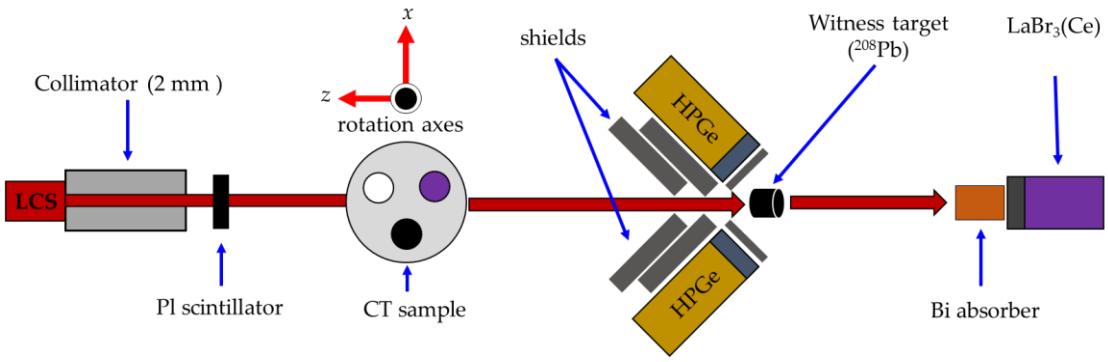

Figure 6. 3. Schematic of the experimental setup of the 3D NRF – CT imaging technique at the beam line BL1U in the UVSOR – III facility

6.3 Results and discussion of the 3D NRF – CT imaging

The numerical method used to measure the 2D images for each layer measured in the z-direction was detailed in Chapter 5 of this dissertation. Therefore, we will discuss it in less detail in this section, but in accordance with the current measurement conditions. The 2D NRF – CT images of the ^{208}Pb rods

for each layer in the z-direction were obtained by measuring the gamma-ray transmission factors, which included the effects of atomic absorption and nuclear resonance attenuation [173]. Figure 6.4 shows a typical LCS spectrum recorded by the Pl scintillator. Because the Pl scintillator had no energy resolution within the 5 MeV region, the ROI was chosen in a wide channel range from 50 to 7000, to measure the relative flux of the incident gamma ray beam.

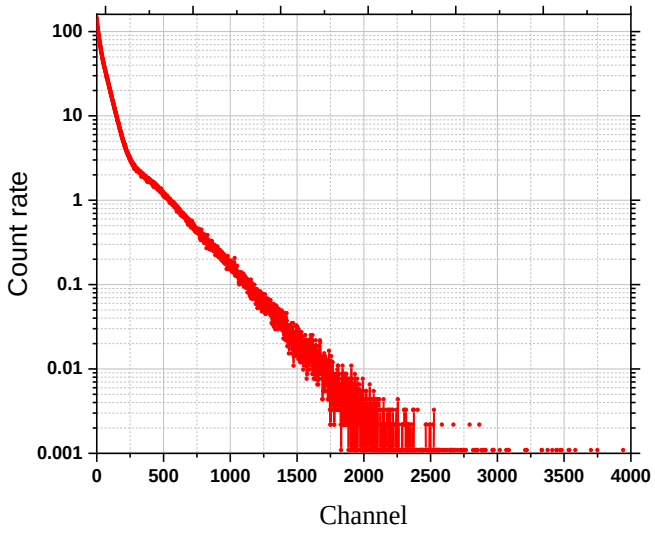

Figure 6. 4. Part of the spectrum recorded by the PL scintillator (0: 4000 channel)

Figure 6.5 shows a typical energy spectrum recorded by the $LaBr_3$(Ce) scintillation detector. The ROI, shown by the colored area, covered the energy range from 5.36 MeV to 5.885 MeV to consider the counts under the full energy peak. By integrating the counts in the ROI s and dividing them by the acquisition live time, we determined the count rates of the PL scintillator and the $LaBr_3$(Ce) detector for each location of scanning (x, θ). Then, we calculated the ε_{off} according to the following: The count rate of the $LaBr_3$(Ce) transmission detector was divided by the total integrated count rate of the PL scintillator within the ROI. The ε_{off} was calculated by normalizing the count rate of the transmission detector in the presence and absence of the CT sample. The influence of resonance attenuation on the yield measured by the $LaBr_3$(Ce)

detector was likewise minimal in this investigation, as the ROI was 4– 5 orders of magnitude broader than the resonance attenuation.

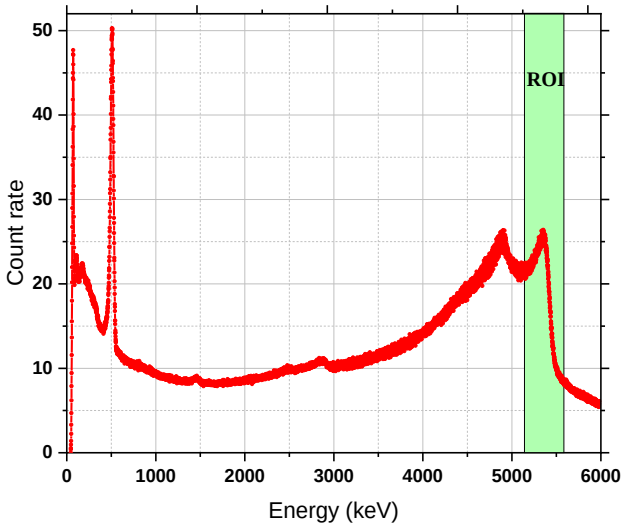

Figure 6. 5. Typical gamma-ray spectrum recorded by the $LaBr_3$(Ce) detector

The recorded spectra by the HPGe detectors were summed after the energy axis was re-binned by 2 keV per channel to enhance the statics of the NRF signal scattered from the witness material. Figure 6.6 shows a typical summed energy spectrum by those detectors in the 2 keV energy interval. There were several energy levels that clearly appeared in the summed spectra as follows: The NRF level of ^{208}Pb at 5.512 MeV, another NRF level of ^{208}Pb at 5.292 MeV, the single escape peak of the ^{208}Pb NRF level (5.512 MeV) at 5.001 MeV, the double escape peak of the ^{208}Pb NRF (5.512 MeV) at 4.490 MeV, the naturally unstable isotopes of ^{208}Tl at 2.614 MeV, and the naturally unstable isotopes of ^{40}K at 1.460 MeV. The two energy lines of 1.460 MeV and 5.512 MeV have been used to perform the energy calibration for the HPGe detectors. The NRF peak of ^{208}Pb at 5.512 MeV was fitted using the least-squares method of the Gaussian function (figure 6.7). Thus, the NRF yield was calculated using the area resulting from fitting. The normalized NRF count rate was derived by dividing the NRF yield by the acquisition live time and the Pl scintillator's count rate.

The ε_{on} at the resonance energy was then calculated for each (x, θ) by the normalized NRF count rate obtained in the presence and absence of the investigated sample. Furthermore, we followed the same calculation to estimate the ε_{NRF} which we detailed in Chapter 5 of this dissertation. Due to the limited number of scanned projections in the current study, we also used the ART algorithms for the image's reconstruction.

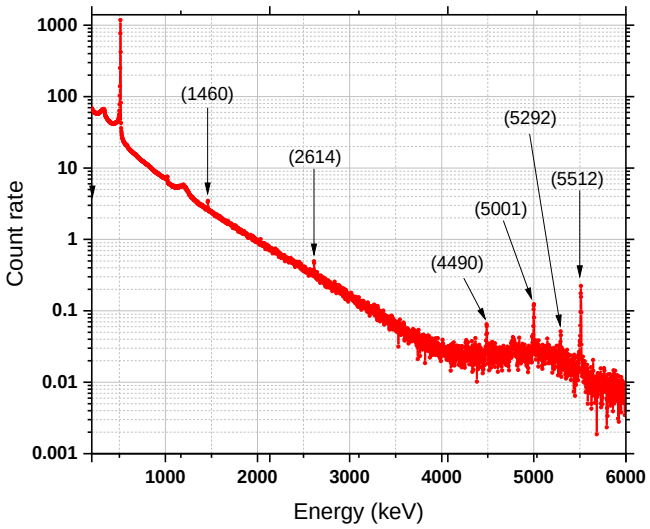

Figure 6. 6. HPGe detector spectra (summation of two spectra) in a 2 keV energy interval

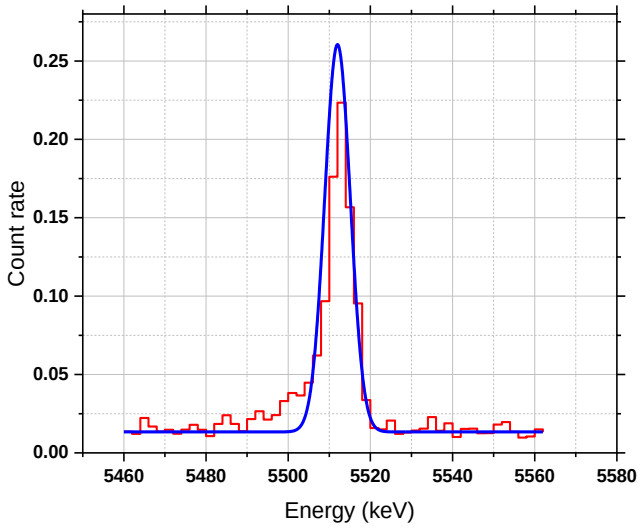

Figure 6. 7. Gaussian fitting for the ^{208}Pb NRF energy level at 5.512 MeV

Three images for gamma − CT, on-resonance attenuation, and pure NRF attenuation were reconstructed with a resolution of 4 mm/pixel for each layer of scanning in the z-direction. Figure 6.8 (a) shows a cross-sectional view of the sample taken at $z = 3$ mm. It shows the rods ^{206}Pb and ^{208}Pb were inserted into two holes of the holder, while a Fe rod was inserted into the third one. The gamma − CT images of the off-resonance attenuation detected by the $LaBr_3$(Ce) detector are shown in figure 6.8 (b). The ^{206}Pb and ^{208}Pb rods correspond to the two high-attenuation zones created by the atomic process. However, differentiating between these two isotope rods is challenging due to the almost similar atomic attenuations of both materials. The Fe rod vanished in the gamma − CT image because the atomic attenuation induced by the Fe rod was lower than that caused by the lead rods. Figure 6.8 (c) presents the distribution of on-resonance gamma-ray attenuation. Although the ^{208}Pb rod was clearly visible, the ^{206}Pb rod had a much lower intensity. Furthermore, the Fe rod had almost vanished. After atomic attenuation is eliminated, figure 6.8 (d) shows the NRF − CT image for the ^{208}Pb distribution. The ^{208}Pb rod was clearly visible, while the other rods (^{206}Pb and Fe) were almost invisible.

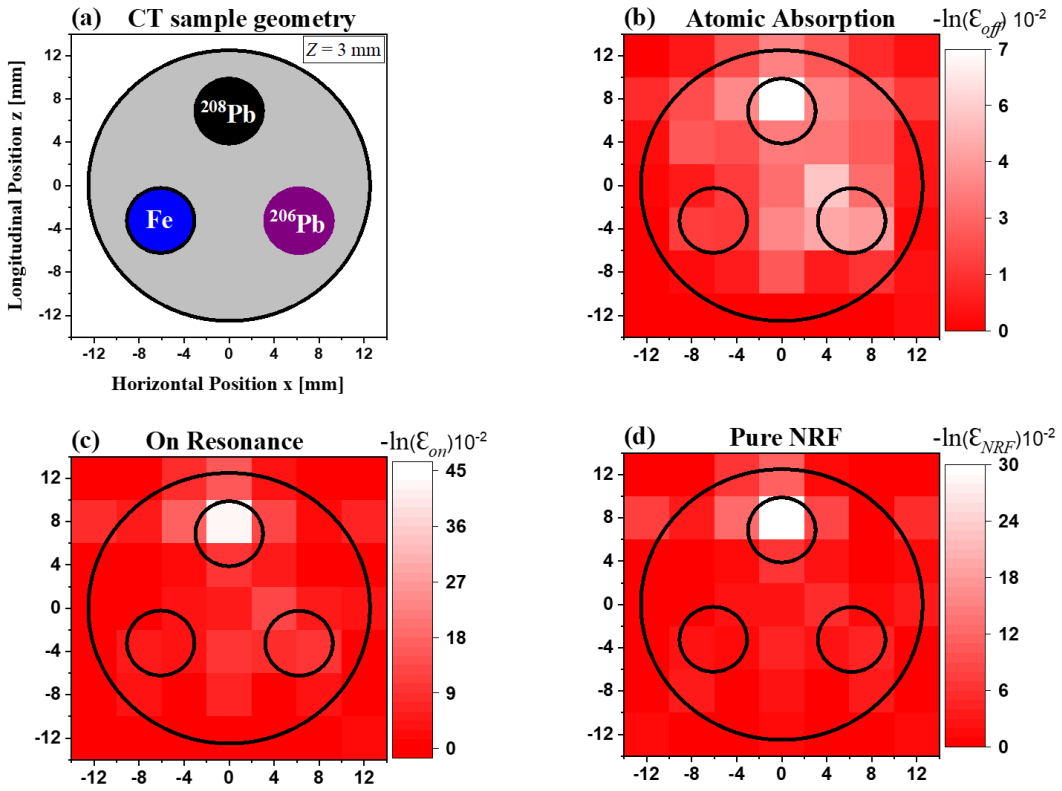

Figure 6. 8. (a) CT sample cross-sectional layer image at a vertical distance of $z = 3$ mm (b) gamma − CT image, (c) on-resonance attenuation image, and (d) NRF − CT image

The rod's configuration is shown in figure 6.9 (a) at a vertical distance of $z = 11$ mm. This row of rods contains the rods of ^{208}Pb, Fe, and Al, which are placed into the sample holder's first, second, and third holes, respectively. The gamma − CT image, which indicates the high-attenuation zone owing to the atomic process related to the ^{208}Pb rod, is shown in figure 6.9 (b). The Fe and Al rods vanished from the reconstructed image because their atomic attenuation was smaller than that of the lead rod. In the on-resonance image as shown in figure 6.9 (c) and the pure NRF image as shown in figure 6.9 (d), only the ^{208}Pb rod was visible, while the Fe and Al rods completely vanished.

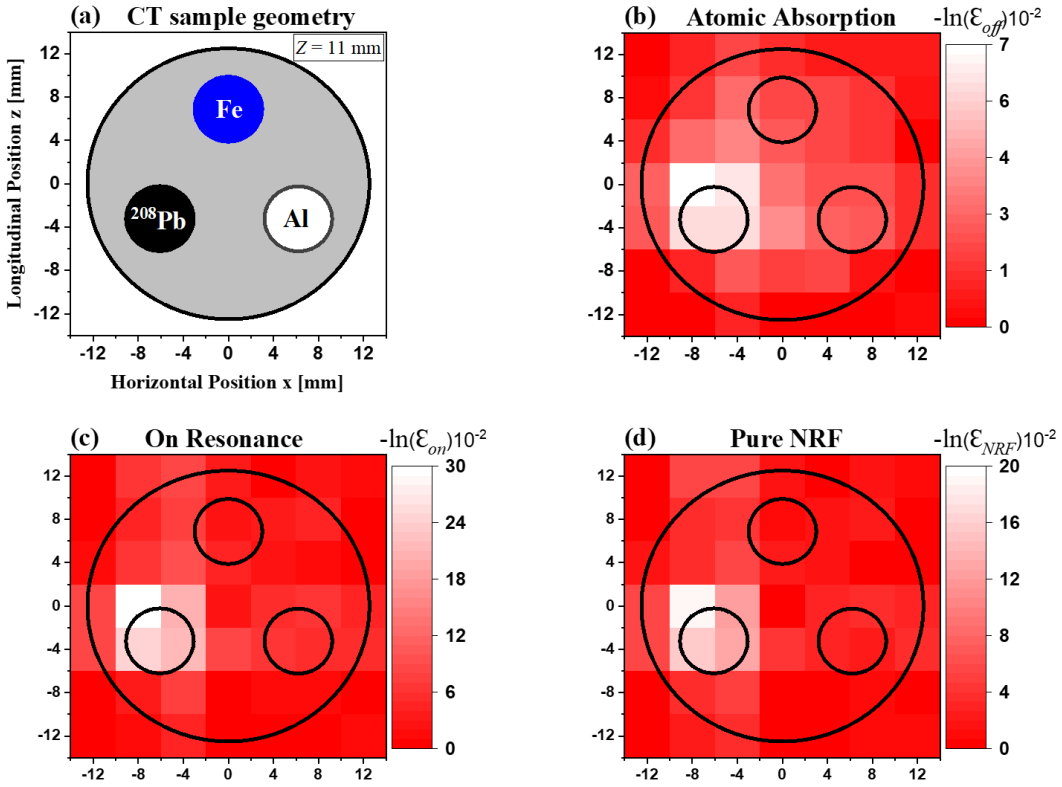

Figure 6. 9. (a) CT sample cross-sectional layer image at vertical distance of $z = 11$ mm (b) gamma − CT image, (c) on-resonance attenuation image, and (d) NRF − CT image

The rod's configuration is shown in figure 6.10 (a) at a vertical distance of $z = 17$ mm. This row of rods contains ^{208}Pb, and ^{206}Pb, which are placed into the sample holder's first and second holes, respectively. The third drilled hole was left empty. The gamma − CT image is shown in figure 6.10 (b). The ^{206}Pb and ^{208}Pb rods correspond to the two high-attenuation zones created by the atomic process, but the low intensity at the third hole refers to the empty space. The distribution of the on-resonance is seen in figure 6.10 (c), in which the ^{208}Pb rod was plainly visible, and the ^{206}Pb rod seemed blurry. Figure 6.10 (d) shows the NRF − CT image of the ^{208}Pb distribution. The ^{208}Pb was clearly apparent, whereas the ^{206}Pb rod and empty space were invisible.

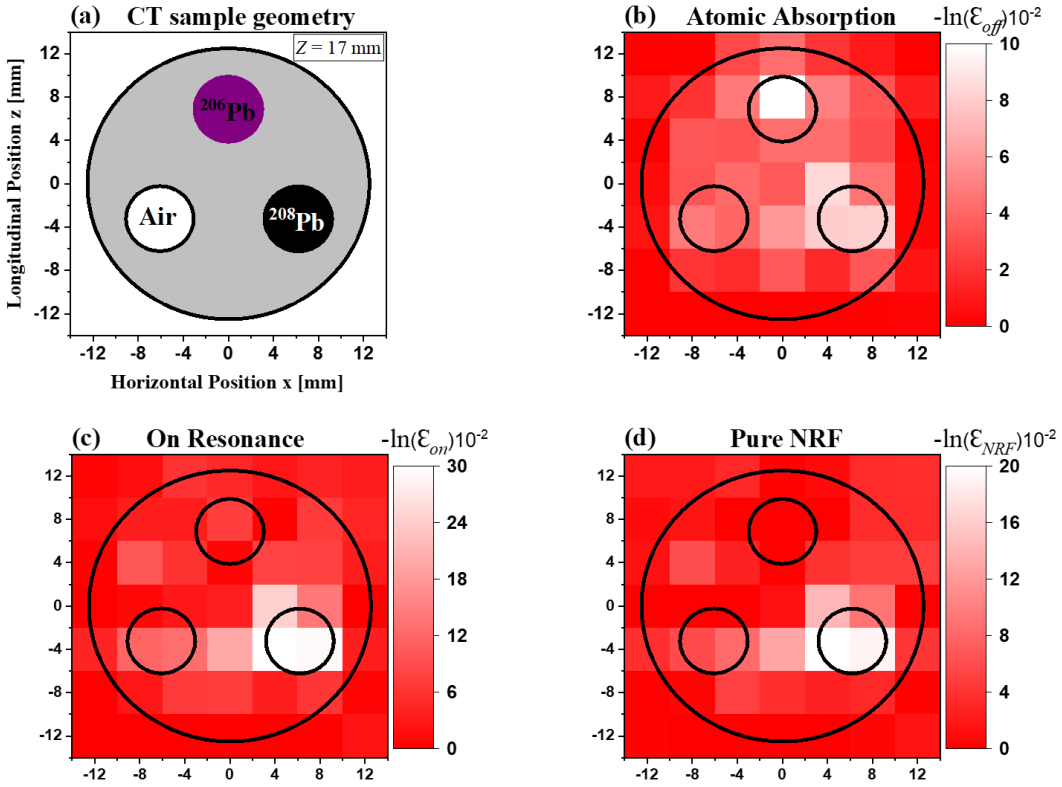

Figure 6. 10. (a) CT sample cross-sectional layer image at vertical distance of $z = 17$ mm (b) gamma − CT image, (c) on-resonance attenuation image, and (d) NRF − CT image

The NRF − CT imaging technique with isotope-selective capabilities, as proven in previous work [173], can clearly differentiate between two enriched lead isotope rods in the same investigated sample in 3D. In principle, any 3D − CT image may be created by assembling a series of 2D − CT scanned at different positions. Therefore, the 2D NRF − CT images produced in this investigation were combined to create a single 3D NRF − CT image using the visualization tool (MicroAVS) [184]. The visualized image had a horizontal resolution of 4 mm/pixel and a vertical resolution of 8 mm/pixel. Figure 6.11 shows a single view of the visualized 3D gamma − CT image captured at an oblique angle. Figure 6.12 (a– i) shows a series of shots of the visualization captured at a side angle of 20° from the movie of the 3D gamma − CT image (see Video S1 in the supplementary information of the reference [185]). The five zones of high attenuation caused by the atomic process, which correspond to the positions of

the five lead rods inside the investigated sample, are clearly visible in these series views. The atomic attenuation caused by the Fe rod, Al rods, or vacant space, on the other hand, was non-existent, making pinpointing their positions impossible.

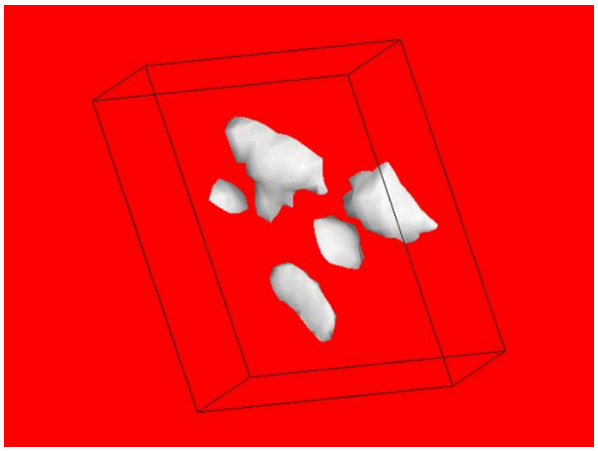

Figure 6.11. A single view from the visualization of the 3D gamma − CT image captured at an oblique angle in a resolution of 4 mm/pixel for the vertical plane and 8 mm/pixel for the horizontal plan.

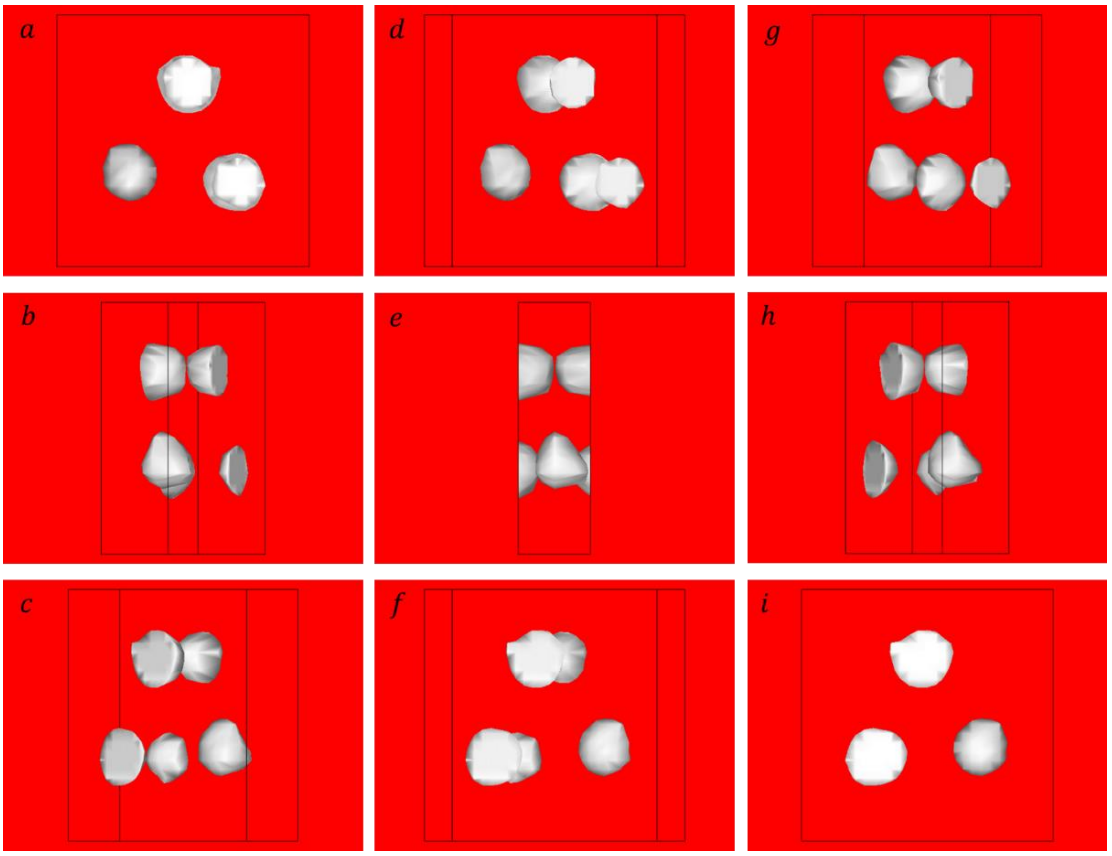

Figure 6.12. $(a - i)$ Consecutive views of the visualized three-dimensional movie of the gamma − CT imaging due to the off-resonant attenuation

Figure 6.13 shows a single view of the visualized 3D NRF − CT image captured at an oblique angle. Figure 6.14 (a–i) shows a series of shots of the visualization captured at a side angle of 20° from the visualized 3D NRF − CT images caused only by the ^{208}Pb (pure NRF). These views clearly show the locations of the three ^{208}Pb rods. In contrast, ^{206}Pb, Fe, and Al rods and the empty areas were invisible (see Video S2 in the supplementary information of reference [185]).

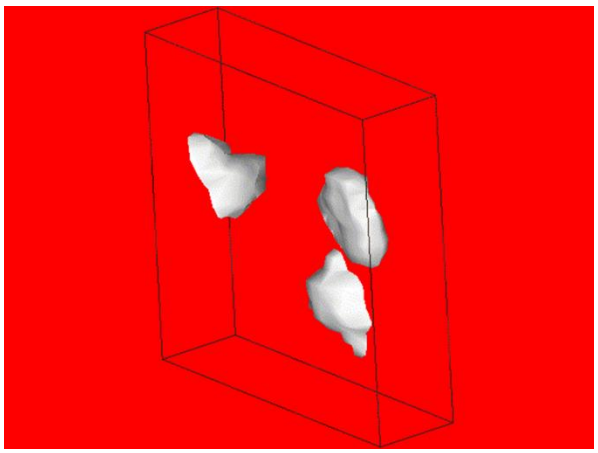

Figure 6. 13. A single view of the 3D NRF − CT image caused by the distribution of ^{208}Pb at a resolution of 4 mm/pixel for the vertical plane and 8 mm/pixel for the horizontal plane.

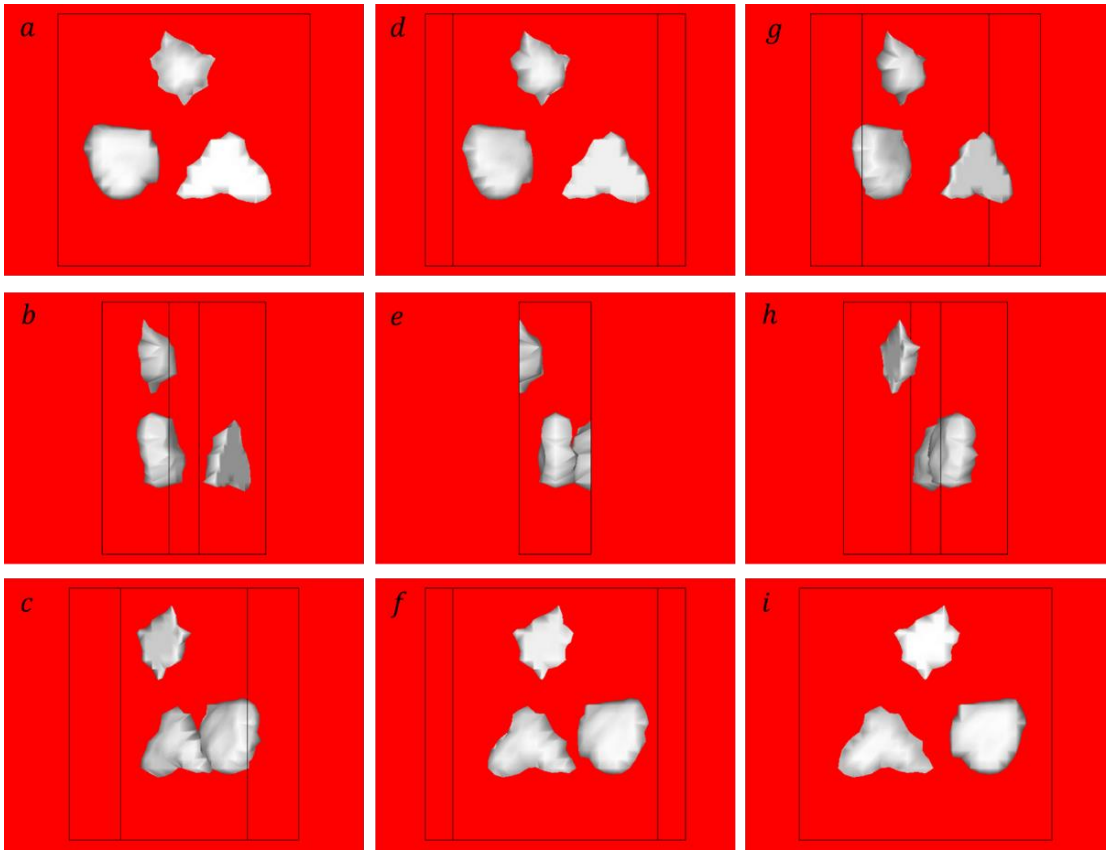

Figure 6. 14. Consecutive views of the movie of the visualized 3D NRF − CT image for the distribution of ^{208}Pb isotope

In the current study of this dissertation, we upgraded our measurement system. Consequently, we demonstrated isotope-selective CT imaging based on the NRF transmission method in 3D. The first presentation of the NRF − CT technique in 3D led to widespread usage of the technique in nuclear safeguards. It also aids in the quantification of hidden isotopes within the SNMs , particularly by enhancing the quality of the acquired images. A single 3D NRF − CT image of the investigated sample with a horizontal pixel resolution of 4 mm and a vertical pixel resolution of 8 mm for 3 vertical layers took roughly 48 hours to acquire. Although the horizontal resolution of the 3D NRF − CT image in this study was lower than that of the 2D NRF − CT image in the previous study (2 mm/pixel) [173], the improvement in the experimental set-up was positively reflected in the image acquisition time. One of the aims of this study was to see if the NRF − CT technique could be used in 3D with the

existing experimental setup at the UVSOR − III facility. As a consequence, the lack of image resolution acquired has not proven to be an impediment thus far. The 3D NRF − CT imaging method is still time-consuming. However, several solutions have been suggested to improve the image quality and reduce measuring time. One of the possible options is to improve the detection system by increasing the number of HPGe detectors used to measure the NRF signal scattered from the witness material. Increasing the gamma-ray beam intensity is another option. Although this is challenging under the current conditions for the UVSOR − III facility, the ELI − NP project is currently being built as a new LCS gamma-ray facility [166], with an expected flux density of the LCS gamma rays of 500 times higher than the current one. This upgrade will offer new and exciting possibilities in nuclear science research and 3D NRF − CT applications. Furthermore, various approaches to enhance the quality of the measurements based on a specific numerical treatment have been proposed. The employment of these approaches depends on the combination of two different CT images into a single image. We have already had success in developing this numerical technique, which has resulted in an immensely substantial improvement in the quality of the obtained 3D images without a considerable increase in measurement time. The implantation of these treatments will be discussed in greater depth in chapter 7 of this dissertation.

7 FUSION VISUALIZATION TECHNIQUE

7.1 Overview

In the first experimental study of this dissertation, we acquired an isotope-selective CT image in 2D based on the NRF transmission method for the distribution of enriched isotopes (^{208}Pb and ^{206}Pb) inserted into a cylinder holder made of thick aluminum. The resolution of the 2D NRF − CT image was 2 mm/pixel, and the data acquisition time was 60 hours [173]. As an outcome, those isotopes could be clearly distinguished. In a subsequent study [185], we added a one-dimensional scan in the vertical direction to measure an NRF − CT image in 3D with horizontal and vertical resolutions of 4 and 8 mm/pixel, respectively. The data acquisition time was 48 hours. In the case of the NDI for the hidden isotopes within an assembly volume, scientific visualization involves representing complex raw data as 2D or 3D images to understand the shape of the hidden isotopes that may be overlooked by standard methods alone. Increasing the image resolution acquired through the employment of the NRF − CT imaging technique is critical for realistic applications. Upgrading the detection effectiveness of the NRF measuring system and raising the gamma-ray intensity are two possible approaches for improving image resolution while maintaining a tolerable data acquisition time. However, applying these approaches is challenging under the current conditions of the UVSOR − III facility. Therefore, we developed an alternate technique that applied a numerical treatment, called the fusion visualization (FV) technique [186 – 190], to enhance the quality of the NRF − CT images. We applied this technique to the obtained 3D NRF − CT image in the previous chapter [185]. The term "data fusion" refers to a numerical data processing technique that combines multiple data sources to provide more meaningful, consistent, and accurate information. In our case, the FV technique is based on the integration of multiple data sources. One of the sources is the primary 3D NRF − CT image

[185], which provides the necessary isotope distribution but has poor image quality. Another data source is a 3D gamma − CT image in high-resolution measured for the same sample at the UVSOR − III facility under comparable experimental conditions, but with minor changes to the parameters of the LCS gamma rays [191]. In the current chapter, we describe the numerical treatment procedures of the FV technique to improve the quality of an isotope-selective 3D NRF − CT image. Furthermore, we evaluated a few alternative numerical treatments for the FV technique and talked about the obtained image quality.

7.2 Experimental procedures

The images used for these treatments were obtained utilizing the available LCS gamma-ray beams at the beamline BL1U in the UVSOR − III facility. Using an LCS gamma-ray beam at low intensity, we first measured the 3D gamma − CT image based on atomic absorption. Second, we measured the isotope-selective 3D NRF − CT image based on the NRF transmission method using an LCS gamma-ray beam in relatively high flux. In the following sections, after describing the details of the 3D gamma − CT image, we will briefly describe the experimental procedures for the 3D NRF − CT measurements because the details of its experimental procedures were described in detail in the previous chapter of this dissertation.

7.2.1 3D gamma − CT image measurements

Figure 7.1 illustrates the experimental setup used to measure the 3D gamma − CT image. A lead collimator (1 mm) was positioned in the path of the LCS gamma-ray beam to define its diameter and energy spectrum on the investigated sample. We operated the laser system at a typical average power of 2.4 W to generate an LCS gamma-ray beam with an intensity of 7.6×10^6 photons/s with 100% energy bandwidth at the FWHM before collimation [192]. After collimation, the LCS gamma-ray beam's properties were calculated

using the EGS5 Monte Carlo simulation code [172]. The calculated flux was 0.7 photons/s/eV at a maximum energy of 5.54 MeV with a 1.1% energy bandwidth at the FWHM. The beam diameter on the investigated sample was almost the same as the size of the hole in the collimator: roughly 1 mm, due to the modest divergence of the LCS gamma-ray beam (about 10^{-3}). The PL scintillator placed 1.8 m downstream from the collimator was used to measure the flux of the incoming LCS gamma-ray beam. After passing through the PL scintillator, the transmitted gamma rays were injected into the sample, which was mounted on the three-axis traveling stage 213 cm downstream from the collimator. The $LaBr_3(Ce)$ scintillation detector positioned 0.82 m downstream from the sample was used to estimate the flux of transmitted photons. This transmitted flux was analyzed to measure the sample's atomic attenuation. A 5-cm thick Bi absorber was installed in front of the $LaBr_3(Ce)$ scintillation detector to minimize the pileup events on the detector.

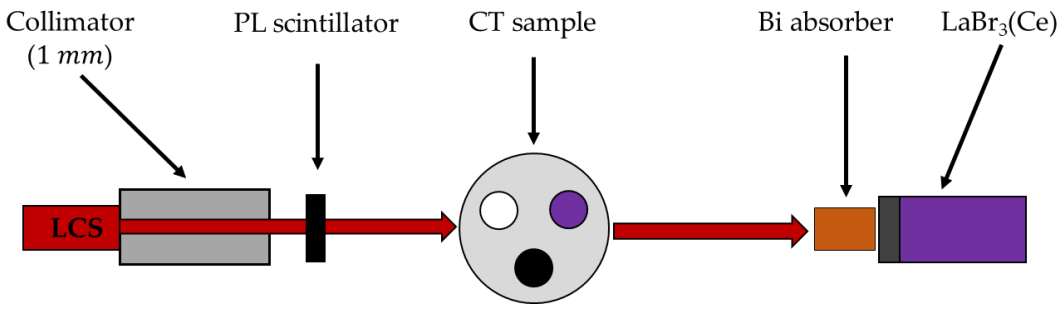

Figure 7. 1. The experimental setup to measure the 3D gamma – CT image

7.2.2 3D gamma – CT image scanning plan

We have used the same cylindrical aluminum container for the CT sample as previously described in figure 6.1 with the same concealed rods, including the isotope of interest (^{208}Pb). The developed scanning system, which was implemented with LabVIEW software, was used to perform the scanning of the 3D gamma – CT imaging. The CT sample was scanned along three axes as follows: (i) the vertical position (y) was fixed at a set position; (ii) 2D gamma –

CT images were scanned in the x-direction along the range of -12 to $+12$ mm with a step size of 1 mm. The sample was scanned in each horizontal position in the θ-direction along the range from 0° to 150° degrees with a step size of 30° degrees; (iii) (i) and (ii) were repeated for different vertical positions (y) 1 to 22 mm with a step size of 1 mm. We gathered 3300 data points in the presence of the CT sample by measuring 25 locations along the x-direction, 22 layers in the y-direction, and 6 rotational angles (θ). In addition, we measured one data point for each scan in the x-direction in the absence of the CT sample. Therefore, a total of 3432 data points were measured with an average measurement time of 5 seconds per data point. The overall time needed to obtain the 3D gamma $-$ CT image from all data points was approximately 5 hours. Table 7.1 summarizes the scanning procedures for the 3D gamma $-$ CT image.

Table 7.1 The scanning procedures for NRF $-$ CT imaging in three dimensions

Direction	Step size	Range	No. of points
θ	30°	0° ~150°	6
x	1 mm	$-12 \sim +12$ mm	25
y	1 mm	0 ~21 mm	22
Acquiring time for one position			5 seconds
Total measurement time			5 hours

7.2.3 3D NRF $-$ CT image measurements

We used an LCS gamma-ray beam with a relatively high flux to measure the 3D NRF $-$ CT image. As shown in figure 7.2, since the total flux of the gamma-ray beam was proportional to the average power of the laser with a proportional constant of 3.5×10^{6} photons/s/W, we used the laser system with a typical power of 36 W to generate the gamma rays. As a result, a total flux

higher than 10^8 photons/s with a 100% energy bandwidth could be generated. We used a collimator with a hole diameter of 2 mm, which is twice as wide as that of the collimator used for 3D gamma − CT image measurement. The flux of the LCS gamma-ray beam traveling through the collimator was numerically estimated using the EGS5 Monte Carlo simulation code [172], and thus, we found that the flux density was 10 photons/s/eV and that the maximum energy was 5.54 MeV with 2.9% energy bandwidth at the FWHM, which was able to excite the $J^{\pi} = 1^{-}$ NRF level at 5.512 MeV in ^{208}Pb. Although the isotope imaging with the NRF − CT technique is time-consuming, we were able to shorten the image acquisition time for each location during the scanning, which had been measured in our earlier study by adjusting the CT sample scanning pattern and increasing the LCS gamma-ray beam's intensity flux [173]. The overall time needed to acquire a 3D NRF − CT image was approximately 48 hours. The previous chapter gives more details on the experimental setup, the CT sample scanning plan, and a schematic diagram of the 3D NRF − CT image. Table 7.2 summarizes the difference in the LCS gamma-ray source for both 3D − CT images.

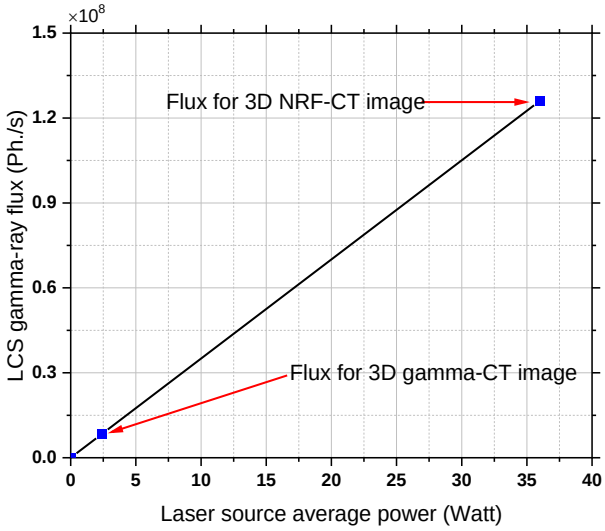

Figure 7. 2. The average power of the Tm-fiber laser source vs the generated gamma-ray intensity

Table 7.2 The differences in the LCS gamma-rays' source between the 3D NRF − CT imaging and the 3D gamma − CT imaging

	beam parameters	3D gamma − CT	3D NRF − CT
[2]Inputs	beam diameter	1 mm	2 mm
	laser power	2.4 W (CW)	36 W (CW)
Outputs	LCS intensity	0.7 photons/s/eV	10 photons/s/eV

7.3 Results and discussion of the FV technique

7.3.1 3D − CT primary images

In principle, CT imaging of objects can be performed by measuring the decrease in the gamma-ray intensity passing through the scanned sample along a series of linear pathways and angles. The amount of reduction is influenced by the gamma-ray energy, path lengths, and linear attenuation coefficients of the material. Therefore, one can obtain a gamma − CT image for a sample using the gamma-ray transmission factor measurements of the ε_{off}, which originate from the atomic effect. The methodologies for gamma − CT imaging techniques are described in detail in Chapter 5 of this dissertation [173]. Since the height of the CT sample holder was 20 mm, we divided the sample holder into 20 layers with a vertical spacing of 1 mm (figure 6.1). We also added two more layers, one below the holder's bottom and the other above it, for a total of 22 layers. The layers were given their names $L1$ to $L22$ at vertical distances of $y = -1$ mm to $y = 21$ mm, respectively. As a result, we obtained one 2D gamma − CT image (25×25) with a resolution of 1 mm/pixel for each row of rods in the y-direction of scanning. The pixel size of the measured images was determined by the scanning step in the x-direction. In total, 22 reconstructed 2D gamma − CT images were obtained, which we named $L_{\text{off}}1$ to $L_{\text{off}}22$. According to our

[2] The laser wavelength, spectral linewidth, and beam quality were same in both experiments

experimental setup conditions, layer $L1$ was beneath the sample holder, and layer $L2$ was at the holder's bottom edge. As a result, the LCS gamma-ray beam failed to pass through the inserted rods. Accordingly, the reconstructed gamma $-$ CT images for the first two layers $L_{\text{off}}1$ and $L_{\text{off}}2$ did not show any characterization of the hidden rods. The cross-sectional slices of the measured sample for the horizontal layers from $L3$ to $L8$ are shown in figure 7.3 (a). These layers had a total height of 6 mm, which was the same as the height of each rod within them. Two rods of ^{208}Pb and ^{206}Pb were inserted into two of the holes, and a Fe rod was installed into the third one. The reconstructed CT images from $L_{\text{off}}3$ to $L_{\text{off}}8$ due to the atomic attenuation measured by the $LaBr_3$(Ce) detector are shown in figure 7.3 (b). The two zones in the white-colored area of the high attenuation caused by the atomic process corresponding to the locations of the lead isotope rods were vividly visible in all images because these materials had the same atomic attenuation. However, it was difficult to distinguish between them. Furthermore, the Fe rod's atomic attenuation was less than that of the lead rods, causing the Fe rod to appear as a faint shadow.

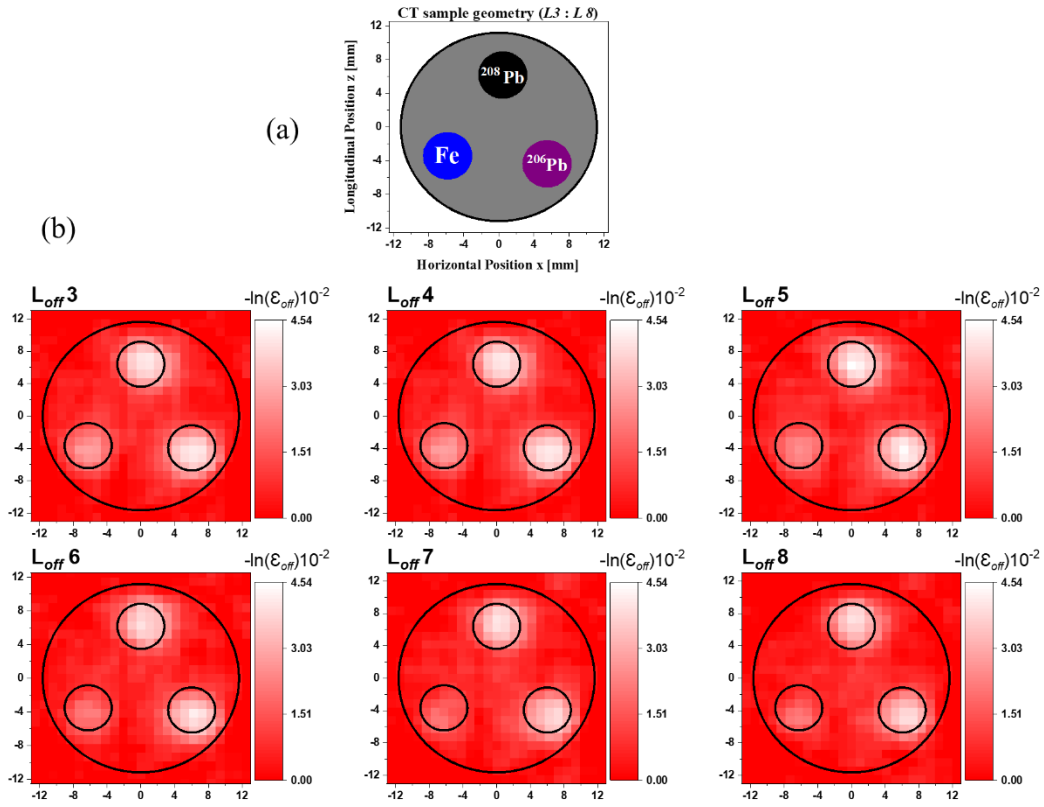

Figure 7. 3. (a) Cross-sectional slice images of the CT sample in the first 6 layers from $L3$ to $L8$ and (b) its 2D gamma − CT images with a resolution of 1 mm/pixel

The cross-sectional slices of the CT sample for the horizontal layers from $L9$ to $L14$ are shown in figure 7.4 (a). These layers had a total height of 6 mm as well. The first, second, and third holes were filled with ^{208}Pb, Fe, and Al rods, respectively. Figure 7.4 (b) shows the reconstructed gamma − CT images from $L_{\text{off}}9$ to $L_{\text{off}}14$. A high-attenuation zone induced by the atomic process of the ^{208}Pb rod is plainly evident. Since the CT sample holder was manufactured from aluminum, the Al rod was not visible.

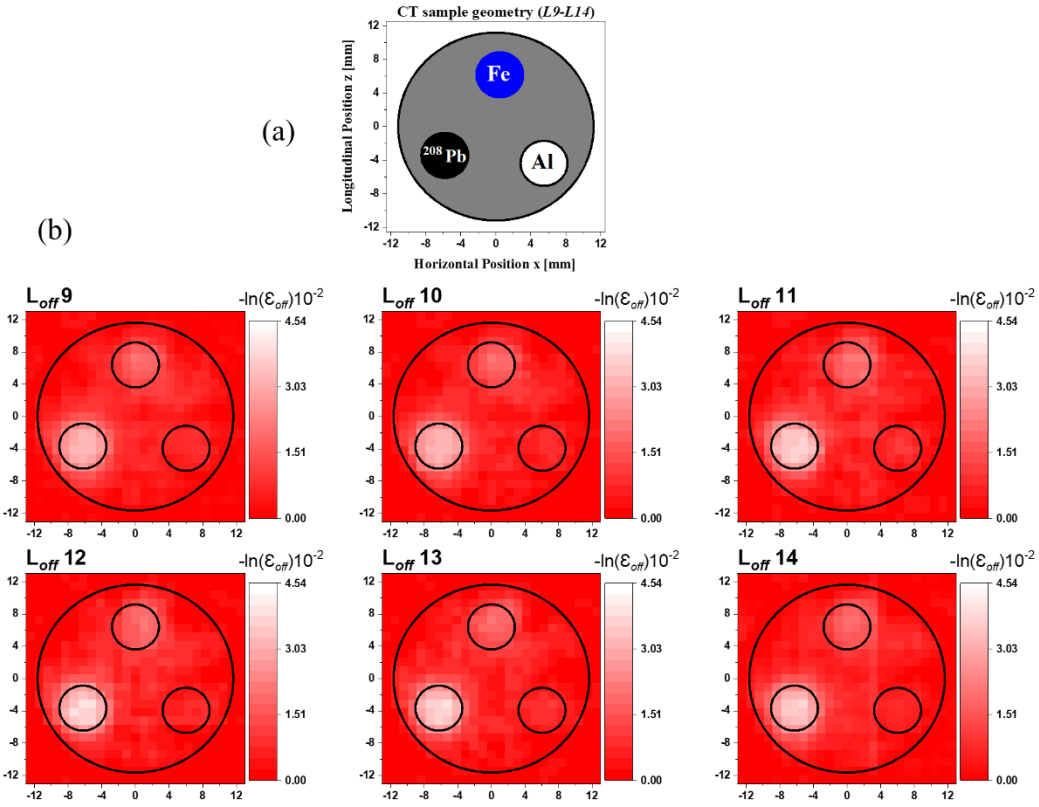

Figure 7.4. (a) Cross-sectional slice images of the CT sample in the second 6 layers from $L9$ to $L14$ and (b) its 2D gamma − CT images with a resolution of 1 mm/pixel

The resulted images for the layers from $L15$ to $L20$ are shown in figure 7.5. Two rods of ^{208}Pb and ^{206}Pb were inserted into the two holes, while the third hole remained unfilled. Figure 7.5 (b) shows the reconstructed images from $L_{\text{off}}15$ to $L_{\text{off}}20$. The two high-attenuation areas corresponding to the ^{206}Pb and ^{208}Pb rods can be clearly observed, but they cannot be distinguished. The low-intensity area at the third hole corresponds to the vacant space.

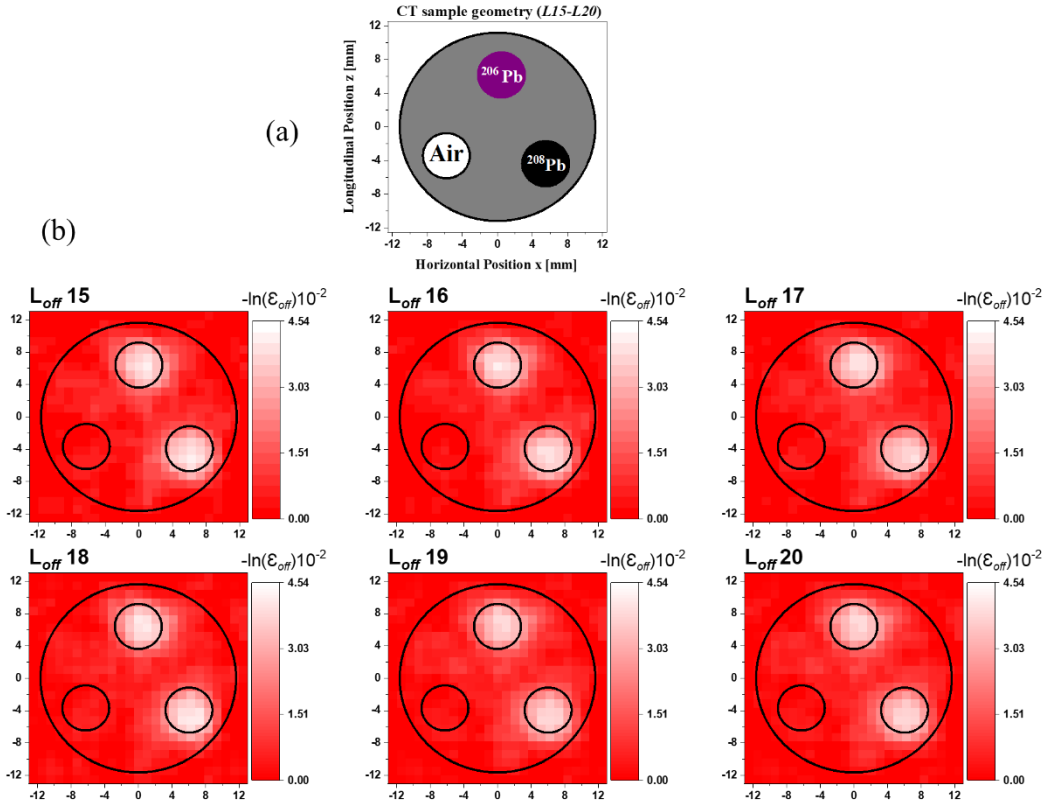

Figure 7.5. Cross-sectional slice images of the sample in the third 6 layers from $L15$ to $L20$ and (b) its 2D gamma − CT images with a resolution of 1 mm/pixel

Because layers $L21$ and $L22$ were situated above the inserted rods in the CT sample, the LCS gamma-ray beam did not pass through them. Therefore, similar to the first two layers $L1$ and $L2$, no characterization of any material can be seen in the images $L_{\text{off}}21$, and $L_{\text{off}}22$. The $2D-CT$ images collected at various positions were principally used to create the $3D-CT$ image. The obtained 2D gamma − CT images (22 layers) were visualized to create a single 3D gamma − CT image at a resolution of 1 mm/pixel. We also used the MicroAVS tool for the visualization process [184]. The 3D gamma − CT image can be seen in the movie S1 in the supplementary information of the reference [193]. Figure 7.6 shows a single view of the 3D gamma − CT image captured at an oblique angle. A series of shots of the visualization captured at 20° side angles are also shown in figure 7.7 (a– i).

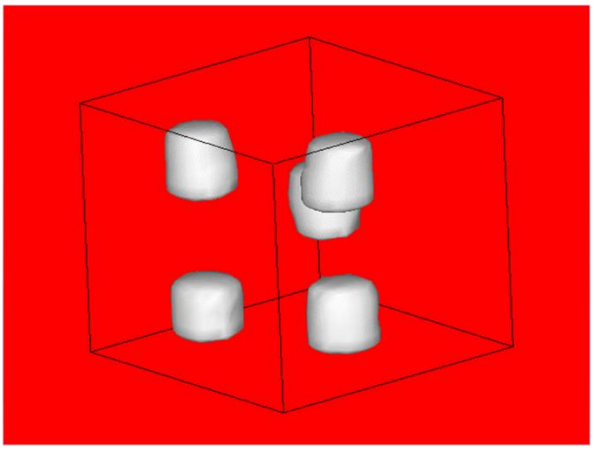

Figure 7. 6. A single view captured from the visualization of the 3D gamma − CT image at an oblique angle

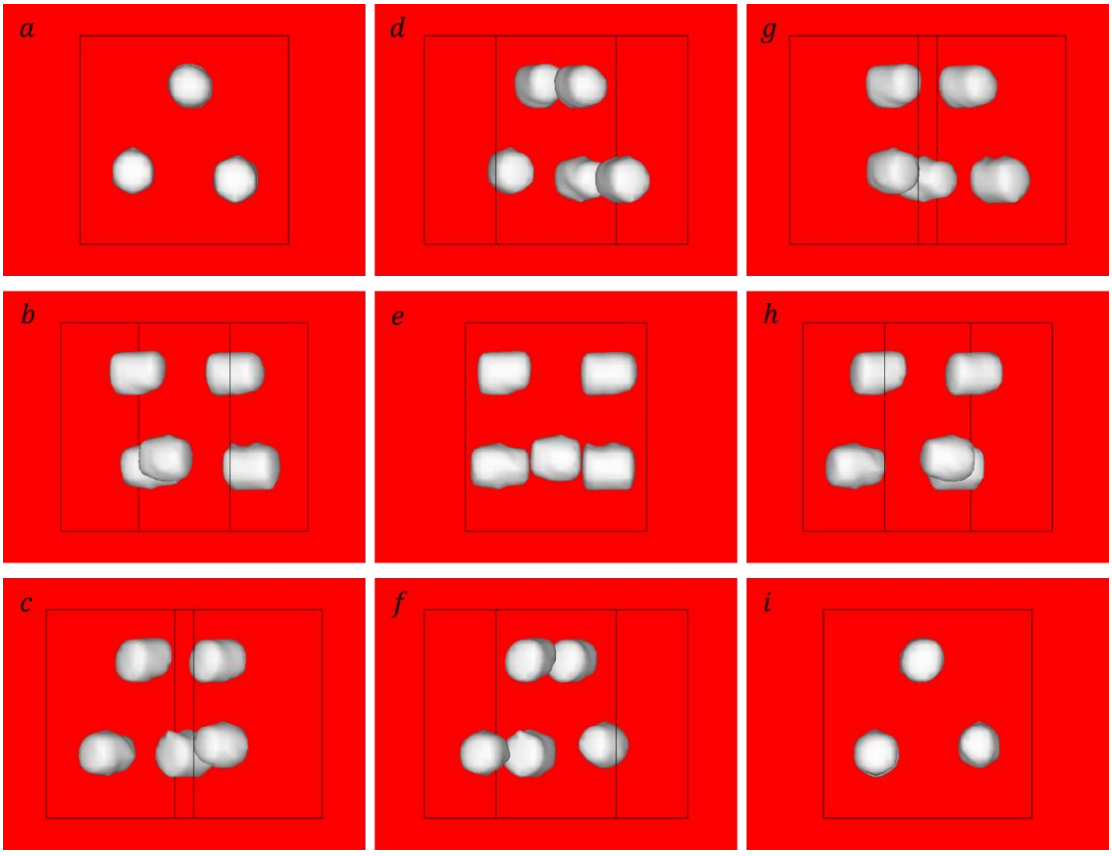

Figure 7. 7. A series of views of the visualization of the 3D gamma − CT image captured from a side angle of 20°

As a threshold limit for the visualization of the 3D surface, we set a value of approximately 60% of the highest intensity of the 2D gamma − CT images. This threshold limit assured that only the lead rods appeared on the 3D surface. Since the Fe or Al rods induced less atomic attenuation than the lead rods, this

threshold limit ensured that only the lead rods appeared on the 3D surface. Intensity values greater than the limit appeared in the 3D image. On the other hand, the intensity values less than the limit disappeared from the visualized image. The five areas of high attenuation induced by the atomic process, which correspond to the positions of the lead isotope rods, are clearly visible on the 3D surface of the gamma − CT image. We may infer from this section that the gamma − CT imaging technique can identify the existence of the materials to be investigated clearly. Furthermore, compared to NRF − CT imaging, we were able to obtain a 3D gamma − CT image with greater resolution and a quicker acquisition time. However, it lacked the isotope-selective capability needed to distinguish between different isotopes within the same sample. Therefore, in the following section, we will consider the 3D gamma − CT image as an additional information source to improve the quality of the 3D isotope-selective CT imaging based on the NRF transmission method. This paragraph will briefly describe the primary 3D NRF − CT image. As we described in Chapter 6 of this dissertation, we chose the layers at a vertical distance of $z = 3, 11,$ and 17 mm, measured from the holder's bottom, to reconstruct the 2D NRF − CT images of $L_{\mathrm{NRF}}4$, $L_{\mathrm{NRF}}12$, and $L_{\mathrm{NRF}}18$, respectively. Each horizontal row of rods produced one 2D NRF − CT image. We previously reported the visualization of reconstructed 3D images with resolutions of 4 or 8 mm/pixel for the horizontal and vertical planes, respectively, based on atomic attenuation and pure NRF attenuation [193]. If a 3D NRF − CT image were acquired using the current gamma-ray flux and detection efficiency available at the UVSOR − III facility's BL1U, the total time required to obtain a single 3D NRF − CT with a spatial resolution of 1 mm would be 2640 hours (about 3 and a half months). Thus, we need an alternative method to enhance the resolution of the 3D NRF − CT image without requiring a lengthy acquisition time. We developed an FV numerical treatment to obtain a higher-quality

image with a resolution of 1 mm/pixel with a measuring time shorter than that required to get the desired resolution without this treatment. We will go through the FV method in more depth in the following sections.

7.3.2 Post-multiply FV method (PMFV)

One of the FV numerical approaches is the so-called post-multiply FV method (PMFV), which analyzes a 3D gamma − CT image with a resolution of 1 mm/pixel as an additional data source to improve the resolution of the 3D NRF − CT image [193]. The following steps are the procedure of the PMFV method: sinograms adjustment, layer alignment (x, θ), 2D gamma − CT image segmentation, 2D − CT image overlapping, and image visualization in 3D.

7.3.2.1 Sinogram adjustment

The transmission factors ε_{off} and ε_{NRF} were collected in a 2D matrix which we called a sinogram. The sinogram size was determined by the scanning steps in the x-direction and the θ-angle. The 2D gamma − CT images were created by scanning the CT sample in the x direction with a step size of 1 mm step size spanning the range of -12 to $+12$ mm (25 positions). We also scanned the CT sample in the rotational direction (θ) with a 30° angle step spanning the range of 0° to 150° (6 angles). Therefore, we obtained sinograms of the ε_{off} transmission factor $M_{\varepsilon_{\text{off}}}(x_i, \theta_j)$ for each image in a matrix with a size of 25×6. Furthermore, the reconstructed 2D gamma − CT images had a matrix size of 25×25. For the 2D NRF − CT images, we scanned the sample in the x-direction with a 4 mm step size across the range of -12 to $+12$ mm (7 positions). We also scanned the sample in the θ-direction with an angle step of 30° across the range from 0° to 150° (6 angles). Therefore, we obtained sinograms of the ε_{NRF} transmission factor $M_{\varepsilon_{\text{NRF}}}(x_i, \theta_j)$ with a size of 7×6. The reconstructed 2D NRF − CT images had a matrix size of 7×7. To overlap both 2D − CT images resulting from the sinograms of the reconstructed transmission factors

$\varepsilon_{\mathrm{NRF}}$ and $\varepsilon_{\mathrm{off}}$, the images needed to be the same size in both directions (x and z). Therefore, we introduced a sinogram adjustment process to numerically divide each $\varepsilon_{\mathrm{NRF}}$ sinogram from $M_{\varepsilon_{\mathrm{NRF}}}(x_i, \theta_j)$ with a dimension of 7×6 to $M_{\tilde{\varepsilon}_{\mathrm{NRF}}}(x_i, \theta_j)$ with a dimension of 25×6 as follows: we divided each value in the x-direction equally into 25 values to create a sinogram (x, θ) with a dimension of 175×6. We then combined all consecutive 7 values together into one value to create a new sinogram in a dimension of 25×6. As a result of this process, the newly reconstructed images ($2\mathrm{D\ NRF}^{\sim} - \mathrm{CT}$) had a size of 25×25.

7.3.2.2 Layer alignment (x, θ)

We measured the 22 layers of the $\mathrm{gamma} - \mathrm{CT}$ measurement ($L_{\mathrm{off}}1$ to $L_{\mathrm{off}}22$) in addition to the 3 layers of the $\mathrm{NRF} - \mathrm{CT}$ measurement ($L_{\mathrm{NRF}}4, L_{\mathrm{NRF}}12,$ and $L_{\mathrm{NRF}}18$), and we aligned every $2\mathrm{D\ NRF}^{\sim} - \mathrm{CT}$ image to a group with 6 $2\mathrm{D\ gamma} - \mathrm{CT}$ images measured for 6 consecutive layers. Figure 7.8 illustrates the aligned layers in the vertical direction for both kinds of images. We aligned the $2\mathrm{D\ gamma} - \mathrm{CT}$ images from $L_{\mathrm{off}}3$ to $L_{\mathrm{off}}8$, which included the rods of ^{208}Pb, ^{206}Pb, and Fe, with the $2\mathrm{D\ NRF}^{\sim} - \mathrm{CT}$ image of $L_{\mathrm{NRF}}4$. We also aligned the $2\mathrm{D\ gamma} - \mathrm{CT}$ images from $L_{\mathrm{off}}9$ to $L_{\mathrm{off}}14$, which included the rods of ^{208}Pb, Fe, and Al, with the calculated $2\mathrm{D\ NRF}^{\sim} - \mathrm{CT}$ image of $L_{\mathrm{NRF}}12$. The $2\mathrm{D\ gamma} - \mathrm{CT}$ images from $L_{\mathrm{off}}15$ to $L_{\mathrm{off}}20$, including the ^{206}Pb, and ^{208}Pb rods, in addition to the vacant area, were aligned with the calculated $2\mathrm{D\ NRF}^{\sim} - \mathrm{CT}$ image of $L_{\mathrm{NRF}}18$.

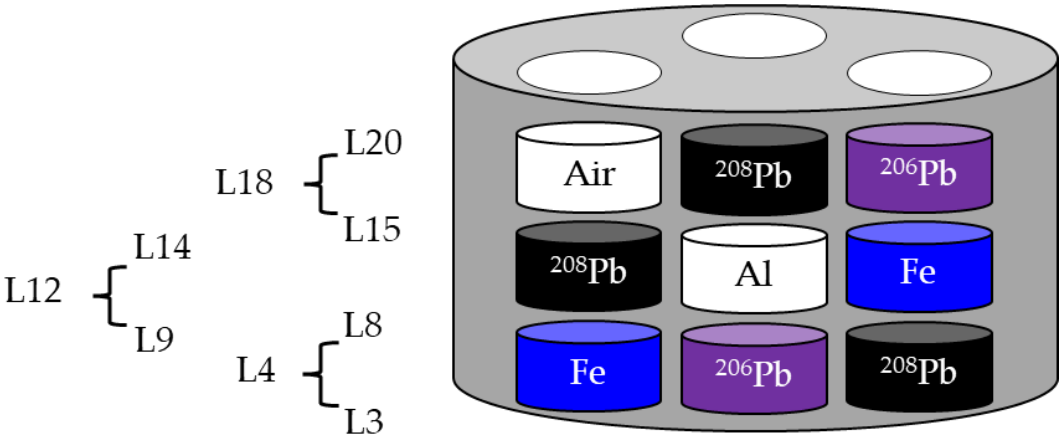

Figure 7.8. The aligned layers in the vertical z-direction between the 3D gamma − CT image and the 3D NRF − CT image

7.3.2.3 2D Gamma − CT image segmentation

Image segmentation is the division of an image into multiple segments or the positioning of pixels such that they do not overlap [192]. This segmentation procedure is the first stage of visualization, object representation, image analysis [194], and other image processing strategies used in a variety of fields [195]. Image segmentation's major purpose is to simplify and/or transform an image so that it can be easily analyzed [194]. In the case of applying the segmentation procedures to a 2D gamma − CT image like in the current study, we assumed that the atomic absorption intensities varied in some regions of the investigated sample and that the intensity at each pixel in a rod-containing area was almost constant. The first step of 2D gamma − CT image segmentation is the scaling of the primary image. We scaled the intensity scale for each primary gamma − CT image to a value between 0 and 255. This range was chosen to provide an 8-bit representation of each pixel. The black, and white colors were represented by the values of 0 and 255, respectively. The second step of 2D gamma − CT image segmentation is the thresholding process. The threshold method is one of the most extensively used image segmentation algorithms [194, 196]. Thresholding is important in a variety of image analysis, object representation, and visualization methods [197]. To apply the

thresholding for our 2D − CT images, we chose a threshold value (T_r) for transforming an image from grayscale into a binary image, in which each pixel has a value of 0 or 1, to distinguish the foreground and background of the image [198]. Accordingly, each pixel with an intensity greater (lower) than the T_r value will be shown by a white-colored (black-colored) area. In general, there are two kinds of threshold methods: local thresholding and global thresholding. In the case of using local thresholding methods, various threshold values are applied to different zones of the image. The neighborhood of the pixel to which the threshold is applied determines each T_r value [196, 199]. In the case of using global thresholding, a single T_r value is used to separate the foreground and the background for all pixels in an image [194, 200]. In the present treatment, we performed global thresholding with a common threshold T_r value of 128. The black and white 2D segmented gamma − CT images of the scanned layers are shown in figure 7.9, with the layers labeled from $L_{sg.}3$ to $L_{sg.}20$. The positions of the inserted rod turned entirely white, while the residual areas turned black. The image segmentation process produced a collection of segments that encompassed the whole image or a set of contours that served as the object's edge. Each pixel in the inserted rods' positions had a common property such as color or intensity. Furthermore, the neighboring areas differed substantially in terms of the same characteristics. When 2D segmented gamma − CT images are created for the employment of the FV technique with the NRF − CT images after the gamma − CT image segmentation, the resulting contours can be used to precisely preserve the ^{208}Pb rod locations within the gamma-ray images of the CT sample and cut the surrounding noise and distortions.

(a)

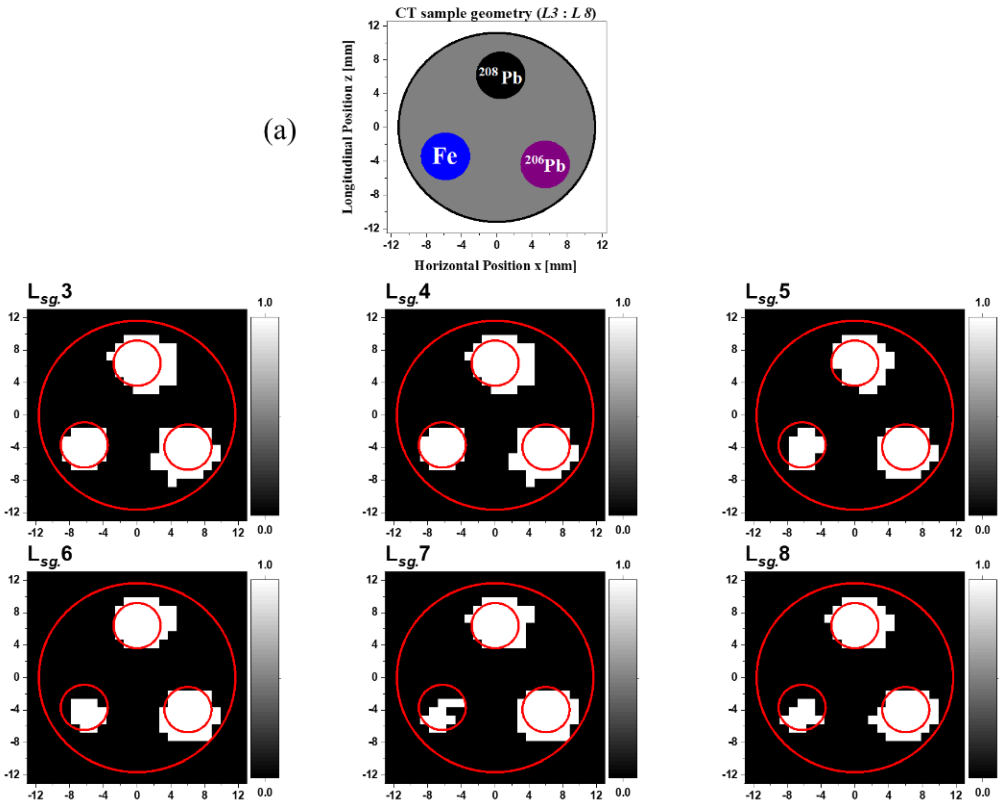
CT sample geometry (L3 : L 8)
Longitudinal Position z [mm]
Horizontal Position x [mm]
208 Pb
Fe
206 Pb
Lsg.3
Lsg.4
Lsg.5
Lsg.6
Lsg.7
Lsg.8

(b)

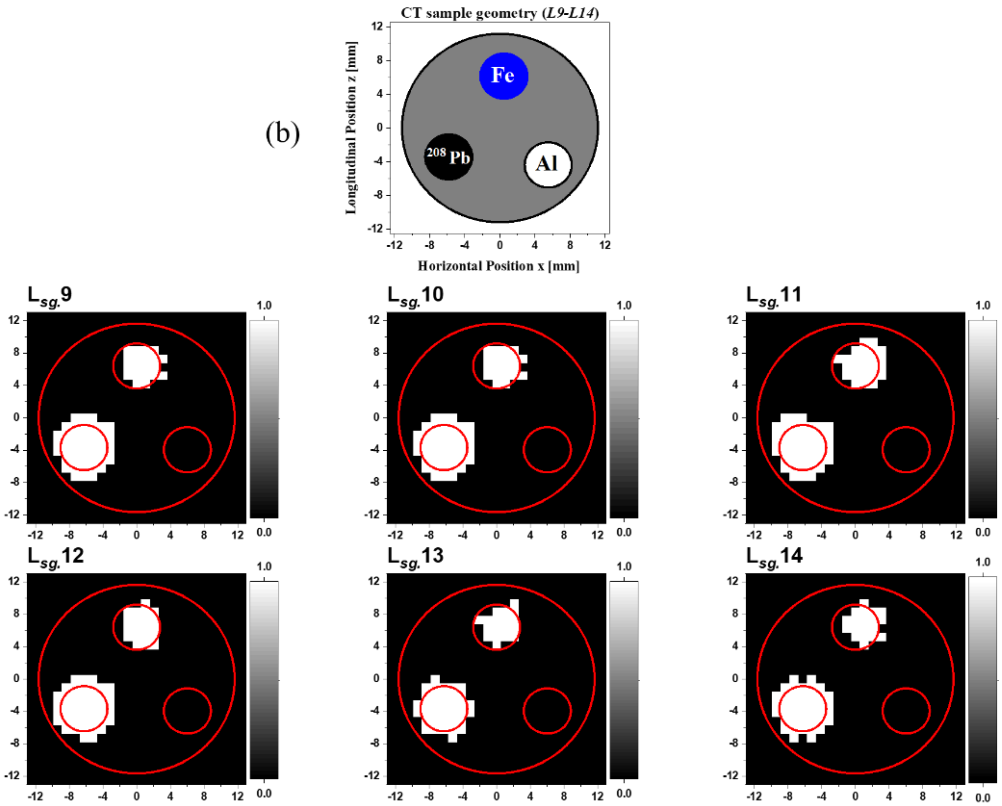
CT sample geometry (L9-L14)
Longitudinal Position z [mm]
Horizontal Position x [mm]
Fe
208 Pb
Al
Lsg.9
Lsg.10
Lsg.11
Lsg.12
Lsg.13
Lsg.14

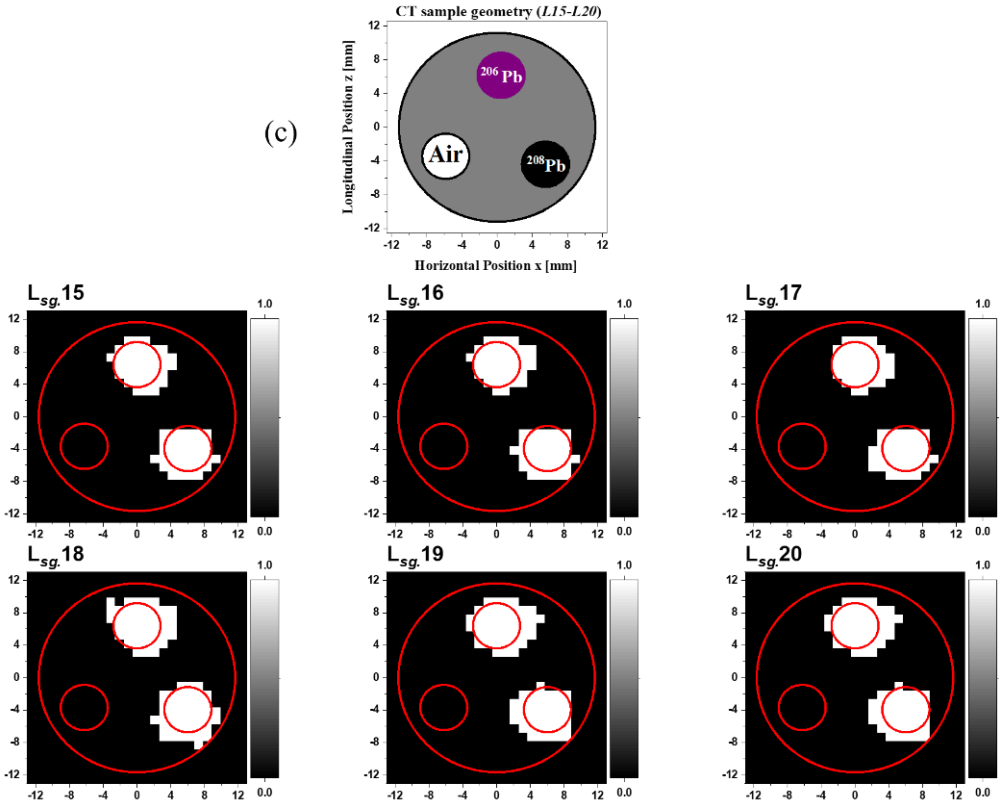

Figure 7. 9. (a– c) Cross-sectional layer images of the sample in the layers from $L3$ to $L20$, in addition to the binary $(0, 1)$ 2D $\mathrm{T_r}$ gamma $-$ CT images due to the segmentation process

7.3.2.4 2D $-$ CT image overlapping

To create the 2D FV NRF $-$ CT image, we overlapped the primary 2D $-$ CT images to obtain as follows: the 2D NRF~ $-$ CT images of Layers $L_{\mathrm{NRF}}4$, $L_{\mathrm{NRF}}12$, and $L_{\mathrm{NRF}}18$ were overlapped with the 2D segmented gamma $-$ CT images from $L_{\mathrm{sg.}}3$ to $L_{\mathrm{sg.}}8$, $L_{\mathrm{sg.}}9$ to $L_{\mathrm{sg.}}14$, and $L_{\mathrm{sg.}}15$ to $L_{\mathrm{sg.}}20$, respectively, according to the following equation:

$$\left[\text{2D FV NRF} - \mathrm{CT}(\mathrm{x_i}, \mathrm{z_j})\right] = \left[\text{2D NRF}^{\sim} - \mathrm{CT}(\mathrm{x_i}, \mathrm{z_j})\right] \times \left[\text{2D } \mathrm{T_r} \text{ gamma} - \mathrm{CT}(\mathrm{x_i}, \mathrm{z_j})\right]$$

Eq. (7.1)

We labeled the resulting 2D FV NRF $-$ CT images as $L_{\mathrm{FV}}3$ to $L_{\mathrm{FV}}20$. While the ^{208}Pb rod is clearly visible in the fused images from $L_{\mathrm{FV}}3$ to $L_{\mathrm{FV}}8$, as shown in figure 7.10 (a), the Fe and ^{206}Pb rods are almost invisible. Figure 7.10 (b)

shows the fused images from $L_{\mathrm{FV}}9$ to $L_{\mathrm{FV}}14$. Only the ^{208}Pb rod can be seen clearly, but neither the Fe nor the Al rods are visible. Moreover, we can clearly pinpoint the location of the ^{208}Pb rod in the reconstructed images from $L_{\mathrm{FV}}15$ to $L_{\mathrm{FV}}20$, as shown in figure 7.10 (c). The ^{206}Pb rod and the vacant area disappeared. Obviously, the noise in all 2D FV NRF − CT images' backgrounds caused by using the PMFV method was totally eliminated from the image's background, and the images look clear. Since the overlapping process of the PMFV method was performed by multiplying the intensity value at each pixel in the 2D NRF~ − CT by a value 1 within the ^{208}Pb locations or by a value 0 in the surrounding regions, the method preserved the locations of the isotopes of interest and completely eliminated the surrounding distortion and background noise. Furthermore, it kept the intensity value at each pixel constant, making this approach useful for isotope quantification.

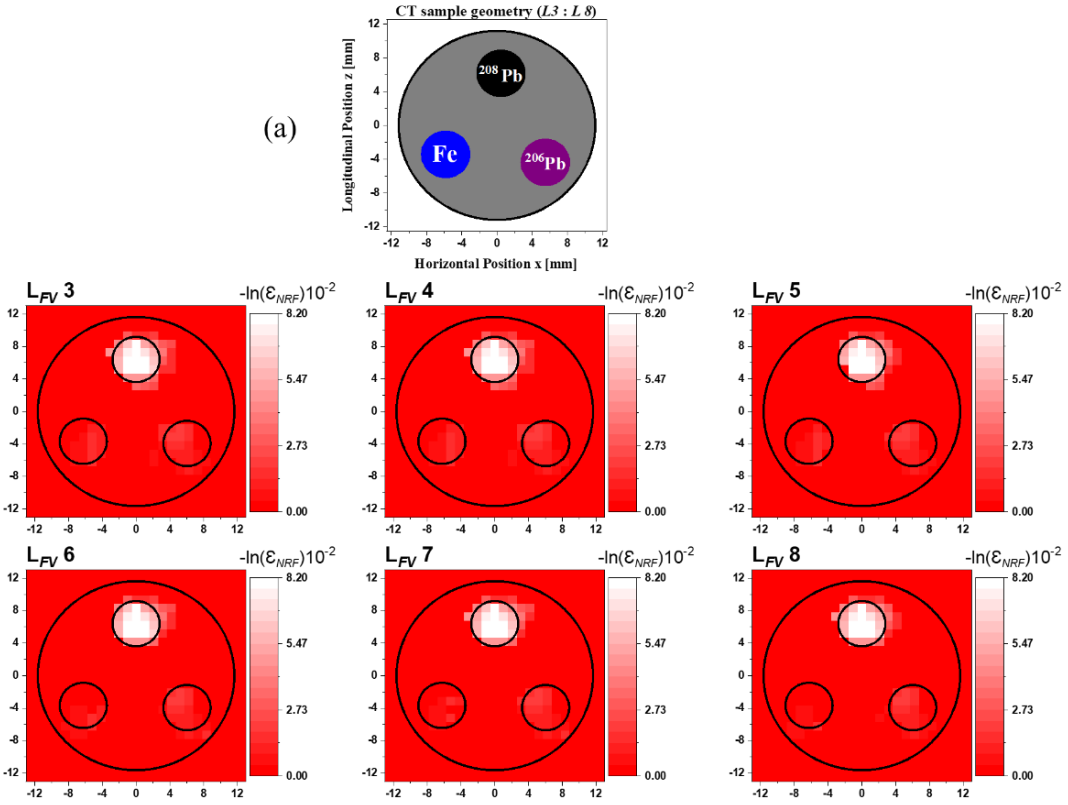

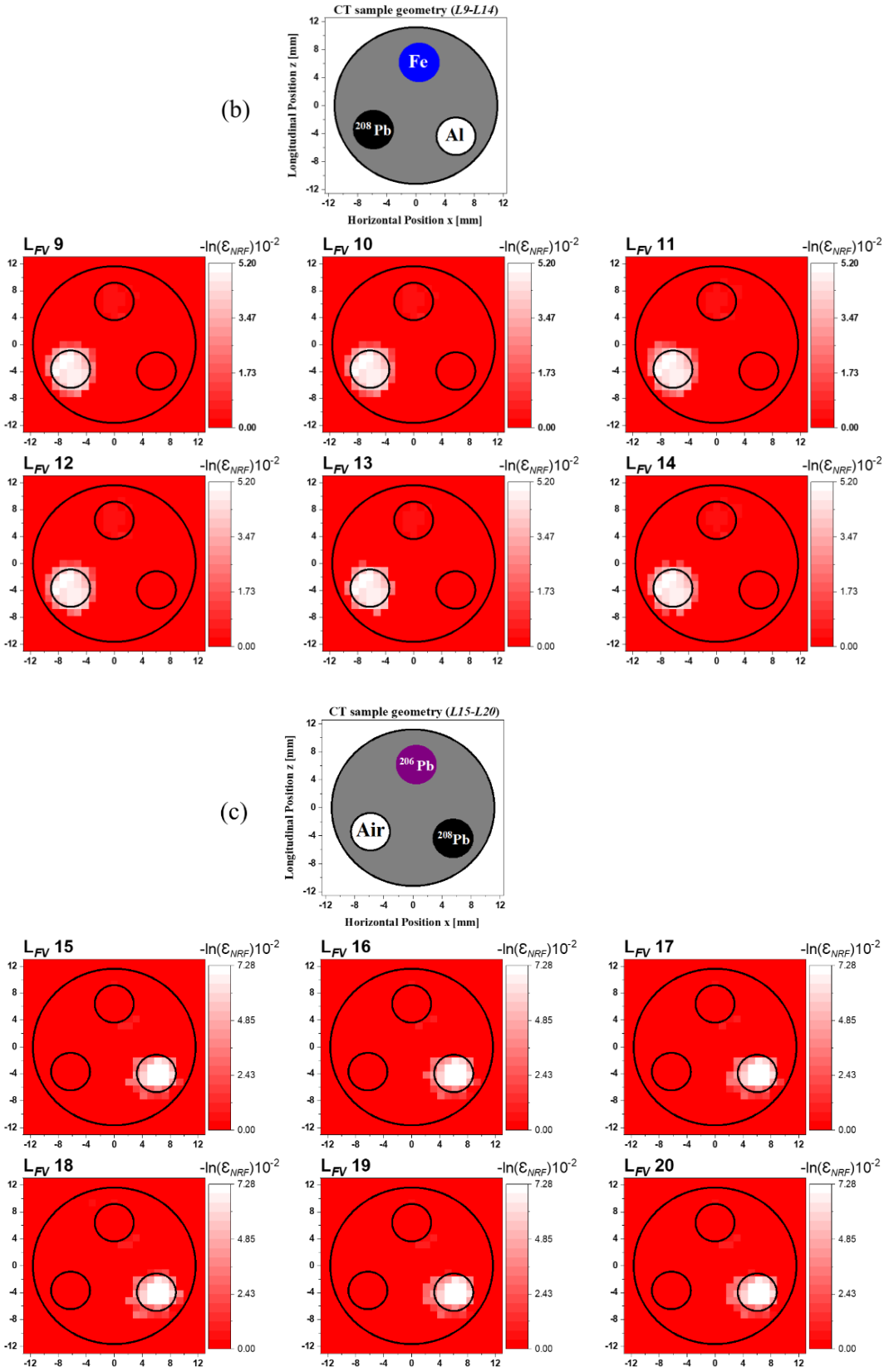

Figure 7. 10. Reconstructed 2D FV NRF – CT images from for the layers from (a) L3 to L8, (b) L9 to L14, and (c) L15 to L20 using the PMFV method with the CT sample's geometry for each layer group

7.3.2.5 Image visualization in 3D

The obtained 2D FV NRF − CT images were combined using the MicroAVS data visualization tool [184] to create a single 3D FV NRF − CT image. We also adjusted a value within the intensity range of the 2D FV NRF − CT images as a threshold limit, so that only the intensity values greater than the threshold limit (^{208}Pb rods) appeared on the 3D surface. Figure 7.11 shows a single view of the 3D FV NRF − CT image, which was captured from the visualization of the fused image of the NRF attenuation caused by the ^{208}Pb isotope within the CT sample (pure NRF) in 3D (see movie S2 in the supplementary materials of reference [193]). Figure 7.12 (a–i) also displays a series of shots of the visualization taken at a 20° side angle. The visualization clearly shows the locations of the ^{208}Pb rods. In contrast, the rods of ^{206}Pb, Fe, and Al and the empty areas are not visible.

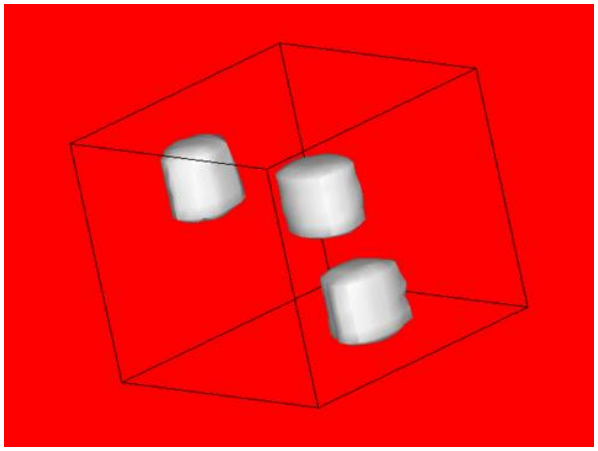

Figure 7.11. A single view of the 3D FV NRF − CT image caused by the distribution of ^{208}Pb isotope

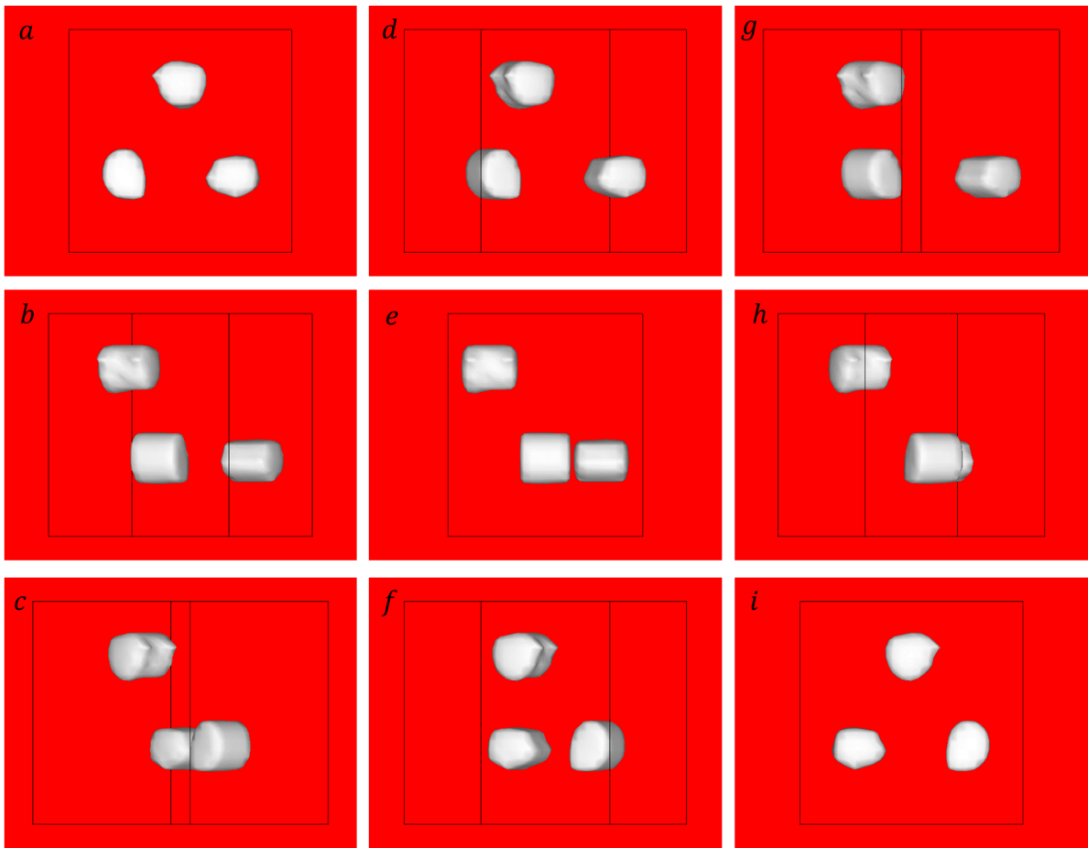

Figure 7. 12. A series of views of the 3D FV NRF − CT image caused by the distribution of ^{208}Pb isotope captured from a side angle of 20°

We conclude that we were able to obtain an isotope-selective 3D FV NRF − CT image with a resolution of 1 mm/pixel for the distribution of an enriched lead isotope (^{208}Pb) implanted with rods of dissimilar materials within a cylinder holder of 20 mm height and 25 mm diameter. Since the fused image has the same pixel resolution as the primary gamma − CT image, the image distortion and the background noise vanished, and the locations of the ^{208}Pb rods were clearly apparent. In contrast, the other rods completely disappeared since their intensity levels were less than the 3D surface's specified threshold limit. As a result, combining a primary 3D NRF − CT image with a high-resolution 3D gamma − CT image using the PMFV technique resulted in a significant increase in image resolution and isotope selectivity in CT imaging based on the NRF transmission method in 3D.

7.3.3 Different approaches to applying the FV technique.

The numerical treatment of the FV technique can be employed in different approaches for primary $3D-CT$ images. Most of these procedures are comparable to the PMFV method, except for a few minor differences. Although the different approaches might be effective in other applications. However, it reveals certain limitations in our case of study. One of the approaches can be employed by direct overlapping of the $2D\ gamma-CT$ image with the $2D\ NRF-CT$ image without the segmentation process, according to the following formula for the overlapping process:

$$\left[2D\ FV\ NRF-CT\ (x_i, z_j)\right] = \left[2D\ NRF^{\sim}-CT\ (x_i, z_j)\right] \times \left[2D\ gamma-CT\ (x_i, z_j)\right]$$

Eq. (7.2)

Although in our scenario, the quality of the $2D\ FV\ NRF-CT$ image obtained using this approach was acceptable, the intensity at each pixel of the $NRF-CT$ image was not preserved, hence it could not be utilized for isotope quantification. Furthermore, even if background noise were greatly decreased, total noise elimination would be unattainable. Another approach that can be applied is the post-sum FV method (PSFV) . Similarly, these approach procedures are comparable to the PMFV method, but the overlapping equation is written as follows:

$$\left[2D\ FV\ NRF-CT\ (x_i, z_j)\right] = \left[2D\ NRF^{\sim}-CT\ (x_i, z_j)\right] + \left[2D\ gamma-CT\ (x_i, z_j)\right]$$

Eq. (7.3)

The PSFV method produces a fused image that indicates the change in intensity at each pixel while still retaining some background noise, making it worthless for isotope quantification. Figure 7.13 shows a comparison between the $2D\ FV\ NRF-CT$ images of one of the scanned layers obtained by the methods of (a) PMFV, (b) PMFV (off segmentation), and (c) PSFV.

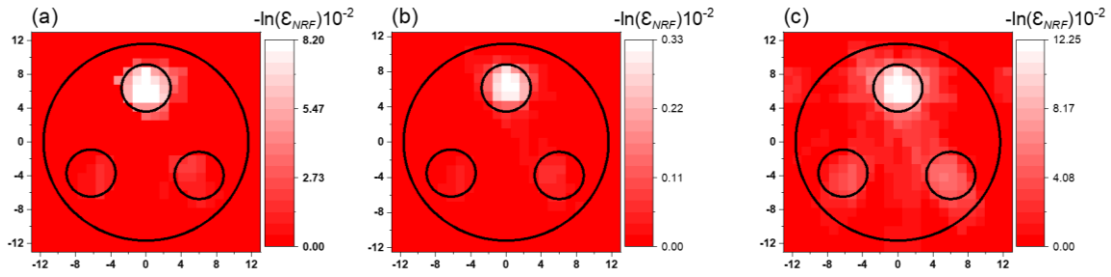

Figure 7.13. (a) Fused 2D NRF − CT images obtained via the PMFV method, (b) PMFV method (off segmentation), and (c) PSFV method

We conclude that using the preceding approaches for FV treatments of the NRF − CT imaging may change the intensity of each pixel, making it impossible to preserve the amount of the isotope of interest, which makes it ineffective in the isotope quantification inspection. Furthermore, even if the noise can be considerably reduced, it cannot be fully eliminated. As a result, we recommend the PMFV method as the best way for the NRF − CT imaging technique, which may be used in different fields, including nuclear safety and nuclear engineering.

8 CONCLUSIONS AND FUTURE PERSPECTIVE

8.1 Up to date

Non-destructive inspection (NDI) technology for nuclear materials is important for nuclear safeguards, nuclear waste management, and nuclear material non-proliferation. Bertozzi et al. [28] proposed the nuclear resonance fluorescence (NRF) method for measuring isotopes of interest using Bremsstrahlung gamma rays. The NRF inspection can provide isotope-specific signatures for a wide variety of materials because of the dependency of the excitation energy on the nuclear species (isotope). As a result, it may be used to look into exotic nuclear materials, commercial contraband, and explosives. The ability of the NRF imaging technique as an NDI technology in safeguard applications lies in its ability to directly measure a specific isotope in an assay volume without having to unfold or destroy the combined responses of several fissile isotopes, as other standard NDI methods frequently require. A MeV energy region gamma-ray beam generated by laser Compton scattering (LCS) interaction on relativistic electron beams is an excellent probe for the NDI of high-density materials because of its strong penetrability. Energy tunability, quasi-monochromatic energy spectrum, adjustable polarization, directionality, and high flux are all unique characteristics of the LCS gamma rays. The LCS gamma-ray beams with energies in the MeV range are now accessible for fundamental research and applications at the ultraviolet synchrotron orbital radiation-III (UVSOR − III) synchrotron radiation facility at the Institute of Molecular Science at the National Institutes of Natural Sciences in Japan. Computed tomography (CT) is a type of cross-sectional imaging that has a wide range of uses, including medical imaging. Furthermore, CT systems using x-rays are utilized to check bags at airports all around the world. It will be difficult to discern between isotopes in nuclear material, including a set of isotopes with almost atomic attenuation in atomic processes using traditional

gamma − CT techniques based on atomic attenuation of gamma rays. The combination of CT with the NRF (NRF − CT) has been proposed for visualizing isotopes inside massive materials. The implementation of NRF − CT as an isotope imaging technique has been developed, allowing NDI to identify concealed isotopic compositions. N. Kikuzawa et al. [44] used NRF gamma rays with LCS gamma-ray beams in a proof-of-principle experiment for NDI. As a simulant for special nuclear materials (SNMs), a lead isotope distribution of ^{208}Pb was detected within an iron box. Our research group recently completed a proof-of-concept for NRF − CT imaging utilizing an LCS gamma-ray beam available at the UVSOR − III facility [127]. We measured a two-dimensional (2D) NRF − CT image with a resolution of 5 mm/pixel for a natural lead isotope implanted within an aluminum cylinder based on the NRF transmission method. One of the most impressive advantages of the NRF − CT imaging technique is that it can selectively identify the isotope of interest from a sample containing many isotopes, which is a huge achievement in nuclear engineering. In the first experimental section of this dissertation, and for the first time, the isotope-selective capability of CT imaging based on the NRF transmission method using quasi-monochromatic LCS gamma-ray beams in the MeV region for enriched lead isotopes (^{206}Pb purity > 93.3 % and ^{208}Pb purity > 97.8 %) implied within a cylinder aluminum holder of 20 mm and 25 mm in height and diameter, respectively, was successfully demonstrated. The gamma rays were generated when an intense laser beam collided with relativistic electrons via the Compton scattering interaction. The experiment was conducted at the UVSOR − III facility's beamline BL1U with a Tm-fiber laser system (50 W, CW) with an 1.896 μm wavelength, and maximum energy of 746 ± 1 MeV for the electron beam (300 mA beam current) within the UVSOR − III's storage ring. The generated LCS gamma-ray beam had an intensity flux of approximately 5.5 photons/s/eV at a maximum energy of 5.54 MeV, which was able to excite the

resonance energy $J^{\pi} = 1^{-}$ at 5.512 MeV in ^{208}Pb. The size of the LCS gamma-ray beam and the spectrum energy at the investigated sample were defined using a lead collimator with a hole diameter of 1 mm. The CT sample was scanned with a 2 mm step size along the horizontal axis, from −14 to 14 mm, and a 30° angle step in the rotation angles from 0° to 150°. The CT image of the ^{208}Pb rod was obtained selectively with a 2 mm pixel size resolution, as determined by the CT sample step size in the horizontal direction. Because of the atomic attenuation effect, both the ^{208}Pb and ^{206}Pb rods were visible in the preliminary image. The signal from the ^{206}Pb rod was reduced after the atomic attenuation effect was removed, resulting in the selected imaging of the ^{208}Pb isotope. The data acquisition duration for the reconstructed 2D NRF − CT image was around 60 hours [173]. In the second experiment, and also for the first time, we created a three-dimensional (3D), isotope-selective CT image based on the NRF transmission method of an enriched lead isotope (^{208}Pb) distribution hidden inside a cylindrical aluminum holder with another enriched lead isotope (^{206}Pb), iron (Fe), and aluminum (Al) rods, and vacant area. The experiment was conducted using an LCS gamma-ray beam with a 5.54 MeV maximum energy, 2 mm beam size, and 10 photon/s/eV flux density, which is available at the same beamline in the UVSOR − III facility. We created 2D − CT images for each row of rods using atomic attenuation and NRF attenuation. Both images had a resolution of 4 mm/pixel. The lead isotope rods were visible in the atomic attenuation images. On the other hand, only the ^{208}Pb rods were visible in the NRF attenuation images. The isotope distribution of ^{208}Pb was shown in a 3D NRF − CT image with 4 and 8 mm/pixel sizes in the horizontal and vertical planes, respectively. The 3D isotope-selective image was accumulated in 48 hours [185] . By improving measurement efficacy, such as increasing the number of detectors to measure NRF signals, increasing the gamma-ray intensity, and developing advanced data processing techniques, further

improvements in image quality and a reduction in acquisition time will be possible, which will be a significant advancement in nuclear engineering for using the 3D NRF − CT technique in real applications. Under the current experimental circumstances of the UVSOR − III facility, increasing the detection efficiency or upgrading the source of photons is a challenge. Consequently, we proposed employing the fusion visualization (FV) methodology to increase the NRF − CT image quality without taking lengthier measurements. In our case, the FV methodology may be employed as an efficient numerical treatment to improve CT imaging based on the NRF transmission method by merging a 3D NRF − CT image with a 3D gamma − CT image with better pixel resolution. Both images were measured under the same experimental conditions as the beamline BL1U in the UVSOR − III facility, with the exception of the gamma-ray parameters for the same sample. For the two experiments, we used LCS beams with different intensities and beam diameters. First, we generated an LCS gamma-ray beam with a diameter of 1 mm and a flux of 0.7 photons/s/eV to measure the 3D gamma − CT image with a resolution of 1 mm/pixel [191]. Next, we generated an LCS gamma-ray beam with a diameter of 2 mm and a flux of 10 photons/s/eV to measure the 3D NRF − CT image with a resolution of 4 and 8 mm/pixel in the horizontal and vertical planes, respectively. We applied the FV technique using the post-multiply FV method (PMFV) between the two primary images to create a 3D isotope-selective fused CT image based on the NRF transmission method (3D FV NRF − CT) for the distribution of ^{208}Pb in the investigated sample. Background noise was eliminated from the fused 3D image, while the amount of the isotope of interest was preserved. The direct overlapping method (off segmentation) and the post-sum FV method (PSFV) were also considered, but we eventually found that the PMFV method was the best for isotope-selective CT imaging in nuclear engineering and other nuclear applications [193].

8.2 Future perspective

Although we were able to develop an isotope selective CT imaging technique based on the NRF transmission method and identify a single isotope, further study is needed to measure multiple isotopes within the same volume. In addition, for the quantitative information of these isotopes to be applicable for practical implementation, particularly in the management of nuclear waste, therefore, we would like to propose the following:

(i) The development of multiple isotope identification and quantification in the NRF − CT imaging technique using LCS gamma rays is available in the UVSOR − III facility.

(ii) A simulation study on NRF − CT imaging of SNMs ($^{235,\ 238}$U, and ^{239}Pu) mapping and characterization in nuclear waste and spent nuclear fuel under highly activated conditions is underway to open up a practical application of the NRF − CT imaging technique.

The key factor of the future plan is to get a full understanding of the hidden isotopes within an assay volume to be applicable in a realistic application. The first objective is to simultaneously measure many isotopes within a sample. Therefore, our research group has already started to conduct the basic experiments using the LCS gamma-ray beams at the beamline BL1U in the UVSOR − III facility to measure multiple enriched lead isotopes such as ^{208}Pb, ^{207}Pb, and ^{206}Pb simultaneously, which can be achieved by preparing a corresponding witness material. Moreover, we would need to develop the NRF − CT imaging technique to shorten the measurement time and improve the obtained image quality. Finally, we plan to conduct the isotope distribution with density quantification in the natural material samples, such as the Galena. The second objective in the future plan is to improve the simulation of the NRF − CT imaging technique for SNMs ($^{235,\ 238}$U, and ^{239}Pu) mapping and

characterization in spent nuclear fuel under highly activated conditions. The Monte Carlo simulation (GEANT4) code for modeling and optimization of NRF experimental parameters will be used to simulate the NRF − CT imaging in 3D under the Extreme Light Infrastructure—Nuclear Physics (ELI − NP) facility, where about 3 orders of magnitude higher intensity of quasi-monoenergetic gamma-rays will be available. Professor Hideaki Ohgaki (Kyoto University) has been appointed to conduct the industrial application program in ELI − NP and the first day of experiments is scheduled soon. In the case of satisfying the future plan, we will be able to investigate the feasibility of isotope mapping in nuclear waste by developing the NRF − CT imaging technique (objective 1) using LCS gamma-ray beams in conjunction with the GEANT4 simulation code (objective 2) to control the SNMs under nuclear safeguards regulations in the world and to promote their use for industrial applications.

9 REFERENCES

[1] National Research Council (US) Committee on Medical Isotope Production Without Highly Enriched Uranium, Medical Isotope Production Without Highly Enriched Uranium, Washington, DC: National Academies Press, 2009.

[2] Khalid Al Nabhani, Faisal Khan, Nuclear Radioactive Materials in the Oil and Gas Industry, 1ed., Elsevier, 2020, p. 328.

[3] International Atomic Energy Agency, IAEA Safety Glossary, Terminology Used in Nuclear Safety and Radiation Protection, 2018ed., Vienna: IAEA, 2019.

[4] International Atomic Energy Agency, Energy, Electricity and Nuclear Power Estimates for the Period up to 2050, 2021ed., Vienna: IAEA, 2021.

[5] International Atomic Energy Agency, World Energy Outlook, Paris: IAEA, 2021.

[6] Frank Barnaby, How to Build a Nuclear Bomb: and other Weapons of Mass Destruction, New York: Nation Books, 2004.

[7] Jeremy Bernstein, Nuclear Weapons: What You Need to Know Illustrated Edition, Illustrated ed., Cambridge University Press, 2010, p. 316.

[8] K. Linga Murty, Indrajit Charit, An Introduction to Nuclear Materials, Fundamentals and Applications, 1ed., Wiley-VCH, 2013, p. 398.

[9] United States Nuclear Regulatory Commission, Protection People and the Environment, "Nuclear Materials," 04 November 2021.

https://www.nrc.gov/reading-rm/basic-ref/glossary/fissile-material.html.

[10] Abe Tomoyuki, Ackland Graeme J., Aerts Alexander, Agarwal Renu, Agarwal Shradha, Alemberti Alessandro, Allen Todd R., Ambard Antoine, Andresen Peter L., Asakura Koichi, Asta Mark, Comprehensive Nuclear Materials, 2ed., R. E. S. Rudy J. M. Konings, Ed., Elsevier Ltd, 2020, p. 4868.

[11] Atomic Energy Act of 1954 (P.L. 83–703), Nuclear Regulatory Legislation 113th Congress. 2nd Session, vol. 1, Washington: Office of the General Counsel, 2015.

[12] World Nuclear Association, "Hiroshima, Nagasaki, and Subsequent Weapons Testing," 2016. https://www.world-nuclear.org/information-library/safety-and-security/non-proliferation.aspx.

[13] Y. R. Rodriguez, "Plutonium," in *Encyclopedia of Toxicology*, 3ed., P. Wexler, Ed., Academic Press, 2014, pp. 982-985.

[14] Arthur K. Parpart, "The permeability of the mammalian erythrocyte to deuterium oxide (heavy water)," *Journal of Cellular and Comparative Physiology*, vol. 7, no. 2, pp. 153-162, 1935.

[15] Chris Waltham, "An Early History of Heavy Water," Vancouver B.C., Canada, 1998.

[16] Doug Reilly, Norbert Ensslin, Hastings smith, Jr., Passive Nondestructive Assay of Nuclear Materials, S. Kreiner, Ed., Washington, DC: Office of Nuclear Regulatory Research. U. S. Nuclear Regulatory Commission, 1991.

[17] A. B. Lovins, "Nuclear weapons and power-reactor plutonium," *Nature,* vol. 283, no. 5750, p. 817–823, 1980.

[18] D. Brugge, "Uranium," in *Encyclopedia of Toxicology*, 3ed., P. Wexler, Ed., Academic Press, 2014, pp. 883-884.

[19] GlobalSecurity.org., "Uranium Isotopes," 5 February 2020. https://www.globalsecurity.org/wmd/intro/u-isotopes.htm.

[20] International Panel on Fissile Materials, "Global Fissile Material Report 2015: Nuclear Weapon and Fissile Material Stockpiles and Production," 2015.

[21] P. A. d. Groot, Ed., "Isotope Separation Methods," in *Handbook of Stable Isotope Analytical Techniques*, Elsevier, 2009, pp. 1025-1032.

[22] W. N. Association, "Uranium Enrichment," September 2020. https://www.world-nuclear.org/information-library/nuclear-fuel-cycle/conversion-enrichment-and-fabrication/uranium-enrichment.aspx.

[23] Philip Casey Durst, Scott Demuth, James Morgan, Brent McGinnis, Michael Whitaker, "Safeguards Guidance for Designers of Commercial Nuclear Facilities International Safeguards Requirements for Uranium Enrichment Plants," in *Northwest International Conference on Global Nuclear Security - The Decade Ahead*, 2010.

[24] A. Fishman, R. Frederickson, A. White, "Safeguarding enriched uranium at a centrifuge enrichment plant," *Nuclear Materials Management,* vol. 5, no. 3, pp. 425-437, 22 June 1976.

[25] International Atomic Energy Agency, IAEA Safeguards Glossary, 2001ed., Vienna: IAEA, 2002.

[26] Hideaki Ohgaki, Toshiteru Kii, Kai Masuda, Tsuyoshi Misawa, Cheol-Ho Pyeon, Ryoichi Hajima, Takehito Hayakawa, Toshiyuki Shizuma, Keigo Kawase, Masaki Kando, Hiroyuki Toyokawa, "Conceptual design of a nuclear material detection system based on the neutron/gamma-ray hybrid approach," in *IEEE International Conference on Technologies for Homeland Security (HST)*, 2010.

[27] Hideaki Ohgaki, Mohamed Omer, Hani Negm, Toshitada Hori, Toshiteru Kii, Kai Masuda, Tsuyoshi Misawa, Cheolho Pyeon, Ryoichi Hajima, Takehito Hayakawa, Toshiyuki Shizuma, Mamoru Fujiwara, Masaki Kando, Izuru Daito, Shinya Fujimoto, Fumio Sakai, Seong H. P., "Non-destructive inspection system for special nuclear material using inertial electrostatic confinement fusion neutrons and Laser Compton Scattering Gamma-rays," in *IEEE Conference on Technologies for Homeland Security (HST)*, 2012.

[28] William Bertozzi, Robert J. Ledoux, "Nuclear Resonance Fluorescence Imaging in Non-intrusive Cargo Inspection," 2005.

[29] Toshiyuki Shizuma, Takehito Hayakawa, Ryoichi Hajima, Nobuhiro Kikuzawa, Hideaki Ohgaki, Hiroyuki Toyokawa, "Nondestructive identification of isotopes using nuclear resonance fluorescence," *Review of Scientific Instruments*, vol. 83, p. 015103, 2012.

[30] J. R. Phillips, "Irradiated Fuel Measurements," in *Passive Nondestructive Assay of nuclear materials*, Vols. NUREG/CR-5550, D. Reilly, Ed., Washington, Office of Nuclear Regulatory Research, 1991, p. 556.

[31] European Nuclear Society, "Material Unaccounted For," 6 June 2019. https://www.euronuclear.org/glossary/muf/.

[32] Tobin Stephen J., Charlton William S., Fensin Michael L., Menlove Howard O., Hoover A. S., Quiter B. J., Rajasingam A., Swinhoe M. T., Thompson S. J., Charlton W. S., Ehinger M. H., Sandoval N. P., Saavedra S. F., Strohmeyer D., "Determining plutonium in spent fuel with nondestructive assay techniques," in *31st. Annual European Safeguards Research and Development Association (ESRADA) Meeting*, Vilnius, Lithuania, 2009.

[33] International Atomic Energy Agency, "Utilization of Accelerator Based Real Time Methods in Investigation of Materials with High Technological Importance," IAEA, Vienna, 2015.

[34] International Atomic Energy Agency, "Nuclear Forensics: Beyond the Science," IAEA, Vienna, 2020.

[35] Michael J. Kristo, "Nuclear Forensics," in *Handbook of Radioactivity Analysis Volume 2: Radioanalytical Applications*, vol. 2, Lawrence, 2018, p. 1:59.

[36] International Atomic Energy Agency, "Nuclear Forensics in Support of Investigations, IAEA Nuclear Security Series No. 2-G (Rev.1)," IAEA, VIENNA, 2015.

[37] Franz R. Metzger, "Resonance fluorescence in nuclei," *Progress in Nuclear Physics,* vol. 7, pp. 54-88, 1959.

[38] G. Breit, E. Wigner, "Capture of Slow Neutrons," *Physical Review Journals Archive,* vol. 49, no. 7, pp. 519-531, 1936.

[39] Vavrek Jayson R., Henderson Brian S., Danagoulian Areg, "Experimental demonstration of an isotope-sensitive warhead verification technique using nuclear resonance fluorescence,"

Proceedings of the National Academy of Sciences, vol. 115, no. 17, pp. 4363-4366, 2018.

[40] William Bertozzi, Robert J. Ledoux, "Nuclear resonance fluorescence imaging in non-intrusive cargo inspection," *Nuclear Instruments and Methods in Physics Research Section B: Beam Interactions with Materials and Atoms,* vol. 241, no. 1, pp. 820-825, 2005.

[41] Takehito Hayakawa, Hideaki Ohgaki, Toshiyuki Shizuma, Ryoichi Hajima, Nobuhiro Kikuzawa, Eisuke Minehara, Toshiteru Kii, Hiroyuki Toyokawa, "Nondestructive detection of hidden chemical compounds with laser Compton-scattering gamma rays," *Review of Scientific Instruments,* vol. 80, no. 4, p. 045110, 2009.

[42] Takehito Hayakawa, NobuhiroKikuzawa, RyoichiHajima, ToshiyukiShizuma, Nobuyuki Nishimori, MamoruFujiwara, MichioSeya, "Nondestructive assay of plutonium and minor actinide in spent fuel using nuclear resonance fluorescence with laser Compton scattering gamma-rays," *Nuclear Instruments and Methods in Physics Research A,* vol. 621, no. 1-3, pp. 695 - 700, 2010.

[43] J. Pruet, D. P. McNabb, C. A. Hagmann, F. V. Hartemann, C. P. J. Barty, "Detecting clandestine material with nuclear resonance fluorescence," *Journal of Applied Physics,* vol. 99, no. 12, p. 123102, 2006.

[44] Nobuhiro Kikuzawa, Ryoichi Hajima, Nobuyuki Nishimori, Eisuke Minehara, Takehito Hayakawa, Toshiyuki Shizuma, Hiroyuki Toyokawa, Hideaki Ohgaki, "Nondestructive Detection of Heavily Shielded Materials by Using Nuclear Resonance Fluorescence with a Laser-Compton Scattering γ-ray Source," *Applied Physics Express,* vol. 2, no. 3, pp. 1-3, 2009.

[45] O. Beck, T. Ruf, Y. Finkelstein, M. Cardona, T. R. Anthony, D. Belic, T. Eckert, D. Jäger, U. Kneissl, H. Maser, R. Moreh, A. Nord, H. H. Pitz, and A. Wolpert, "Nondestructive determination of the ^{13}C content in isotopic diamond by nuclear resonance fluorescence," *Journal of Applied Physics,* vol. 83, no. 10, p. 5484, 15 May 1998.

[46] Kenton J. Moody, Patrick M. Grant, Ian D. Hutcheon, Nuclear Forensic Analysis, 1ed., CRC Press, 2005.

[47] Jorge Eduardo Fernandez, Marcelo Rubio, David Bradley, "Radiation Physics and Chemistry," *The Journal for Radiation Physics, Radiation Chemistry and Radiation Processing,* vol. 154, no. 1, pp. 1-90, 2019.

[48] Hans Bichsel, Heinrich Schindler, "The Interaction of Radiation with Matter," in *Particle Physics Reference Library, Detectors for Particles and Radiation*, vol. 2, H. S. Christian W. Fabjan, Ed., Switzerland, Springer, 2020, p. 1083.

[49] David S. Chang, Foster D. Lasley, Indra J. Das, FAAPM, FACR, FASTRO, Marc S. Mendonca, Joseph R. Dynlacht, "Interactions of Electromagnetic Radiation with Matter," in *Basic Radiotherapy Physics and Biology*, Springer, Cham, 2014, pp. 35-41.

[50] Amin Al-Okour, "Radiation Physics: Radiation interaction with matter," *Materials Today: Proceedings,* 2021.

[51] Daniel R. McAlister, "Gamma Ray Attenuation Properties of Common Shielding Materials," PG Research Foundation, Inc. 1955 University Lane Lisle, IL 60532, USA, 2018.

[52] Walter Huda, Review of Radiologic Physics, 3ed., B. Brown, Ed., Lippincott Williams & Wilkins, a Wolters Kluwer business, 2009.

[53] Ervin B. Podgorsak, Radiation Physics for Medical Physicists, 2ed., Berlin, Heidelberg: Springer, 2006.

[54] M. H. McKetty, "The AAPM/RSNA physics tutorial for residents. X-ray attenuation," *RadioGraphics,* vol. 18, no. 1, pp. 145-150, 1998.

[55] M. J. Berger, J. H. Hubbell, S. M. Seltzer, J. Chang, J. S. Coursey, R. Sukumar, D. S. Zucker, K. Olsen, "XCOM: Photon Cross Sections Database," NIST Standard Reference Database 8, Washington, DC.

[56] Gabriel V. Turturica, Calin A. Ur, "Non-destructive techniques for material inspection with quasi-monoenergetic gamma beams," ELI – NP, Bucharest, 2020.

[57] Simon Cherry, James Sorenson, Michael Phelps, Physics in Nuclear Medicine, 4ed., Elsevier , 2012, p. 544.

[58] Paolo Russo, Handbook of X-ray Imaging, CRC Press Taylor & Francis Group, Boca Raton, FL, 2018, p. 1393.

[59] Takeshi Egami, Simon Billinge, Underneath the Bragg Peaks:Structural Analysis of Complex Materials, Pergamon: Elsevier, 2003.

[60] Albert Messiah, Quantum mechanics, Amsterdam: North-Holland Pub. Co.; New York : Interscience Publishers, 1961-62, 1961.

[61] Claude Leroy, Pier-Giorgio Rancoita, Principles of Radiation Interaction In Matter and Detection, 2ed., Singapore: World Scientific Publishing Co. Pte. Ltd., 2009, p. 950.

[62] Thomas S. Curry, James E. Dowdey, Robert C. Murry, Christensen's Physics of Diagnostic Radiology, 4ed., Lippincott Williams & Wilkins, 1990.

[63] Esam M. A. Hussein, Radiation Mechanics, Principles & Practice, 1ed., Oxford: Elsevier, 2007.

[64] Harvey A. Ziessman, Janis P. O'Malley, James H. Thrall, "Physics of Nuclear Medicine," in *Nuclear Medicine*, 3ed., J. P. O. J. H. T. Harvey A. Ziessman, Ed., Mosby, The Requisites in Radiology, 2006, pp. 20-33.

[65] Qiao Chen-Kai, Wei Jian-Wei, Chen Lin, "An Overview of the Compton Scattering Calculation," *Crystals*, vol. 11, no. 5, 2021.

[66] James E. Parks, "The Compton Effect-Compton Scattering and Gamma Ray Spectroscopy," Tennessee, 2015.

[67] O. Klein, Y. Nishina, "Über die Streuung von Strahlung durch freie Elektronen nach der neuen relativistischen Quantendynamik von Dirac," *Zeitschrift für Physik,* vol. 52, no. 11-12, pp. 853-868, 1929.

[68] Calin Alexandru Ur, "Gamma beam system at ELI − NP," in *AIP Conference Proceedings*, 2015.

[69] M. Schumacher, F. Smend, W. Mückenheim, P. Rullhusen, H. G. Börner, "Nuclear photoexcitation and delbrück scattering studied in the energy range 2–8 MeV," *Zeitschrift für Physik A Atoms and Nuclei,* vol. 300, pp. 193-203, June 1981.

[70] Lynn Kissel, R. H. Pratt, "Rayleigh Scattering Elastic Photon Scattering By Bound Electrons," in *Atomic Inner-Shell Physics*, 1ed., New York, Physics of Atoms and Molecules. Springer, Boston, MA., 1985, p. 465–532.

[71] Szu-yuan Chen, Anatoly Maksimchuk, Donald Umstadter, "Experimental observation of relativistic nonlinear Thomson scattering," *Nature,* vol. 396, no. 6712, pp. 653-655, 1998.

[72] M. Schumacher, P. Rullhusen, F. Smend, W. Mückenheim, H. G. Börner, "The energy dependence of Delbrück scattering investigated at $Z = 73, 82$ and 92," *Nuclear Physics A,* vol. 346, no. 3, pp. 418-430, 1980.

[73] Lynn Kissel, R. H. Pratt, "New Predictions for Rayleigh Scattering: 10 keV - 10 MeV," *Physical Review Letters,* vol. 40, no. 6, pp. 387-390, Feb. 1978.

[74] W. R. Johnson, Kwok-tsang Cheng, "Elastic scattering of 0.1–1 MeV photons," *Physical Review,* vol. 13, no. 2, pp. 692-698, 1976.

[75] L. Kissel, B. Zhou, S. C. Roy, S. K. Sen Gupta, R. H. Pratt, "The validity of form-factor, modified-form-factor and anomalous-scattering-factor approximations in elastic scattering calculations," *Acta Crystallographica Section A, Foundations and Advances,* vol. A51, pp. 271-288, 1995.

[76] J. H. Hubbell, W. J. Veigele, E. A. Briggs, R. T. Brown, D. T. Cromer, "Atomic form factors, incoherent scattering functions, and photon scattering cross sections," *Journal of Physical and Chemical Reference Data,* vol. 4, no. 3, 1975.

[77] J. H. Hubbell, I. O/verbo/, "Relativistic atomic form factors and photon coherent scattering cross sections," *Journal of Physical and Chemical Reference Data,* vol. 8, no. 1, p. 69, 1979.

[78] Lynn Kissel, "RTAB: the Rayleigh scattering database," *Radiation Physics and Chemistry,* vol. 59, no. 2, pp. 185-200, 2000.

[79] P. Rullhusen, W. Mückenheim, F. Smend, M. Schumacher, G. P. A. Berg, K. Mork, Lynn Kissel, "Test of vacuum polarization by precise investigation of Delbruck scattering," *Physical Review C,* vol. 23, no. 4, pp. 1375-1383, 1981.

[80] Martin Schumacher, "Delbrück scattering," *Radiation Physics and Chemistry,* vol. 56, no. 1-2, pp. 101-111, 1999.

[81] H. Falkenberg, A. Hünger, P. Rullhusen, M. Schumacher, A. I. Milstein, K. Mork, "Amplitudes for Delbrück scattering," *Atomic Data and Nuclear Data Tables,* vol. 50, no. 1, pp. 1-27, 1992.

[82] A. Scherdin, A. Schäfer, W. Greiner, G. Soff, P. J. Mohr, "Coulomb corrections to Delbrueck scattering," *Zeitschrift fuer Physik. A, Hadrons and Nuclei,* vol. 353, no. 3, pp. 273-277, September 1995.

[83] Alexander Scherdin, Andreas Schäfer, Walter Greiner, Gerhard Soff, "Delbrück scattering in a strong external field," *Phys. Rev. D,* vol. 45, no. 8, pp. 2982-2987, 1992.

[84] P. Rullhusen, U. Zurmühl, F. Smend, M. Schumacher, H. G. Börner, and S. A. Kerr, "Giant dipole resonance and Coulomb correction effect in Delbrück scattering studied by elastic and Raman scattering of 8.5 to 11.4 MeV photons," *Physical Review C,* vol. 27, no. 2, pp. 559-568, 1983.

[85] B. Kasten, D. Schaupp, P. Rullhusen, F. Smend, M. Schumacher, Lynn Kissel, "Coulomb correction effect in Delbrück scattering and atomic Rayleigh scattering of 1– 4 MeV photons," *Physical Review C,* vol. 33, no. 5, pp. 1606-1615, 1986.

[86] P. Rullhusen, W. Mückenheim, F. Smend, M. Schumacher, G. P. A. Berg, K. Mork, Lynn Kissel, "Test of vacuum polarization by precise

investigation of Delbrück scattering," *Physical Review C,* vol. 23, no. 4, pp. 1375--1383, 1981.

[87] V. A. Plujko, R. Capote, O. M. Gorbachenko, "Giant dipole resonance parameters with uncertainties from photonuclear cross sections," *Atomic Data and Nuclear Data Tables,* vol. 97, no. 5, pp. 567-585, 2011.

[88] R. Capote, M. Herman, P. Obložinský, P. G. Young, S. Goriely, T. Belgya, A. V. Ignatyuk, A. J. Koning, S. Hilaire, V. A. Plujko, M. Avrigeanu, O. Bersillon, M. B. Chadwick, T. Fukahori, Zhigang Ge, Yinlu Han, S. Kailas, J. Kopecky, V. M. Maslov, et al., "RIPL – Reference Input Parameter Library for Calculation of Nuclear Reactions and Nuclear Data Evaluations," *Nuclear Data Sheets,* vol. 110, no. 12, pp. 3107-3214, 2009.

[89] E. G. Fuller, Evans Hayward, "The nuclear photoeffect in holmium and erbium," *Nuclear Physics,* vol. 30, pp. 613-635, 1962.

[90] U. Kneissl, H. H. Pitz, A. Zilges, "Investigation of nuclear structure by resonance fluorescence scattering," *Progress in Particle and Nuclear Physics,* vol. 37, pp. 349-433, 16 February 1996.

[91] Donald R. Hamilton, "On Directional Correlation of Successive Quanta," *Physical Review Journals Archive,* vol. 58, no. 2, pp. 122-131, 15 July 1940.

[92] Lawrence W. Fagg, Stanley S. Hanna, "Polarization Measurements on Nuclear Gamma Rays," *Reviews of Modern Physics,* vol. 31, no. 3, pp. 711-758, July 1959.

[93] Kai Siegbahn, Alpha-, beta- and gamma-ray spectroscopy. vol. 2, vol. 1, Amsterdam: North-Holland, 1965.

[94] A. H. Wapstra, Nuclear spectroscopy tables, Amsterdam: North-Holland Pub. Co, 1959.

[95] B. Özel, J. Enders, P. von Neumann-Cosel, I. Poltoratska, A. Richter, D. Savran, S. Volz, A. Zilges, "Systematics of the pygmy dipole resonance in stable tin isotopes from resonant photon scattering," *Nuclear Physics A,* vol. 788, no. 1-4, pp. 385-388, 2007.

[96] F. Ajzenberg-Selove, "Energy levels of light nuclei $A = 11 - 12$," *Nuclear Physics .A,* vol. 506, pp. 1-158, 1990.

[97] Stanley G. Prussin, Nuclear Physics for Applications: A Model Approach, Berkeley, California: Wiley-VCH Verlag GmbH & Co. KGaA, Weinheim, 2007.

[98] Samuel A. M. Wong, Introductory Nuclear Physics, 2ed., Wiley-VCH Verlag GmbH & Co. KGaA, 2004.

[99] W. Donner, W. Greiner, "Octupole vibrations of deformed nuclei," *Zeitschrift für Physik,* vol. 197, no. 5, pp. 440-472, 1966.

[100] U E P Berg, U Kneissl, "Recent Progress on Nuclear Magnetic Dipole Excitations," *Annual Review of Nuclear and Particle Science,* vol. 37, pp. 33-69, 1987.

[101] J. Bryssinck, L. Govor, V. Yu. Ponomarev, F.Bauwens, O. Beck, D. Belic, D. De Frenne, T. Eckert, C. Fransen, K. Govaert, R. -D. Herzberg, E. Jacobs, U. Kneissl, H. Maser, A. Nord, N. Pietralla, H. H. Pitz, V. Werner, "Systematic study of electric quadrupole excitations in the stable even mass Sn nuclei," *Physical Review C,* vol. 61, no. 2, p. 024309, 2000.

[102] J. Bryssinck, L. Govor, D. Belic, F. Bauwens, O. Beck, P. von Brentano, D. de Frenne, T. Eckert, C. Fransen, K. Govaert, R. -D. Herzberg, E. Jacobs, U. Kneissl, H. Maser, A. Nord, N. Pietralla, H. H. Pitz, V. Yu. Ponomarev, V. Werner, "Uniform properties of $J^{\pi} = 1^{-}$ two-phonon states in the semimagic even-even tin isotopes $^{116, 118, 120, 122, 124}$Sn," *Physical Review C,* vol. 59, no. 4, pp. 1930-1934, 1999.

[103] B. A. Brown, P. M. S. Lesser, D. B. Fossan, "Properties of high-spin states in Nb-91 and Zr-91 via Li-91 induced reactions," *Physical Review C,* vol. 13, no. 5, pp. 1900-1921, 1976.

[104] D. R. Tilley, J. H. Kelley, J. L. Godwin, D. J. Millener, J. E. Purcell, C. G. heu, H. R. Weller, "Energy levels of light nuclei $A = 8, 9, 10$," *Nuclear Physics A,* vol. 745, no. 3, pp. 155-362, 2004.

[105] P. Oblozinsky, P. Dimitriou, S. Goriely, Xu Ruirui, Tian Yuan, M. Krticka, R. Schwengner, T. Belgya, N. Iwamoto, H. Utsunomiya, Y. S. Cho, J. Kopecky, S. Siem, R. B. Firestone, T. Kawano, D. M. Filipescu, V. V. Varlamov, V. Plujko, "IAEA Evaluated Photonuclear Data Library (IAEA/PD-2019)," International Atomic Energy Agency, 2020. https://www-nds.iaea.org/photonuclear/pdfilelist.html.

[106] J. M. Blatt, V. F. Weisskopf, Theoretical Nuclear Physics, New York: John Wiley & Sons, 1952.

[107] J. Enders, P. von Brentano, J. Eberth, A. Fitzler, C. Fransen, R.-D. Herzberg, H. Kaiser, L. Käubler, P. von Neumann-Cosel, N. Pietralla, V.Yu. Ponomarev, A. Richter, R. Schwengner, I. Wiedenhöver, "Nuclear resonance fluorescence experiments on $^{204, 206, 207, 208}$Pb up to 6.75 MeV," *Nuclear Physics A,* vol. 724, no. 3-4, pp. 243-273, 2003.

[108] E. Hammar\'en, P. Heikkinen, K. W. Schmid, Amand Faessler, "Microscopic and phenomenological analysis of the Alaga rule for dipole states," *Nuclear Physics A,* vol. 541, pp. 226-240, 1992.

[109] Kenneth S. Krane, Introductory Nuclear Physics, 2ed., New York: John Wiley & Sons, Inc., 1987, p. 864.

[110] Warren, Glen A. and Detwiler, Rebecca S. and Peplowski, Patrick N., "Applications of nuclear resonance fluorescence," in *Nuclear Science Symposuim, Medical Imaging Conference*, Knoxville, TN, USA, 2010.

[111] Glen Warren, Jac Caggiano, Patrick Peplowski, "Potential Applications of Nuclear Resonance Fluorescence," in *International Conference on Applications of Nuclear Techniques*, 2009.

[112] Jake J. Hecla, Areg Danagoulian, "Nuclear disarmament verification via resonant phenomena," *Nature Communications,* vol. 9, no. 1, p. 1259, 2018.

[113] L. E. Smith, A. Dougan, S. Tobin, B. Cipiti, M. Ehinger, A. Bakel, R. Bean, J. W. Grate, P. Santi, S. Bryan, M. Kinlaw, J. Schwantes, T. Burr, S. Lehn, K. Tolk, D. Chichester, H. Menlove, D. Vo, D. Duckworth, P. Merkle, T. F. Wang, F. Duran, et al., "AFCI Safeguards Enhancement Study: Technology Development Roadmap," Pacific Northwest National Laboratory (PNNL), Richland, Washington, 2008.

[114] Stephen J. Tobin, Peter Jansson, "Nondestructive assay options for spent fuel encapsulation," Svensk Kärnbränslehantering AB Swedish Nuclear Fuel and Waste Management Co, Stockholm, 2013.

[115] Alan Michael Bolind, Michio Seya, "The State of the Art of the Nondestructive Assay of Spent Nuclear Fuel Assemblies- A Critical

Review of the Spent Fuel NDA Project of the U.S. Department of Energy's Next Generation Safeguards Initiative," JAEA, 2015.

[116] G. A. Warren, P. N. Peplowski, J. A. Caggiano, "Potential National Security Applications of Nuclear Resonance Fluorescence Methods," Pacific Northwest National Laboratory, Springfield, 2009.

[117] William Bertozzi, Stephen E. Korbly, Robert J. Ledoux, William Park, "Nuclear resonance fluorescence and effective Z determination applied to detection and imaging of special nuclear material, explosives, toxic substances and contraband," *Nuclear Instruments and Methods in Physics Research Section B: Beam Interactions with Materials and Atoms,* vol. 261, no. 1-2, pp. 331-336, 17 April 2007.

[118] G. V. Turturica, V. Iancu, A. Pappalardo, P. -A. Söderström, E. Açıksöz, D. L. Balabanski, L. Capponi, P. Constantin, V. Fugaru, G. L. Guardo, M. Ilie, S. Ilie, M. Iovea, D. Lattuada, D. Nichita, T. Petruse, A. Spataru, C. A. Ur, "Effective Z evaluation using monoenergetic gamma rays and neural networks," *The European Physical Journal Plus,* vol. 135, no. 2, p. 140, 28 January 2020.

[119] Y. Liu, B. D. Sowerby, J. R. Tickner, "Comparison of neutron and high-energy X-ray dual-beam radiography for air cargo inspection," *Applied Radiation and Isotopes,* vol. 66, no. 4, pp. 463-473, 2008.

[120] Rogers Thomas W., Jaccard Nicolas, Protonotarios Emmanouil D. Ollier James, Morton Edward J., Griffin Lewis D., "Threat Image Projection (TIP) into X-ray images of cargo containers for training humans and machines," in *IEEE International Carnahan Conference on Security Technology (ICCST)*, Orlando, FL, USA, 2016.

[121] Thomas W. Rogers, Nicolas Jaccarda, Edward J. Morton, Lewis D. Griffin, "Automated X-ray image analysis for cargo security: Critical review and future promise," *Journal of x-Ray Science and Technology,* vol. 25, pp. 33-56, 2017.

[122] S. Ogorodnikov, V. Petrunin, "Processing of interlaced images in 4–10 MeV dual energy customs system for material recognition," *Physical Review Accelerators and Beams,* vol. 5, no. 10, p. 104701, 8 October 2002.

[123] Bernhard A. Ludewigt, Brian J. Quiter, Scott D. Ambers, "Nuclear Resonance Fluorescence for Safeguards Applications," 2011.

[124] Ryoichi Hajima, Takehito Hayakawa, Nobuhiro Kikuzawa, Eisuke Minehara, "Proposal of Nondestructive Radionuclide Assay Using a High-Flux Gamma-Ray Source and Nuclear Resonance Fluorescence," *Journal of Nuclear Science and Technology,* vol. 45, no. 5, pp. 441-451, 2008.

[125] Toshiyuki Shizuma, Takehito Hayakawa, Christopher T. Angell, Ryoichi Hajima, Futoshi Minato, Kenya Suyama, Michio Seya, Micah S. Johnson, Dennis P. McNabb, "Statistical uncertainties of nondestructive assay for spent nuclear fuel by using nuclear resonance fluorescence," *Nuclear Instruments and Methods in Physics Research Section A: Accelerators, Spectrometers, Detectors and Associated Equipment,* vol. 737, pp. 170-175, 2014.

[126] Hiroyuki Toyokawa, Hideaki Ohgaki, Takehito Hayakawa, Toshiteru Kii, Toshiyuki Shizuma, Ryoichi Hajima, Nobuhiro Kikuzawa, Kai Masuda, Fumito Kitatani, Hideo Harada, "Two-Dimensional Isotope Imaging of Radiation Shielded Materials Using Nuclear Resonance Fluorescence," *Japanese Journal of Applied Physics,* vol. 50, no. 10R, p. 100209, 2011.

[127] Heishun Zen, Hideaki Ohgaki, Yoshitaka Taira, Takehito Hayakawa, Toshiyuki Shizuma, Izuru Daito, Jun-ichiro Yamazaki, Toshiteru Kii, Hiroyuki Toyokawa, Masahiro Katoh, "Demonstration of tomographic imaging of isotope distribution by nuclear resonance fluorescence," *AIP Advances,* vol. 9, no. 035101, pp. 1-7, 2019.

[128] C. A. Hagmann, J. M. Hall, M. S. Johnson, D. P. McNabb, J. H. Kelley, C. Huibregtse, E. Kwan, G. Rusev, A. P. Tonchev, "Transmission-based detection of nuclides with nuclear resonance fluorescence using a quasimonoenergetic photon source," *Journal of Applied Physics,* vol. 106, no. 084901, pp. 1-7, 2009.

[129] B. J. Quiter, B. A. Ludewigt, V. V. Mozin, C. Wilson, S. Korbly, "Transmission nuclear resonance fluorescence measurements of 238U in thick targets," *Nuclear Instruments and Methods in Physics Research Section B: Beam Interactions with Materials and Atoms,* vol. 269, no. 10, pp. 1130-1139, 2011.

[130] C. T. Angell, R. Hajima, T. Hayakawa, T. Shizuma, H. J. Karwowski, J. Silano, "Demonstration of a transmission nuclear resonance fluorescence measurement for a realistic radioactive waste canister scenario," *Nuclear Instruments and Methods in Physics Research Section B: Beam Interactions with Materials and Atoms,* vol. 347, pp. 11-19, 2015.

[131] C. T. Angell, "Enabling in situ thermometry using transmission nuclear resonance fluorescence," *Nuclear Instruments and Methods in Physics Research Section B: Beam Interactions with Materials and Atoms,* vol. 368, pp. 9-14, 2016.

[132] Thomas A. Holly, Brian G. Abbott, Mouaz Al-Mallah, Dennis A. Calnon, Mylan C. Cohen, Frank P. DiFilippo, Edward P. Ficaro,

Michael R. Freeman, Robert C. Hendel, Diwakar Jain, Scott M. Leonard, Kenneth J. Nichols, Donna M. Polk, Prem Soman, "Single photon-emission computed tomography," *Journal of Nuclear Cardiology,* vol. 17, no. 5, pp. 941-973, 2010.

[133] H. E. Martz, D. J. Schneberk, G. P. Roberson, S. G. Azevedo, S. K. Lynch, "Computerized Tomography of High Explosives," in *Nondestructive Characterization of Materials IV*, 1ed., J. F. B. R. E. G. Clayton O. Ruud, Ed., Boston, MA, Springer US, p. 187–195.

[134] Sameer Singh, Maneesha Singh, "Explosives detection systems (EDS) for aviation security," *Signal Processing,* vol. 83, no. 1, pp. 31-55, 2003.

[135] Andrea Mouton, Toby Breckon, "A review of automated image understanding within 3D baggage computed tomography security screening," *Journal of X-Ray Science and Technology,* vol. 23, no. 5, pp. 531-555, 2015.

[136] L. R. Fredrick, "The evolution of computed tomography (CT) as an explosives detection modality," in *In Proceedings of the First International Symposium on Explosive Detection Technology, Federal Aviation Administration*, Technical Center. Atlantic City, NJ, 1991.

[137] Jongbum Kim, Sunghee Jung, Jinho Moon, Taekyong Kwon, Gyuseong Cho, "Monte Carlo Simulation for the Design of Industrial Gamma-ray Transmission Tomography," *Progress in Nuclear Science and TECHNOLOGY,* vol. 1, pp. 263-266, 2011.

[138] Nicolas Estre, Daniel Eck, Jean-Luc Pettier, Emmanuel Payan, Christophe Roure, Eric Simon, "High-Energy X-Ray Imaging Applied

to Nondestructive Characterization of Large Nuclear Waste Drums," *IEEE Transactions on Nuclear Science,* vol. 62, no. 6, pp. 3104 - 3109, 2015.

[139] Hiroyuki Toyokawa, Hideaki Ohgaki, Tomohisa Mikado, and Kawakatsu Yamada, "High-energy photon radiography system using laser-Compton scattering for inspection of bulk materials," *Review of Scientific Instruments,* vol. 73, no. 9, 22 August 2002.

[140] W. Bertozzi, R. J. Ledoux, "Methods and Systemic For Computer Tomography of Nuclear Isotopes Using Nuclear Resonance Fluorescence," U.S. Patent 8,180,019 B2, 2012.

[141] C. P. Barty, F. Albert, S. G. Anderson, P. Armstrong, A. Bayramian, G. Beer, R. Cross, C. A. Ebbers, G. Deis, D. J. Gibson, J. Hall, F. V. Hartemann, T. Houck, R. A. Marsh, M. J. Messerly, H. Phan, V. A. Semenov, S. S. Wu, "Overview of MEGa-ray-based Nuclear Materials Management Activities at the Lawrence Livermore National Laboratory," in *2nd Annual Meeting, Palm Desert,*, Palm Desert, CA, United States, 2011.

[142] Ryoichi Hajima, Takehito Hayakawa, Nobuhiro Kikuzawa, Eisuke Minehara, "Proposal of Nondestructive Radionuclide Assay Using a High-Flux Gamma-Ray Source and Nuclear Resonance Fluorescence," *Journal of Nuclear Science and Technology,* vol. 45, no. 5, pp. 441-451, 2008.

[143] Estre Nicolas, Eck Daniel, Pettier Jean-Luc, Payan Emmanuel, Roure Christophe, Simon Eric, "High-Energy X-Ray Imaging Applied to Nondestructive Characterization of Large Nuclear Waste Drums," *IEEE Transactions on Nuclear Science,* vol. 62, no. 6, pp. 3104-3109, 2015.

[144] H. Ohgaki, S. Sugiyama, T. Yamazaki, T. Mikado, M. Chiwaki, K. Yamada, R. Suzuki, T. Noguchi, T. Tomimasu , "Measurement of laser-induced Compton backscattered photons with anti-Compton spectrometer," *IEEE Transactions on Nuclear Science,* vol. 38, no. 2, pp. 386-392, 1991.

[145] Hideaki Ohgaki, Hiroyuki Toyokawa, Katsuhisa Kudo, Naoto Takeda, Tetsuo Yamazaki, "Generation and application of Laser-Compton gamma-ray at ETL," *Nuclear Instruments and Methods in Physics Research Section A: Accelerators, Spectrometers, Detectors and Associated Equipment,* vol. 455, no. 1, pp. 54-59, 2000.

[146] H. Ohgaki, I. Daito, T. Kii, H. Zen, T. Hayakawa, T. Shizuma, M. Katoh, J. Yamazaki, Y. Taira, H. Toyokawa, "Study on NRF – CT Imaging by Laser Compton Backscattering Gamma-rays in UVSOR," in *International Particle Accelerator Conference (7th)*, 2016.

[147] F. R. Arutyunian, V. A. Tumanian, "The Compton effect on relativistic electrons and the possibility of obtaining high energy beams," *Physics Letters,* vol. 4, no. 3, pp. 176-178, 1963.

[148] M. Adachi, H. Zen, T. Konomi, J. Yamazaki, K. Hayashi, M. Katoh, "Design and Construction of UVSOR – III ," in 11th International Conference on Synchrotron Radiation Instrumentation (SRI 2012), Journal of Physics: Conference Series, 2013.

[149] Richard H. Milburn, "Electron Scattering by an Intense Polarized Photon Field," *Physical Review Letters,* vol. 10, no. 3, pp. 75-77, February 1963.

[150] H. Ohgaki, T. Noguchi, S. Sugiyama, T. Yamazaki, T. Mikado, M. Chiwaki, K. Yamada, R. Suzuki, N. Sei, "Linearly polarized photons from Compton backscattering of laser-light for nuclear resonance fluorescence experiments," *Nuclear Instruments and Methods in Physics Research Section A, Accelerators, Spectrometers, Detectors and Associated Equipment*, vol. 353, no. 1-3, pp. 384-388, December 1994.

[151] Henry R. Weller, Mohammad W. Ahmed, Haiyan Gao, Werner Tornow, Ying K. Wu, Moshe Gai, Rory Miskimen, "Research opportunities at the upgraded HIγS facility," *Progress in Particle and Nuclear Physics*, vol. 62, no. 1, pp. 257-303, 2009.

[152] O. F Kulikov, Y. Y Telnov, E. I Filippov, M. N Yakimenko, "Compton effect on moving electrons," *Physics Letters*, vol. 13, no. 4, pp. 344-346, 1964.

[153] R. Klein, P. Kuske, R. Thornagel, G. Brandt, R. Görgen, G. Ulm, "Measurement of the BESSY II electron beam energy by Compton-backscattering of laser photons," *Nuclear Instruments and Methods in Physics Research Section A: Accelerators, Spectrometers, Detectors and Associated Equipment*, vol. 486, no. 3, pp. 545-551, 2002.

[154] K. Aoki, K. Hosono, T. Hadame, H. Munenaga, K. Kinoshita, M. Toda, S. Amano, S. Miyamoto, T. Mochizuki, M. Aoki, D. Li, "High-energy photon beam production with laser-Compton backscattering," *Nuclear Instruments and Methods in Physics Research Section A: Accelerators, Spectrometers, Detectors and Associated Equipment*, vol. 516, no. 2-3, pp. 228-236, 2004.

[155] Sho Amano, Ken Horikawa, Kazuki Ishihara, Shuji Miyamoto, Takehito Hayakawa, Toshiyuki Shizuma, Takayasu Mochizuki,

"Several-MeV γ-ray generation at NewSUBARU by laser Compton backscattering," *Nuclear Instruments and Methods in Physics Research Section A: Accelerators, Spectrometers, Detectors and Associated Equipment,* vol. 602, no. 2, pp. 337-341, 2009.

[156] T. Kaneyasu, Y. Takabayashi, Y. Iwasaki, S. Koda, "Generation of laser Compton gamma-rays in the SAGA light source storage ring," *Nuclear Instruments and Methods in Physics Research Section A: Accelerators, Spectrometers, Detectors and Associated Equipment,* vol. 659, no. 1, pp. 30-35, 2011.

[157] K. Kawase, Y. Arimoto, M. Fujiwara, S. Okajima, M. Shoji, S. Suzuki, K. Tamura, T. Yorita, H. Ohkuma, "MeV γ-ray generation from backward Compton scattering at SPring-8," *Nuclear Instruments and Methods in Physics Research Section A: Accelerators, Spectrometers, Detectors and Associated Equipment,* vol. 592, no. 3, pp. 154-161, 2008.

[158] D. Nutarelli, M. E. Couprie, L. Nahon, R. Bakker, A. Delboulbe, R. Roux, B. Visentin, M. Billardon, "Gamma rays production by intra-cavity Compton Back Scattering with Super-ACO Storage Ring Free Electron Laser," *Nuclear Instruments and Methods in Physics Research Section A: Accelerators, Spectrometers, Detectors and Associated Equipment,* vol. 407, no. 1-3, pp. 459-463, 1998.

[159] Vladimir N. Litvinenko, "Recent results with the high intensity γ-ray facility," Nuclear Instruments and Methods in Physics Research Section A: Accelerators, Spectrometers, Detectors and Associated Equipment, vol. 507, no. 1-2, pp. 527-536, 2003.

[160] M. Hosaka, H. Hama, K. Kimura, J. Yamazaki, T. Kinoshita, "Observation of intracavity Compton backscattering of the UVSOR free

electron laser," *Nuclear Instruments and Methods in Physics Research Section A: Accelerators, Spectrometers, Detectors and Associated Equipment,* vol. 393, no. 1-3, pp. 525-529, 1997.

[161] Kii Toshiteru, Masuda Kai, Ohgaki Hideaki, Harada Hideo, Kitatani Fumito, Hayakawa Takehito, Shizuma Toshiyuki, Kikuzawa Nobuhiro, Hajima Ryoichi, Nishimori Nobuyuki, Toyokawa Hiroyuki, "Performance of the $LaBr_3$(Ce) scintillator for nuclear resonance fluorescence experiment," in *IEEE Nuclear Science Symposium Conference Record (NSS/MIC)*, Orlando, 2009.

[162] H. Yang, D. K. Wehe, "Detection of concealed Special Nuclear Material using Nuclear Resonance Fluorescence technique," in *IEEE Nuclear Science Symposium Conference Record (NSS/MIC*, Orlando, FL, USA, 2009.

[163] V. N. Litvinenko, B. Burnham, M. Emamian, N. Hower, J. M. J. Madey, P. Morcombe, P. G. O'Shea, S. H. Park, Sachtschale, R. Straub, G. K. D. Swift, P. Wang, Y. Wu, R. S. Canon, C. R. Howell, Roberson, N. R. Roberson, E. C. Schreiber, M. Spraker, et al.,, "Gamma-Ray Production in a Storage Ring Free-Electron Laser," *Physical Review Letters,* vol. 78, no. 24, pp. 4569-4572, 1997.

[164] Phillip M. Rinard, "Application Guide to Shufflers," Los Alamos National Laboratory, Los Alamos, New Mexico, 2001.

[165] Shuji Miyamoto, Yoshihiko Shoji, Sho Amano, Ken Horikawa, Yoshiki Hidaka, Ainosuke Ando, Takayasu Mochizuki, Dazhi Li, Kazuo Imasaki, Kazuhiko Aoki, Yoshihiro Asano, Tetsuya Takagi, "Laser Compton back-scattering gamma-ray source on NewSUBARU," in *2nd Annual Meeting of Particle Accelerator Society of Japan*, Tosu, Japan, 2005.

[166] The ELI-Nuclear Physics working groups, "The White Book of ELI Nuclear Physics Bucharest-Magurele, Romania," Andreas Thoss, 2011.

[167] " BL1U ," UVSOR – III Synchrotron Facility, Institute for Molecular Science, National Institutes of Natural Sciences, [Accessed 22 June 2021].
https://www.uvsor.ims.ac.jp/beamlines/1U/ebl1u.html.

[168] Khaled Ali, Hideaki Ohgaki, Heishun Zen, Toshiteru Kii, Takehito Hayakawa, Toshiyuki Shizuma, Hiroyuki Toyokawa, YoshitakaTaira, Violeta Iancu, Gabriel Turturica, Călin Alexandru Ur, Masaki Fujimoto, Masahiro Katoh, "Experimental Demonstration of Selective Isotope CT-Imaging Based on Nuclear Resonance Fluorescence Absorption Method," in *IEEE Nuclear Science Symposium and Medical Imaging Conference (NSS/MIC)*, Manchester, UK, 2019.

[169] Thomas Flohr, "CT Systems," *Current Radiology Reports,* vol. 1, no. 1, pp. 52-63, 2013.

[170] Toshio Suzuki, "General formulae of luminosity for various types of colliding beam machines," KEK--76-3, Oho, Ibaraki, 1976.

[171] Heishun Zen, Yoshitaka Taira, Taro Konomi, Takehito Hayakawa, Toshiyuki Shizuma, Junichiro Yamazaki, Toshiteru Kii, Hiroyuki Toyokawa, Masahiro Katoh, Hideaki Ohgaki, "Generation of High Energy Gamma-ray by Laser Compton Scattering of 1.94-μm Fiber Laser in UVSOR – III Electron Storage Ring," *Energy Procedia,* vol. 89, pp. 335-345, 2016.

[172] Hideo Hirayama, Yoshihito Namito, Alex F. Bielajew, Scott J. Wilderman, Walter R. Nelson,, "The EGS5 code system," SLAC Report

number: SLAC-R-730 and KEK Report number: 2005-8, Ibaraki-ken, 2005.

[173] Khaled Ali, Hideaki Ohgaki, Heishun Zen, Toshiteru Kii, Takehito Hayakawa, Toshiyuki Shizuma, Hiroyuki Toyokawa, Yoshitaka Taira, Violeta Iancu, Gabriel Turturica, Călin Alexandru Ur, Masaki Fujimoto, Masahiro Katoh, "Selective Isotope CT Imaging Based on Nuclear Resonance Fluorescence Transmission Method," *IEEE Transactions on Nuclear Science,* vol. 67, no. 8, pp. 1976-1984, 2020.

[174] Glenn F. Knoll, Radiation Detectibn and Measurement, 3ed., vol. 65, New York: John Wiley & Sons, Inc, 2000, pp. 757-771.

[175] Mikhail Korzhik, Gintautas Tamulaitis, Andrey N. Vasil'ev, Physics of Fast Processes in Scintillators, Cham, Switzerland: Springer Nature Switzerland AG, 2020.

[176] Li Sangang, Cheng Yi, Wang Lei, Yang Li, Liu Huan, Liao Jiawei, Zeng Liyang, Luo Yong, Wang Xiaoyu, Pei Qiuyan & Wang Jie, "The Effect of Intrinsic Radiation from a 3 × 3-in. $LaBr_3$(Ce) Scintillation Detector on In Situ Artificial Radiation Measurements," *Nuclear Technology,* vol. 204, no. 2, pp. 195-202, 2018.

[177] Hani Negm, Izuru Daito, Heishun Zen, Toshiteru Kii, Kai Masuda, Toshitada Hori, Hideaki Ohgaki, Ryoichi Hajima, Toshiyuki Shizuma, Takehito Hayakawa, Nobuhiro Kikuzawa, Hiroyuki Toyokawa, "A Study of the Nuclear Resonance Fluorescence Reaction Yield Dependence on the Target Thickness of ^{208}Pb," *Nuclear Physics and Gamma-Ray Sources for Nuclear Security and Nonproliferation,* pp. 291-299, 2014.

[178] I. Daito, H. Ohgaki, G. Suliman, V. Iancu, C.A. Ur, M. Iovea, "Simulation Study on Computer Tomography Imaging of Nuclear Distribution by Quasi Monoenergetic Gamma Rays with Nuclear Resonance Fluorescence: Case Study for ELI − NP Application," *Energy Procedia,* vol. 394, p. 389, 2016.

[179] M. Goto, Andrei Gheata, O. Couet, I. Antcheva, B. Bellenot, V. Onoutchin, G. Ganis, M. Ballintijn, V. Fine, V. Perevoztchikov, N. Buncic, S. Panacek, A. Naumann, A. Kreshuk, R. Maunder, T. Pocheptsov. S. Linev, S. Roiser, L. Moneta, W. Lavrijsen, Root Data Analysis Framework, Geneva: Rene Brun & Fons Rademakers, 2018.

[180] Richard Gordon, Robert Bender, Gabor T. Herman, "Algebraic Reconstruction Techniques (ART) for three-dimensional electron microscopy and X-ray photography," *Journal of Theoretical Biology,* vol. 29, no. 3, pp. 471-5193, 1970.

[181] Takuso Sato, Stephen J. Norton, Melvin Linzer, Osamu Ikeda, Makoto Hirama, "Tomographic image reconstruction from limited projections using iterative revisions in image and transform spaces," *Applied Optics,* vol. 20, no. 3, pp. 395-399, 1981.

[182] Johan Nuyts, Bruno De Man, Jeffrey A Fessler, Wojciech Zijewski, Freek J Beekman, "Modelling the physics in the iterative reconstruction for transmission computed tomography," *Physics in Medicine & Biology,* vol. 58, no. 12, p. 63, 2013.

[183] P. M. Endt, "Energy levels of $A = 21-44$ nuclei (VII)," *Nuclear Physics A,* vol. 521, pp. 1-400, 15 May 1990.

[184] AVS. LTD AVS/Express, "General Purpose Visualization Software.," Copyright © 2022 Cybernet Systems CO., LTD., 2022. https://www.cybernet.co.jp/avs/sitemap.html.

[185] Khaled Ali, Heishun Zen, Hideaki Ohgaki, Toshiteru Kii, Takehito Hayakawa, Toshiyuki Shizuma, Hiroyuki Toyokawa, Masaki Fujimoto, Yoshitaka Taira, Masahiro Katoh, "Three-Dimensional Nondestructive Isotope-Selective Tomographic Imaging of ^{208}Pb Distribution via Nuclear Resonance Fluorescence," *Applied Sciences,* vol. 11, no. 8, 2021.

[186] K. P. Ziock, "Principles and applications of gamma-ray imaging for arms control," Nuclear Instruments and Methods in Physics Research Section A: Accelerators, Spectrometers, Detectors and Associated Equipment, vol. 878, pp. 191-199, 2018.

[187] Julio Diaz, Taeil Kim, Victor Petrov, Annalisa Manera, "X-ray and gamma-ray tomographic imaging of fuel relocation inside sodium fast reactor test assemblies during severe accidents," *Journal of Nuclear Materials,* vol. 543, 2 October 2020.

[188] Christopher G. Wahl, Willy R. Kaye, Weiyi Wang, Feng Zhang, Jason M. Jaworski, Alexis King, Y. Andy Boucher, Zhong He, "The Polaris-H imaging spectrometer," *Nuclear Instruments and Methods in Physics Research Section A: Accelerators, Spectrometers, Detectors and Associated Equipment,* vol. 784, pp. 377-381, 2015.

[189] Tai Pham Duc, Ryouichi Nakamura, "Fused visualization of 3D Ultrasound and CT image on navigation system for Water-filled Laparo-endoscopic Surgery," *Transactions of Japanese Society for Medical*

and Biological Engineering, vol. 52, no. Supplement, pp. O-303-O-304, 2014.

[190] Shipeng Xie, Tao Yang, "Artifact Removal in Sparse-Angle CT Based on Feature Fusion Residual Network," *IEEE Transactions on Radiation and Plasma Medical Sciences,* vol. 5, no. 2, pp. 261-271, 2021.

[191] Khaled Ali, Hideaki Ohgaki, Heishun Zen, Toshiteru Kii, Takehito Hayakawa,Toshiyuki Shizuma, Hiroyuki Toyokawa, Yoshitaka Taira, Masaki Fujimoto, Masahiro Katoh, "Experimental Study on 3-D Isotope-Selective CT Imaging Based on Nuclear Resonance Fluorescence Transmission Method," in *IEEE Nuclear Science Symposium and Medical Imaging Conference (NSS/MIC)*, Boston MA, USA, 2020.

[192] Milan Sonka, Vaclav Hlavac, Roger Boyle, Image Processing, Analysis, and Machine Vision, 1ed., H. Gowans, Ed., Springer New York, NY, 1993.

[193] Khaled Ali, Heishun Zen, Hideaki Ohgaki, Toshiteru Kii, Takehito Hayakawa, Toshiyuki Shizuma, Masahiro Katoh, Yoshitaka Taira, Masaki Fujimoto, Hiroyuki Toyokawa, "Fusion Visualization Technique to Improve a Three-Dimensional Isotope-Selective CT Image Based on Nuclear Resonance Fluorescence with a Gamma − CT Image," *Applied Sciences,* vol. 11, no. 24, 2021.

[194] Linda G. Shapiro, George C. Stockman, Computer Vision, 1ed., Pearson, 2000, p. 608.

[195] G. Evelin Sujji, Y. V. S. Lakshmi, G. Wiselin Jiji, "MRI Brain Image Segmentation based on Thresholding," *International Journal of Advanced Computer Research,* vol. 3, no. 1, pp. 97-101, 2013.

[196] N. Senthilkumaran, S. Vaithegi, "Image Segmentation By Using Thresholding Techniques For Medical Images," *Computer Science & Engineering: An International Journal (CSEIJ),* vol. 6, no. 1, pp. 1-13, February 2016.

[197] Ta Yang Goh, Shafriza Nisha Basah, Haniza Yazid, Muhammad Juhairi Aziz Safar, Fathinul Syahir Ahmad Saad, "Performance analysis of image thresholding: Otsu technique," *Measurement*, vol. 114, pp. 298-307, 2018.

[198] Liang-Kai Huang, Mao-Jiun J. Wang, "Image thresholding by minimizing the measures of fuzziness," *Pattern Recognition,* vol. 28, no. 1, pp. 41-51, 1995.

[199] H. K. Anasuya Devi, "Thresholding: A Pixel-Level Image Processing Methodology Preprocessing Technique for an OCR System for the Brahmi Script," *Ancient Asia,* vol. 1, pp. 161-165, 2006.

[200] Nobuyuki Otsu, "A Threshold Selection Method from Gray-Level Histograms," *IEEE Transactions on Systems, Man, and Cybernetics*, vol. 9, no. 1, pp. 62-66, 1979.

10 ACHIVEMENTS

[1] Paper

Khaled Ali, Heishun Zen, Hideaki Ohgaki, Toshiteru Kii, Takehito Hayakawa, Toshiyuki Shizuma, Masaki Fujimoto, Yoshitaka Taira, Masahiro Katoh, Hiroyuki Toyokawa. Fusion Visualization Technique to Improve a Three-Dimensional Isotope-Selective CT Image Based on Nuclear Resonance Fluorescence with a Gamma – CT Image. Appl. Sci. 2021, 11, 11866.

https://doi.org/10.3390/app112411866

[2] Paper

Khaled Ali, Hideaki Ohgaki, Heishun Zen, Toshiteru Kii, Takehito Hayakawa, Toshiyuki Shizuma, Hiroyuki Toyokawa, Yoshitaka Taira, Masaki Fujimoto, Masahiro Katoh, "Three-Dimensional Nondestructive Isotope-Selective Tomographic Imaging of ^{208}Pb Distribution via Nuclear Resonance Fluorescence," Applied Sciences, vol. 11, no. 8, p. 3415. Apr. 2021.

https://doi.org/10.3390/app11083415

[3] Paper

Khaled Ali, Hideaki Ohgaki, Heishun Zen, Toshiteru Kii, Takehito Hayakawa, Toshiyuki Shizuma, Hiroyuki Toyokawa, Yoshitaka Taira, Violeta Iancu, Gabriel Turturica, Alexandru Ur. Călin Masaki Fujimoto, Masahiro Katoh, “Selective Isotope CT Imaging Based on Nuclear Resonance Fluorescence Transmission Method,” IEEE Transactions on Nuclear Science, vol. 67, no. 8, p. 1976-1984, Aug. 2020.

https://doi.org/10.1109/TNS.2020.3004565

[4] International conferences

Khaled Ali, Hideaki Ohgaki, Heishun Zen, Toshiteru Kii, Takehito Hayakawa, Toshiyuki Shizuma, Masahiro Katoh, Yoshitaka Taira, Masaki

Fujimoto, Hiroyuki Toyokawa, “Fused 3D visualization for NRF − CT with a high-quality gamma − CT image,” 2021 IEEE Nuclear Science Symposium and Medical Imaging Conference (NSS/MIC), Oct. 2021, Yokohama, Japan.

[5] International conferences

Khaled Ali, Hideaki Ohgaki, Heishun Zen, Toshiteru Kii, Takehito Hayakawa, Toshiyuki Shizuma, Hiroyuki Toyokawa, Yoshitaka Taira, Masaki Fujimoto, Masahiro Katoh, “Proposal study for the fused visualization technique of 3D NRF − CT and a high-resolution gamma − CT image,”. The 3rd International Conference on Nuclear Photonics (NP2020), Kurashiki, Japan.

[6] International conferences

Khaled Ali, Heishun Zen, Hideaki Ohgaki, Toshiteru Kii, Takehito Hayakawa, Toshiyuki Shizuma, Hiroyuki Toyokawa, Masahiro Katoh, Masaki Fujimoto, Yoshitaka Taira, “Non-destructive inspection of enriched isotope (Pb-208) using nuclear resonance fluorescence with laser Compton scattering,”. The 3rd International Conference on Radiation and Emission in Materials (ICREM). Chiang Mai University, Dec. 2020. Chiang Mai, Thailand.

[7] International conferences

Ali, Khaled and Ohgaki, Hideaki and Zen, Heishun and Kii, Toshiteru and Hayakawa, Takehito and Shizuma, Toshiyuki and Toyokawa, Hiroyuki and Taira, Yoshitaka and Fujimoto, Masaki and Katoh, Masahiro, "Experimental Study on 3-D Isotope-Selective CT Imaging Based on Nuclear Resonance Fluorescence Transmission Method," 2020 IEEE Nuclear Science Symposium and Medical Imaging Conference (NSS/MIC), 2020, pp. 1-2, Boston, MA, USA.

https://doi.org/10.1109/NSS/MIC42677.2020.9507895

[8] International conferences

Ali, Khaled and Ohgaki, Hideaki and Zen, Heishun and Kii, Toshiteru and Hayakawa, Takehito and Shizuma, Toshiyuki and Toyokawa, Hiroyuki and Taira, Yoshitaka and Iancu, Violeta and Turturica, Gabriel and Ur, Călin Alexandru and Fujimoto, Masaki and Katoh, Masahiro, " Experimental Demonstration of Selective Isotope CT -Imaging Based on Nuclear Resonance Fluorescence Absorption Method," 2019 IEEE Nuclear Science Symposium and Medical Imaging Conference (NSS/MIC), 2019, pp. 1-2, Manchester, UK.

https://doi.org/10.1109/NSS/MIC42101.2019.9059859

[9] Poster

Khaled Ali. "Development of Isotope Selective CT Imaging Based on Nuclear Resonance Fluorescence". 13th International Symposium of the Institute of Advanced Energy, September 2022. Kyoto University, Kyoto, Japan.

[10] Presentation

Khaled Ali. K. Ali, H. Ohgaki, H. Zen, T. Kii, T. Hayakawa, T. Shizuma, H. Toyokawa, M. Katoh, M. Fujimoto and Y. Taira, "Evaluation of the gamma-ray CT image resolution by LCS gamma-ray beam in UVSOR – III,". Atomic Energy Society of Japan (AESJ), 2022 Annual Meeting, Japan.

https://doi.org/10.13140/RG.2.2.30720.92166

[11] Presentation

Khaled Ali. "Advanced Utilization of Gamma-ray Based CT Techniques for Nuclear Safeguard and Industrial Applications". 1st IAE Student Research Presentation, March 2022. Kyoto University, Kyoto, Japan.

https://doi.org/10.13140/RG.2.2.27899.59683

[12] Presentation

Khaled Ali, Hideaki Ohgaki, Heishun Zen, Toshiteru Kii, Takehito Hayakawa, Toshiyuki Shizuma, Hiroyuki Toyokawa, Masahiro Katoh, Masaki Fujimoto, Yoshitaka Taira. "Non-destructive Inspection for the hidden isotopes using Laser Compton scattering gamma rays,". Ajou-Kyoto-Zhejiang Joint Symposium on Energy Science, Nov. 2021. Kyoto University, Kyoto, Japan.

https://doi.org/10.13140/RG.2.2.34541.51689

[13] Presentation

K. Ali, H. Ohgaki, H. Zen, T. Kii, T. Shizuma, T. Hayakawa, H. Toyokawa, M. Fujimoto, Y. Taira, M. Katoh, "LCS gamma-ray beams utilization for the isotope selective NRF – CT imaging in UVSOR – III,". UVSORシンポジウム 2021, 分子科学研究所極端紫外光研究施設（UVSOR）, Nov. 2021. Institute for Molecular Science, Okazaki, Japan.

https://doi.org/10.13140/RG.2.2.32759.75684

[14] Presentation

Khaled Ali, Hideaki Ohgaki, Heishun Zen, Toshiteru Kii, Takehito Hayakawa, Toshiyuki Shizuma, Hiroyuki Toyokawa, Masahiro Katoh, Masaki Fujimoto, Yoshitaka Taira, "Fused CT imaging technique to improve 3D isotope-selective NRF – CT image,". Atomic Energy of Society of Japan (AESJ), 2021 Fall Meeting, Oct. 2021. Yokohama City University, Yokohama, Japan.

https://doi.org/10.13140/RG.2.2.34652.92807

[15] Poster

K. Ali, H. Ohgaki, H. Zen, T. Kii, T. Hayakawa, T. Shizuma, H. Toyokawa, M. Katoh, M. Fujimoto, Y. Taira, "Improving of a 3D NRF – CT image by the fusion visualization technique with a 3D gamma – CT image,". The 12th International Symposium of Advanced Energy Science Research Activities

on Zero-Emission Energy Network. Sep. 2021. Kyoto University, Kyoto, Japan.

https://doi.org/10.13140/RG.2.2.10776.11526

[16] Presentation

K. Ali, H. Ohgaki, H. Zen, T. Kii, T. Hayakawa, T. Shizuma, H. Toyokawa, M. Katoh, M. Fujimoto and Y. Taira, "Three-Dimensional Isotope-Selective Tomographic Imaging for Pb-208 distribution based on Nuclear Resonance Fluorescence,". Atomic Energy Society of Japan (AESJ), 2021 Annual Meeting, Waseda University. Tokyo, Japan.

https://doi.org/10.13140/RG.2.2.24837.88808

[17] Presentation

Khaled Ali, et. al. "3D Imaging of Pb-208 via nuclear resonance fluorescence and computed tomography,". 日本原子力学会関西支部若手研究発表会, 第１６回若手研究者による研究発表会. Mar. 2021. (Award).

[18] Presentation

K. Ali, H. Zen, H. Ohgaki, T. Kii, T. Hayakawa, T. Shizuma, H. Toyokawa, M. Katoh, M. Fujimoto, Y. Taira, "Three-Dimensional Tomographic Isotope Imaging of ^{208}Pb by Nuclear Resonance Fluorescence,". The 4th Zhejiang-Kyoto-Ajou Joint Symposium on Energy Science Dec. 2020. Kyoto University, Kyoto, Japan.

https://doi.org/10.13140/RG.2.2.35743.07845

[19] Poster

Khaled Ali, Heishun Zen, Hideaki Ohgaki, Toshiteru Kii, Takehito Hayakawa, Toshiyuki Shizuma, Hiroyuki Toyokawa, Masahiro Katoh, Masaki Fujimoto, Yoshitaka Taira, "3-D Isotope-Selective CT Imaging Based on Nuclear Resonance Fluorescence Transmission Method,". UVSORシンポ

ジウム 2020, 分子科学研究所極端紫外光研究施設（UVSOR）. Institute for Molecular Science, Okazaki, Japan.
https://doi.org/10.13140/RG.2.2.15343.76962

[20] Presentation

K. Ali, H. Ohgaki, H. Zen, T. Kii, T. Hayakawa, T. Shizuma, H. Toyokawa, Y. Taira, V. Iancu, G. Turturica, Calin Ur A, M. Fujimoto and M. Katoh, "Development of Three-Dimensional gamma – CT Scan System in BL1U-UVSOR – III ,". Atomic Energy Society of Japan (AESJ), 2020 Annual Meeting, Fukushima University, Fukushima, Japan.
https://doi.org/10.13140/RG.2.2.31282.12485

[21] Presentation

K. Ali, H. Ohgaki, H. Zen, T. Kii, T. Hayakawa, T. Shizuma, H. Toyokawa, Y. Taira, V. Iancu, G. Turturica, Calin. A. Ur., M. Fujimoto, M. Katoh, "Image Reconstruction of the Enriched Isotope ^{208}Pb Using Nuclear Resonance Fluorescence Absorption Method in UVSOR – III BL1U,". The 3rd Kyoto-Zhejiang-Ajou Joint Symposium on Energy Science, Kyoto University. Dec. 2019. Kyoto, Japan.
https://doi.org/10.13140/RG.2.2.25583.76965

[22] Presentation

K. Ali, H. Ohgaki, H. Zen, T. Kii, T. Hayakawa, T. Shizuma, H. Toyokawa, Y. Taira, Calin. A. Ur. V. Iancu, G. Turturica, M. Fujimoto, and M. Katoh, "Demonstration of Isotope CT Using NRF Absorption Method in UVSOR-BL1U,". Atomic Energy of Society of Japan (AESJ), 2019 Fall Meeting, University of Toyama, Toyama, Japan.
https://doi.org/10.13140/RG.2.2.24795.69923

[23] Poster

K. Ali, H. Ohgaki, H. Zen, T. Kii, T. Hayakawa, T. Shizuma, H. Toyokawa, Y. Taira, V. Iancu, G. Turturica, Calin. A. Ur., M. Fujimoto, M. Katoh, "Image Reconstruction of the Enriched Isotope Pb-208 Using Nuclear Resonance Florescence Absorption Method in UVSOR – BL1U,". The 10th Korea-Japan Joint Summer School on Accelerator and Beam Science, Nuclear Data, Radiation Engineering and Reactor Physics. Osaka University, Aug. 2019, Osaka, Japan.
https://doi.org/10.13140/RG.2.2.14729.36969